

Macroporous silicon for crystalline thin-film solar cells

Der Fakultät für Mathematik und Physik
der Gottfried Wilhelm Leibniz Universität Hannover
zur Erlangung des Grades

Doktor der Naturwissenschaften

Dr. rer. nat.

genehmigte Dissertation

von

Dipl.-Phys. Marco Ernst

geboren am 11. April 1983 in Sulingen

2013

Referent: Prof. Dr.-Ing. Rolf Brendel
Korreferent: Prof. Dr.-Ing. Tobias Wietler
Tag der Promotion: 04.12.2013

Abstract

The typical thickness of an industrial crystalline Si wafer is 180 μm . The Si wafer makes around 30 % of the module cost mainly due to the three crystallizations that are required during wafer production. For cost saving reasons it is highly desirable to slice a thick wafer into many thin films while maintaining the high efficiency potential of crystalline Si.

This work investigates electrochemical etching for fabricating thin macroporous Si layers from crystalline n-type Si wafers for thin-film solar cells. The macroporous Si layers fabricated from 150 mm wafers in this work are up to 133 cm^2 -sized and have a thickness of around 30 μm .

The macroporous structure guarantees a low surface reflectance and an efficient light trapping. The optical performance of macroporous Si is evaluated by measuring the absorption and comparing the photogeneration current density with ideal Lambertian light trapping. Therefore, a (35 ± 2) μm -thick and 133 cm^2 -sized free-standing macroporous Si layer is separated from a 150 mm n-type Si wafer. The randomly arranged pores have an average diameter of (2.3 ± 0.4) μm and an average center-to-center distance of (4.5 ± 1.2) μm . The optical absorption of this sample yields a photogeneration current density of (40.82 ± 0.36) mA cm^{-2} . This is close to the photogeneration current density of (41.43 ± 0.37) mA cm^{-2} calculated for a Lambertian light trapping scheme of identical thickness. Thus, the macroporous Si sample achieves a fraction of 0.985 ± 0.012 of the Lambertian limit. A (34 ± 2) μm -thick sample that has hexagonally arranged macropores achieves a fraction of 0.935 ± 0.003 of the Lambertian limit. In this case, the average pore diameter is (4.0 ± 0.2) μm . Photolithographically defines the pore distance to 8 μm .

The large surface area of the macroporous requires a surface conformal passivation. In this work, thermally grown oxide and plasma-assisted atomic layer deposited aluminum oxide are used to passivate the macroporous Si surface. Aluminum oxide passivates the surface of the optically characterized samples. In case of the (35 ± 2) μm -thick macroporous Si layer with randomly arranged pores, the measured effective carrier lifetimes is (25.7 ± 2.6) μs . The (34 ± 2) μm -thick passivated sample with hexagonally arranged pores yields an effective carrier lifetime of (28.6 ± 2.9) μs .

In order to determine the efficiency potential of macroporous Si, implied J - V curves are measured by contactless photoluminescence-based technique. In this work, the photoluminescence signal is calibrated by means of microwave-detected photoconductance decay method for the first time. This new method determines an efficiency potential of the macroporous Si sample with randomly arranged pores of $\eta = (21.5 \pm 0.4)$ %. In case of the hexagonally arranged pores, the efficiency potential is $\eta = (20.2 \pm 0.4)$ %.

A new method for mechanically supporting and easier handling of the macroporous Si layers is developed in this work. This process laser-bonds the macroporous Si layer to a thick Si frame without contaminating the macroporous Si layer with other materials. Thus, no restrictions arise for the following device processes.

Three concepts for solar cell fabrication using macroporous Si are developed and characterized in this work. The size of the solar cells is 3.92 cm^2 . One approach uses epitaxial growth of p^+ -type silicon onto the n-type macroporous silicon for junction formation. The epitaxial layer has two functions. First, the layer acts as a p-type emitter and second, the epitaxial layer seals the rear side of the macroporous silicon absorber and, thus, eases device fabrication. The best solar cell of this type achieves an open-circuit voltage of 544 mV, a short-circuit current density of 37.1 mA cm^{-2} , and with a fill factor of 65.1 % an energy-conversion efficiency of 13.1 %.

Keywords: Porous silicon, kerf-free, light trapping, thin-film solar cells

Kurzzusammenfassung

Die typische Dicke industrieller kristalliner Si Wafer ist 180 μm . Der Si Wafer macht hierbei einen Kostenanteil von 30 % an den Modulkosten aus, welcher hauptsächlich durch die drei notwendigen Kristallisationsschritte bei der Waferherstellung entsteht. Zur Kosteneinsparung ist es daher, unter Beibehaltung des hohen Wirkungsgradpotentials von kristallinem Si, wünschenswert, einen dicken Wafer in viele dünne Schichten zu teilen.

Diese Arbeit untersucht elektrochemisches Ätzen von kristallinen n-Typ Si Wafern zur Herstellung dünner makroporöser Si Schichten zur Verwendung als Absorber in kristallinen Dünnschichtszellzellen. Die makroporösen Si Schichten in dieser Arbeit, welche aus 150 mm Wafern hergestellt werden, sind bis zu 133 cm^2 -groß und etwa 30 μm dick.

Die makroporöse Struktur gewährleistet eine geringe Oberflächenreflexion, sowie eine effiziente Lichteinkopplung. Die optische Güte von makroporösem Si wird durch Messung der Absorption und Vergleich der Photogenerationsstromdichte mit einer idealen Lambertschen Struktur bewertet. Dafür wird eine (35 ± 2) μm -dicke und 133 cm^2 -große freitragende makroporöse Si Schicht von einem 150 mm n-Typ Wafer abgetrennt. Die zufällig angeordneten Poren haben einen mittleren Durchmesser von (2.3 ± 0.4) μm und einen mittleren Abstand von (4.5 ± 1.2) μm . Die optische Absorption dieser Probe erreicht eine Photogenerationsstromdichte von (40.82 ± 0.36) mA cm^{-2} . Dieser Wert ist nah an der Photogenerationsstromdichte von (41.43 ± 0.37) mA cm^{-2} welche für eine Struktur gleicher effektiver Dicke mit Lambertschem Light-trapping berechnet wird. Somit erreicht die makroporöse Schicht einen Anteil von 0.985 ± 0.012 von dem Lambertschen Limit. Eine weitere Probe mit hexagonaler Porenanordnung erreicht einen Anteil von 0.935 ± 0.003 von dem Lambertschen Limit. In diesem Fall beträgt der mittlere Porendurchmesser (4.0 ± 0.2) μm . Der photolithografisch definierte Porenabstand ist 8 μm .

Die große Oberfläche der Makroporen benötigt eine oberflächenkonforme Passivierung. In dieser Arbeit wird zur Passivierung der makroporösen Oberfläche thermisch gewachsenes Oxid und Aluminiumoxid aus plasmaunterstützter Atomlagenabscheidung verwendet. Aluminiumoxid passiviert die optisch charakterisierten Proben. Im Fall der (35 ± 2) μm -dicken makroporösen Si Schicht mit zufälliger Porenanordnung, ergibt sich eine Ladungsträgerlebensdauer von (25.7 ± 2.6) μs . Die gemessene Ladungsträgerlebensdauer der (34 ± 2) μm -dicken passivierten Probe mit hexagonaler Porenanordnung ist (28.6 ± 2.9) μs .

Um das Wirkungsgradpotential von makroporösem Si zu bestimmen, werden implizierte $J-V$ Kennlinien mit Hilfe einer kontaktfreien, auf Photolumineszenz-Strahlung basierten Methode gemessen. Dabei wird erstmals in dieser Arbeit das Photolumineszenz-Signal mit Hilfe der mikrowellen-detektierten Photoleitfähigkeitsmethode kalibriert. Diese neue Methode bestimmt ein Wirkungsgradpotential der makroporösen Si Schicht mit zufälliger Porenanordnung von $\eta = (21.5 \pm 0.4)$ %. Im Fall der hexagonal angeordneten Poren ergibt sich ein Wirkungsgradpotential von $\eta = (20.2 \pm 0.4)$ %.

In dieser Arbeit wurde eine neue Methode zur mechanischen Unterstützung und vereinfachtem Handling der makroporösen Si Schichten entwickelt. In dem Prozess wird die makroporöse Si Schicht durch einen Laserschweißprozess mit einem dicken Si Rahmen verbunden. Dabei wird die makroporöse Si Schicht nicht mit Fremdmaterialien verunreinigt. Daher entstehen keine Einschränkungen für die nachfolgenden Prozessschritte.

Weiterhin werden in dieser Arbeit drei Konzepte zur Herstellung von Solarzellen aus makroporösem Si entwickelt und charakterisiert. Die hergestellten makroporösen Solarzellen haben eine Größe von 3.92 cm^2 . Ein Ansatz verwendet epitaktisches Wachstum von p^+ -Typ Silizium auf das n-Typ makroporöse Silizium zur Bildung eines pn-Übergangs. Die epitaktisch gewachsene Schicht erfüllt dabei zwei Funktionen. Als Erstes dient die p-Typ Schicht als Emitter der Solarzelle.

Als Zweites schließt die epitaktische Schicht die Rückseite der makroporösen Absorberschicht und vereinfacht dadurch die weitere Prozessierung. Die beste Solarzelle dieses Typs erreicht eine Leerlaufspannung von 544 mV, eine beachtenswerte Kurzschlussstromdichte von 37.1 mA cm^{-2} und mit einem Füllfaktor von 65.1 % einen Wirkungsgrad von 13.1 %.

Schlagwörter: Poröses Silizium, sägeverlustfrei, Lichtsammlung, Dünnschichtsolarzellen

Contents

Introduction	1
1 Macroporous silicon fabrication	3
1.1 Introduction	3
1.2 Electrochemical etching of macropores in n-type Si	3
1.3 Dissolution reaction	5
1.4 Etching setup	7
1.5 Wafer preparation	8
1.6 Current-voltage profiles for small area etching	10
1.7 Current-voltage profiles for large area etching	11
1.8 Etching procedure	12
1.9 Determination of the porosity	16
1.10 Effective thickness	18
2 Modeling surface recombination velocities	19
2.1 Sample preparation	19
2.2 Experimental results	23
2.3 Numerical modeling	27
2.4 Impact of various parameters on the effective carrier lifetime	31
2.5 Conclusion	35
3 Optical characterization	37
3.1 Sample preparation	37
3.2 Structural analysis	38
3.3 Optical measurement setup	40
3.4 Measurement theory	41
3.5 Measurement results	42
3.6 Analytical modeling of the reflection	45
3.7 Fit of experimental data	48
3.8 Photogeneration current density	49
3.9 Current losses	50
3.10 Conclusion	51

4	Efficiency potential	53
4.1	Sample preparation	53
4.2	Measurement setup	54
4.3	Measurement results	56
4.4	Voltage calibration	63
4.5	Calibration results	65
4.6	Statistical error analysis	68
4.7	Results of statistical error analysis	69
4.8	Efficiency potential results	72
4.9	Discussion	72
5	Device fabrication and characterization	75
5.1	Handling of thin films	75
5.2	Individual addressing of surfaces	79
5.3	MacPSi heterojunction solar cells	83
5.4	MacPSi solar cells with epitaxial emitter	95
5.5	MacPSi solar cells with ion implanted emitter	109
6	Summary	119
	Bibliography	121
	List of symbols	129

Introduction

Crystalline silicon solar cell technology benefits from its high energy-conversion efficiency potential and the abundance of the required raw elements.

However, the Si material consumption makes around 30 % of the total costs of an industrial module. This is mainly due to the energy-intensive purification process during wafer production. Currently the wafer thickness of industrial solar cells is approximately 180 μm , but with Si utilization yields of only 45 % to 55 % mainly due to the kerflosses during wire sawing. However, the current Si consumption of approximately 360 μm per solar cell could only be reduced by a factor of 2 with an improved wire sawing technology [Pow12].

Tiedje et al. calculated that such wafer thicknesses are not required for producing $\eta > 20\%$ solar cells [Tie84]. Moslehi et al. recently demonstrated the fabrication of a 43 μm -thick and 20.1 %-efficient 156 mm \times 156 mm-sized solar cell from an epitaxially grown crystalline Si absorber [Mos12].

Hence, slicing of a wafer into many thin films could drastically reduce the wafer costs while maintaining the high efficiency potential of crystalline Si. Currently several technologies with no significant kerfloss for thin ($< 50\ \mu\text{m}$) silicon absorber production are under development [Tay96, Bre97, Dro07, Hen09].

Lehmann et al. proposed and patented the formation and separation of macroporous silicon layers as an absorber for thin silicon solar cells by means of electrochemical etching in 1992 [Leh92].

However, no experimental verification of fabricating and using free-standing macroporous Si layers as absorber material was reported at the time when this PhD was started. This work therefore focuses on the fabrication and electrical and optical characterization of macroporous Si layers for crystalline Si solar cells. The thesis investigates device processes for fabricating thin macroporous Si solar cells.

Chapter 1 presents the theoretical background of electrochemical etching for understanding the electrochemical fabrication process of macroporous Si layers in hydrofluoric acid from crystalline n-type Si substrates. This chapter introduces the wafer preparation and electrochemical etching setups for small (1 cm^2) and large (133 cm^2) area. It discusses the etching procedure for fabricating free-standing macroporous Si layers.

Chapter 2 derives a three-dimensional numerical model to calculate effective carrier lifetimes of macroporous Si as a function of the pore geometry, bulk recombination, and surface recombination. The numerical model is experimentally verified by measuring carrier lifetimes of surface passivated macroporous Si samples.

Chapter 3 optically characterizes free-standing macroporous Si layers. An integrating sphere measures the hemispherical reflection of macroporous Si. An analytical model is used to calculate the optical absorption in the macroporous Si absorber. Lambertian light trapping is a benchmark for efficient light trapping. The optical absorption of macroporous Si is compared with the absorption expected for an ideal Lambertian absorber.

Chapter 4 presents a method for determining the efficiency potential of new absorber materials. The contactless method measures the photoluminescence signal of surface passivated Si absorbers and is calibrated by means of transient photoconductance decay measurement. This new method is applied to the macroporous Si absorbers fabricated in this work.

Chapter 5 fabricates solar cells from free-standing macroporous Si layers. The particular challenges for fabricating solar cells from macroporous Si are addressed in this chapter before three types of emitter formation are presented. The first solar cell concept applies a heterojunction cell process with amorphous silicon to the macroporous Si samples. The second approach epitaxially grows an p^+ -type emitter on macroporous Si. The third concept implants phosphorus and boron ions to form the highly-doped regions in the macroporous Si layer.

Finally, **Chapter 6** summarizes the results of this work.

1 | Macroporous silicon fabrication

1.1 Introduction

Silicon easily dissolves in aqueous alkaline etching solutions, but however is chemically resistant in most aqueous acids [Wil96, Wil03]. The first experiments of electrochemical dissolution of p-type silicon in an aqueous hydrofluoric acid (HF)-solution have been performed by Uhler in 1956 [Uhl56]. Uhler observed a “matte black, brown, or red deposit” on the surface of anodized silicon substrates. In contrary to his expectations, he observed a dissolution valence of 2.0 ± 0.2 instead of 4. Two years later, Turner performed several experiments with the electrochemical dissolution of p- and n-type silicon in hydrofluoric acid containing electrolytes [Tur58]. He observed the forming of a thick colored film on the surface of the silicon substrate below a critical current density and electropolishing of the surface above this current density with a dissolution valence of 4. This critical current density was discovered to depend on the electrolyte temperature and HF-concentration. Furthermore, Turner found that an illumination or heat source is required to dissolve n-type silicon substrates.

Almost two decades later, the porous structure of the electrochemically etched film was discovered by Watanabe and Sakai [Wat71] in 1971. They found, that the wafer’s surface is porosified below a critical current density, when applying a constant voltage between a platinum cathode and a silicon anode in an HF-containing electrolyte solution [Wat71].

Formation of trenches in an n-type silicon anode in the dark was first described by Theunissen et al. [The70, The72]. With the beginning of the 1990s, Lehmann and Föll demonstrated the electrochemical etching of ordered arrays of macropores¹ in n-type silicon under rear side illumination [Leh90]. The wafer’s surface was photolithographically pre-structured with inverted pyramids. The cylindrical macropores start growing orthogonal to the (100)-surface at the tips of the pyramids.

1.2 Electrochemical etching of macropores in n-type Si

A silicon electrode dissolves in an acidic electrolyte containing fluorine ions (F^-) under the presence of electronic holes (h^+). In order to generate the required holes, the n-type

¹ According to the IUPAC (International Union of Pure and Applied Chemistry) [Sin85] pore sizes > 50 nm are termed as macropores.

silicon has to be illuminated [Leh90]. Hole generation by high electrical field-strength leads to breakdown-pores instead, as observed by Theunissen et al. [The70, The72].

Controlled macropore formation requires (a) the pore walls to be passivated from dissolution, and (b) the pore tips in a state that facilitates dissolution of the Si [Leh93].

Both requirements are fulfilled by the applied external electric field. The electric field lines focus the hole-current to the pore tips within the space charge region and, thus, facilitate dissolution of Si. Since most of the holes are consumed at the pore tips, the pore walls are protected from dissolution.

Figure 1.1 illustrates the Si/HF contact under anodic bias conditions. Holes are generated by illumination of the rear side of the Si substrate and diffuse to the Si/HF interface. Within the space charge region, the holes drift to the pore tips as a result of the electric field and react with the fluorine ions in a chemical reaction (described in subsection 1.3). Stable pore growth is obtained if the holes are the limiting species of the dissolution process. Since the chemical reaction at the pore tips consumes most of the holes, holes are depleted in the porous region and therefore no essential dissolution of the pore walls occurs. An n^+ -type region at the rear side of the wafer provides ohmic contact to the electrode.

Pre-structuring of the wafer's surface (e. g. with inverted pyramids) facilitates pore nucleation but, however, the requirement for stable pore growth limits the possible range for pore spacing [Leh90]. Too closely spaced pores tend to die out whereas high distances lead to a significant dissolution of the pore walls and branching of pores.

Planar (e. g. shiny-etched) surfaces lead to a random pore nucleation. In this case, the nucleation process can be described by an Ostwald ripening process [Leh98]. Small differences in height and local defects lead to locally varied current densities and, thus, to a surface roughening. Small etch pits are formed, which gradually develop into larger pores until the stable pore growth regime is reached.

According to Lehmann [Leh93], a constant current density J_{PS} at the pore tips characterizes the steady state conditions between charge transfer and mass transport. Consequently, the rate r of pore growth in depth is constant:

$$r = \frac{J_{PS}}{n_v q N_{Si}}. \quad (1.1)$$

Here n_v is the dissolution valence, $q = 1.6022 \times 10^{-19}$ A s the elementary charge, and $N_{Si} = 5.02 \times 10^{22}$ cm⁻³ the atomic density of silicon.

Since the local current density is constant, the porosity p and, thus, the pore diameter is controlled by the total etching current density J :

$$p = \frac{J}{J_{PS}}. \quad (1.2)$$

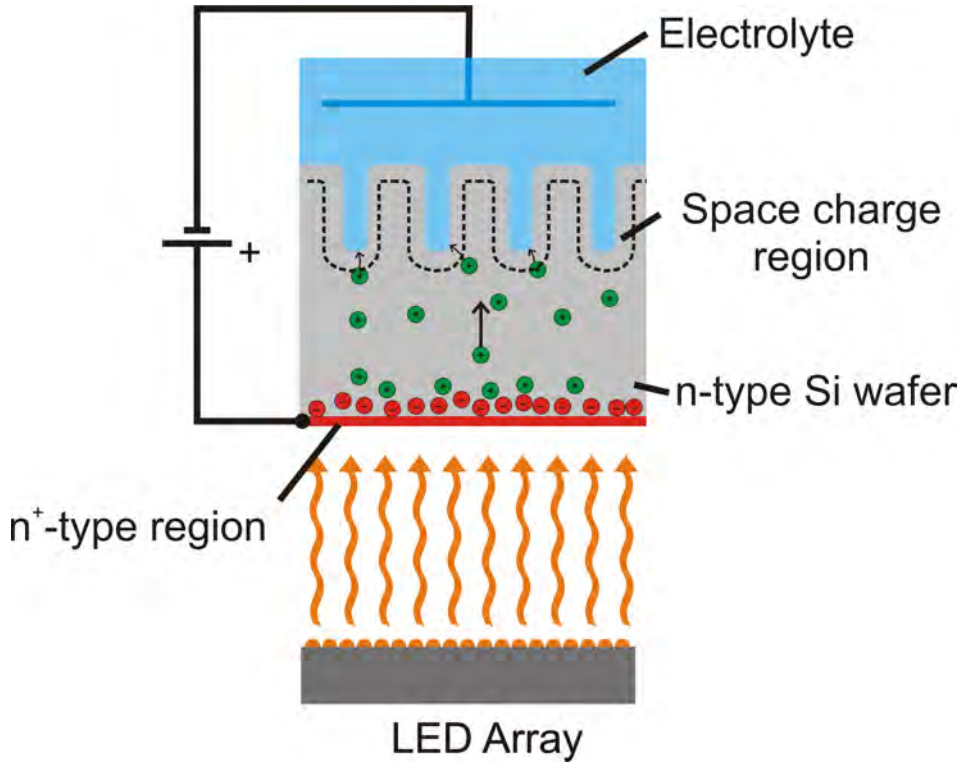


Figure 1.1: Illustration of macropore etching in n-type Si wafers. Electron-hole pairs are generated by illuminating the rear side and separated by the anodic bias. Holes diffuse to the Si/HF interface and drift to the pore tips within the space charge region.

The critical current density J_{PS} depends on the HF-concentration c_{HF} in wt% and the temperature T in K [Leh93]:

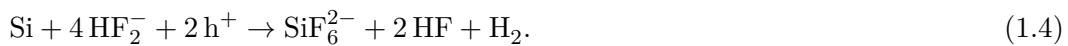
$$J_{PS} = C c_{HF}^{3/2} \exp(-E_a/kT). \quad (1.3)$$

Here k is the Boltzmann constant. The constant of proportionality $C = 3300 \text{ A cm}^{-2}(\text{wt}\%)^{-3/2}$ and activation energy $E_a = 345 \text{ meV}$ were empirically determined by Lehmann [Leh93].

1.3 Dissolution reaction

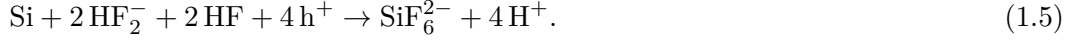
As noted in the introduction, there are two important reaction channels for electrochemical dissolution of Si in HF-containing electrolytes. Divalent reactions dominate for etching current densities $J < J_{PS}$. Above this critical current density tetravalent reaction dominate.

One divalent reaction described in Ref. [Leh91] is



In this reaction two holes are required, thus the dissolution valence is $n_v = 2$.

For anodic current densities $J \geq J_{\text{PS}}$ one possible tetravalent reaction described in Ref. [Pro94] is



This reaction channel is also known as electropolishing. First, an oxide film develops under consumption of two holes at the Si/electrolyte interface. The following chemical dissolution of this oxide film in the HF-containing electrolyte consumes two additional holes. Thus, four holes are consumed for this reaction channel and the dissolution valence is $n_v = 4$. The reaction speed is limited by the dissolution of the oxide film rather than hole transport to the Si/electrolyte interface. Thus, the surface is homogeneously dissolved as holes are distributed uniformly at the surface.

For stable macropore etching both reaction channels are important. According to the steady-state condition of the pore tips, the tetravalent reaction dominates etching of the pore tips. With decreasing current density into the pore walls, the divalent reaction is more likely. This leads to an average dissolution valence of $2.2 < n_v < 3$ [Leh93].

After Lehmann's model [Leh93] the steady-state condition $J_{\text{tip}} = J_{\text{PS}}$ at the pore tips has to be fulfilled for stable macropore growth. Hence, the local current density J_{tip} at the pore tips equals the critical current density J_{PS} and, thus, the centers of the pore tips are electropolished.

As Fig. 1.2a illustrates, the current density decreases with increasing angle θ :

$$J_\theta = J_{\text{PS}} \cos \theta. \quad (1.6)$$

For current densities $J < J_{\text{PS}}$ a mesoporous film develops at the pore walls. Figure 1.2b shows a scanning electron microscope (SEM, S-4800 from Hitachi) micrograph of a pore tip. The center of the pore tip is electropolished and, thus, indicates a local current density of $J = J_{\text{PS}}$ in this region. The thickness of the mesoporous film increases towards the pore walls.

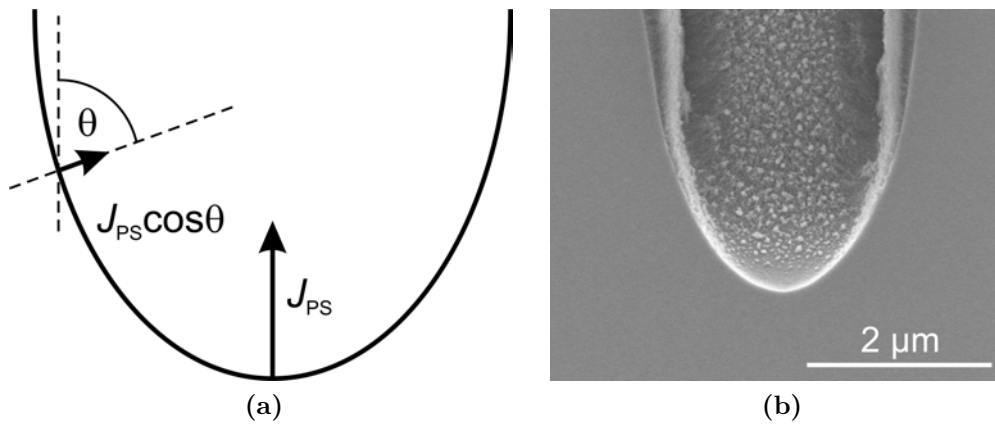


Figure 1.2: (a) Schematic representation of the current distribution at the pore tips. (b) Cross sectional SEM micrograph of a pore tip with a mesoporous film at the pore walls. The smooth surface without a mesoporous film is clearly visible at the center of the pore tips.

1.4 Etching setup

This section describes the two etching setups used in this work. Figure 1.3a shows the small area etching setup (Laboratory test setup from ET&TE Etch and Technology GmbH). The illumination source is a light-emitting diode (LED)-array which emits light at a wavelength of 890 nm. A rubber ring seal defines the etched area to 1 cm^2 . The working electrode (red) is a platinum wire and contacts the Si wafer at the rear side. A platinum

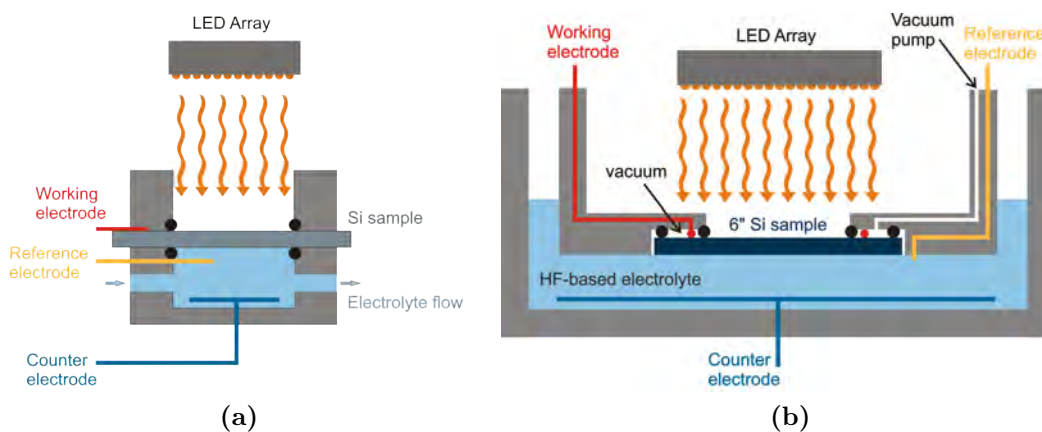


Figure 1.3: Schematics of the electrochemical etching setup with rear-side illumination with an etched area of (a) 1 cm^2 (small area etching setup) and (b) 133 cm^2 (large area etching setup). Figure from Ref. [Ern12b].

reference electrode (yellow) close to the substrate surface measures the potential drop in the electrolyte. The counter electrode (blue) is a platinum wire mesh in the electrolyte.

A peristaltic pump that is attached to an electrolyte container refreshes the electrolyte in the etching cell during electrochemical etching. Due to the large containment in comparison with the small etched area, HF-consumption during etching is negligible in this setup.

Figure 1.3b schematically shows the large area etching setup (Wafer setup from ET&TE Etch and Technology GmbH). The front surface of the 150 mm wafer is fully exposed to the electrolyte. The illuminated and, thus, etched circular area is 133 cm^2 .

The illumination source is a LED-array which emits light at a wavelength of 890 nm. The non-illuminated edge of the wafer is about 1 cm wide in this setup. In this area the wafer is held by vacuum that is established in between two rubber ring seals at the rear side.

The wafer is contacted at the rear side by a platinum foil (red) between the two rubber ring seals. A reference electrode (yellow) close to the substrate surface is used to measure the potential drop in the electrolyte. The counter electrode (blue) in the electrolyte is a platinum covered graphite electrode.

In the large area etching setup, periodic tilting of a rocking table constantly renews the electrolyte at the wafer's surface. A peristaltic pump redoses the amount of consumed HF during one etching process from a 40 wt% HF solution. Etching of one 133 cm^2 -sized macroporous Si layer with a thickness of $30\text{ }\mu\text{m}$ consumes approximately 7 ml of 40 wt% HF.

In this work a 3 wt% aqueous HF-solution at $20\text{ }^\circ\text{C}$ is used. Adding 7.5 vol% acetic acid to the solution improves surface wetting.

1.5 Wafer preparation

The Si substrates used in this work are (100)-oriented, 150 mm, Czochralski (CZ)-grown, shiny-etched, n-type Si wafers. In contrast to commonly used 150 mm substrates, the wafers used in this work have a notch instead of a flat that indicates the crystallographic planes of the wafer. This enlarges the usable area in the electrochemical etching setup. The substrate resistivity is $(1.5 \pm 0.2)\text{ }\Omega\text{ cm}$. This corresponds to a dopant concentration of $N_D = (3.2 \pm 0.4) \times 10^{15}\text{ cm}^{-3}$. The thickness of the substrates is $(305 \pm 20)\text{ }\mu\text{m}$.

A phosphorus diffusion at the rear side of the wafer provides an ohmic contact and lateral conductivity during electrochemical etching.

For rear side diffusion, the wafers are RCA cleaned [Ker70] and a 110 nm-thick oxide layer grows by wet thermal oxidization at $900\text{ }^\circ\text{C}$ in a furnace. The oxide layer serves as diffusion barrier for the front side of the wafer. A lint-free 40 wt% HF-saturated cloth removes the oxide layer at the rear side. Subsequently, an RCA cleaning and a phosphorus diffusion from a POCl_3 -source at a temperature of $980\text{ }^\circ\text{C}$ creates a highly doped region with a sheet resistance of $(10 \pm 2)\text{ }\Omega$ as measured by means of 4-point probes method on

reference samples. Finally, a 1 wt% HF-solution removes the oxide layer on the front side and the phosphosilicate glass on the rear side.

Some of the wafers additionally receive a pre-patterning of the front side. First, the front side of the wafer is spin-coated with a photoresist. Subsequently, UV-irradiation develops the positive resist through a shadow mask with hexagonally arranged circular openings with diameters of $1.5\ \mu\text{m}$. Then, reactive ion etching (RIE) creates cylindrical depressions in the Si surface at this positions. Finally, an acetone solution removes the resist. The patterning of the front side is performed at the Christian-Albrechts-Universität zu Kiel.

The surface patterning results in cylindrical depressions as shown in Figure 1.4a. The depth of the cylinders is $2\ \mu\text{m}$ and the diameter is $3\ \mu\text{m}$. The center-to-center distance is $2r_0 = 8\ \mu\text{m}$. However, pore nucleation requires pronounced tips. For this purpose, anisotropic etching of inverted pyramids is performed.

For anisotropic etching, an RCA cleaned wafer is deposited with a silicon nitride double layer onto the rear side. The SiN_x double layer consists of a $100\ \text{nm}$ -thick SiN_x layer with a refractive index of 1.9 and a $30\ \text{nm}$ -thick SiN_x layer with a refractive index of 2.4 and protects the phosphorus diffusion at the rear side from dissolution. Anisotropic etching is then performed in a 25 wt% potassium hydroxide (KOH) solution with 0.5 wt% polyethylene glycol (PEG) at $50\ ^\circ\text{C}$ for 120 min. Finally, the wafer is RCA cleaned and a 40 wt% HF-solution removes the SiN_x protecting layer.

Figure 1.4b shows the resulting inverted pyramids with a base length of $4\ \mu\text{m}$ at the front side. The distance of the pyramid tips is $2r_0 = 8\ \mu\text{m}$.

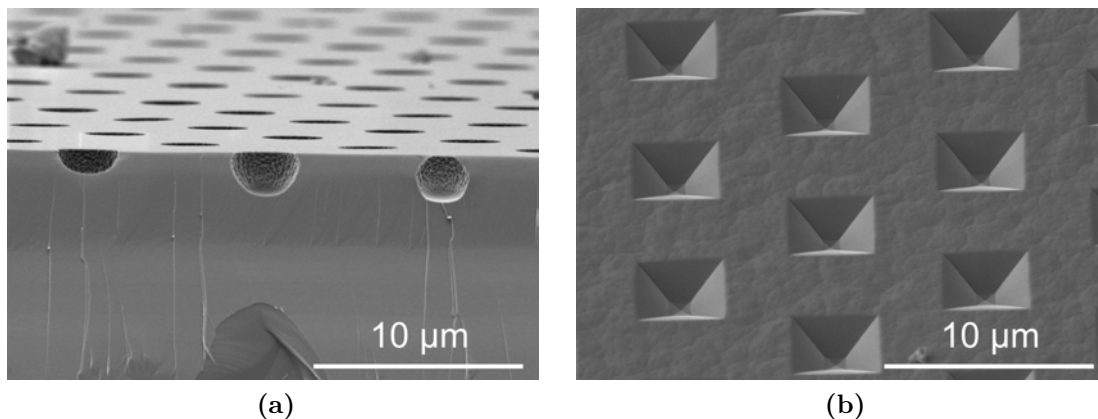


Figure 1.4: (a) Cross sectional SEM micrograph of the surface patterning after RIE. (b) Tilted view on the surface after pyramid etching in a KOH-solution.

1.6 Current-voltage profiles for small area etching

Figure 1.5 shows measured current-voltage curves of the Si/HF interface for various illumination intensities I . The current-voltage curves are measured using the small area etching setup. The electrolyte is a 3 wt% HF with 5 vol% acetic acid added as a wetting agent. The bias voltage U is measured between the rear contact of the Si substrate and a reference electrode in the electrolyte near the wafer's surface. No significant current flow is measured without rear side illumination (red line).

Under rear side illumination, the current density increases for increasing voltages until a saturation current density J_{sat} is reached (solid lines). With increasing illumination intensity (green, blue, pink, and orange lines), the current density saturates at higher values. At this point, every hole that diffuses from the rear side to the Si/HF interface participates in the dissolution process. For increasing illumination intensities the saturation current density increases. This relation holds true until the dissolution process is limited by mass transport of the fluorine ions (pink and orange lines). For a sufficiently high illumination intensity, the current density J is above a critical current density J_{PS} for voltages $U > U_{\text{PS}}$. Electropolishing of the surface occurs beyond this point.

In this work, the “illumination mode” is used for controlled growth of macropores. In this mode, the anodic bias voltage U is set to a value where the current density is in the saturation regime and, thus, constant and independent of the bias voltage. In order to reach a set current density J , the illumination intensity I is adjusted using a feed back loop.

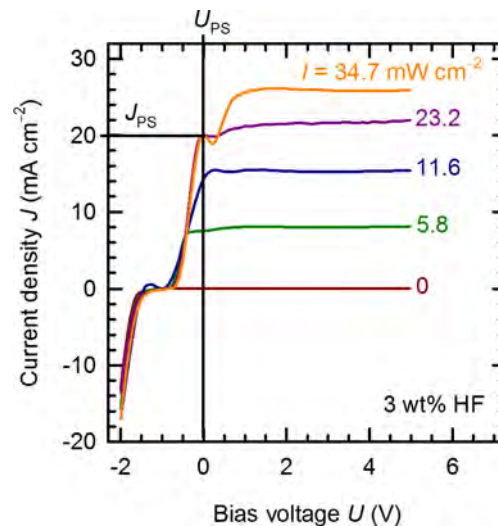


Figure 1.5: Measured current-voltage curves of the Si/HF interface using the small area setup for various illumination intensities.

1.7 Current-voltage profiles for large area etching

The phosphorous doped region at the rear side is essentially a series resistance that influences the current-voltage characteristics. This section therefore addresses the influence of the sheet resistance on the current-voltage profile for large area etching.

Figure 1.6a shows measured current-voltage profiles of the Si/HF interface for two phosphorus diffused wafers with a sheet resistance of $10\ \Omega$ and $40\ \Omega$, respectively. The current-voltage profiles are measured using in the large area etching setup. The horizontal and vertical lines mark the saturation current density J_{sat} and saturation voltage U_{sat} of the $10\ \Omega$ sample (red) and the $40\ \Omega$ sample (green). The decreased series resistance of the $10\ \Omega$ sample determines the steeper slope of the current-voltage curve in Fig. 1.6a compared with the $40\ \Omega$ sample.

From several current-voltage curves measured for illumination intensities ranging from $5.8\ \text{mW cm}^{-2}$ to $40.5\ \text{mW cm}^{-2}$ the saturation current densities J_{sat} and saturation voltages U_{sat} are extracted. Figure 1.6b plots the saturation voltage U_{sat} against the saturation current density J_{sat} for both samples. The current-voltage curves were measured for various constant illumination intensities. In case of the $40\ \Omega$ sample, high current densities – which are required for etching of the separation layer – can only be reached for voltages $\gg 5\ \text{V}$. However, breakdown of the Si/HF junction may occur at such elevated voltages.

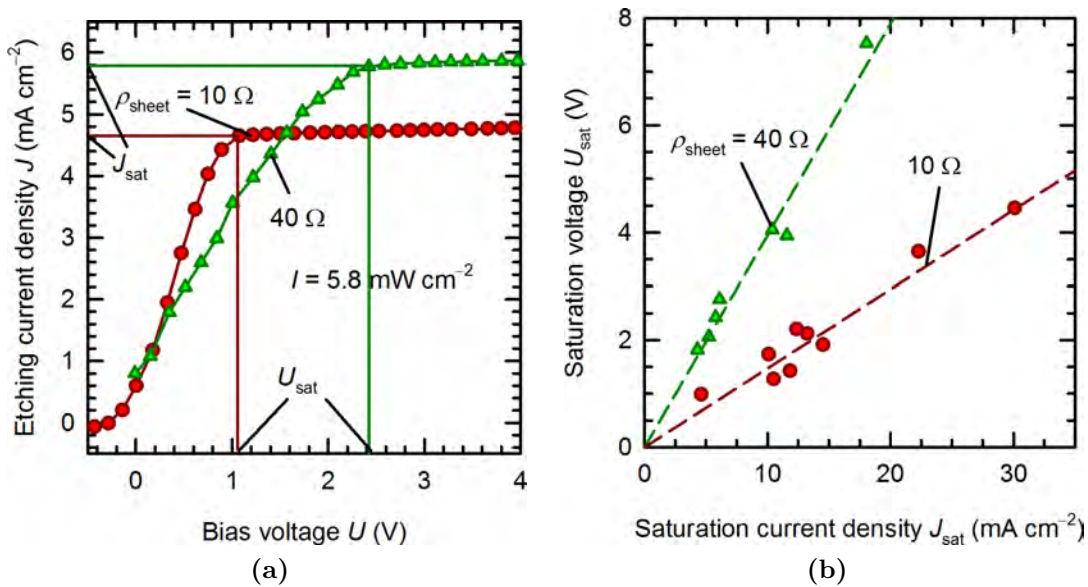


Figure 1.6: (a) Current-voltage profiles of the Si/HF interface using the large area etching setup for a sheet resistance at the rear side of $10\ \Omega$ and $40\ \Omega$ measured for an illumination intensity $I = 5.8\ \text{mW cm}^{-2}$. (b) Saturation voltage U_{sat} plotted against the saturation current density J_{sat} for both sheet resistances.

1.8 Etching procedure

Figure 1.7 schematically shows the macroporous silicon process. (a) The process starts with an n-type wafer that optionally has a pre-structured surface on the side facing the electrolyte. (b) The electrochemical etching procedure then creates a typically $W = 20\ \mu\text{m}$ to $40\ \mu\text{m}$ -thick macroporous silicon layer with a porosity of approximately 30% and (c) a separation layer with a porosity of 100%. The low-porosity layer maintains attached to the wafer only at the un-etched rim. (d) The low-porosity layer is the later absorber layer and is finally detached from the substrate. The substrate can be cleaned and reused in a cyclic procedure.

Figure 1.8 shows a typical etching profile for the large area etching setup to fabricate a $30\ \mu\text{m}$ -thick macroporous Si layer from a pre-structured Si substrate wafer. The solid dark red line is the set value of the etching current density J . The dashed red line is the measured etching current density that follows the set value. The solid dark blue and the dashed blue lines are the set and measured values of the bias voltage U , respectively. The dashed green line shows the illumination intensity I that is controlled for adjusting the current density.

The low-porosity absorber layer is formed by applying an etching current density of $6\ \text{mA cm}^{-2}$ for 40 min. In case of wafers with a shiny-etched surface, the random pore nucleation takes additional 15 min. In case of the pre-structured wafers, the pores start growing immediately at the tips of the inverted pyramids with a growth rate of $r = 0.7\ \mu\text{m min}^{-1}$.

Enhancing of the etching current density to $24.8\ \text{mA cm}^{-2}$ within 6 min broadens the pores in a depth of approximately $30\ \mu\text{m}$ to form a highly porous separation layer. This current density level is maintained for $\approx 12\ \text{min}$ to form a cavity underneath the absorber layer that allows for the detachment of the macroporous top layer from the substrate [Ern10], [Ern12a].

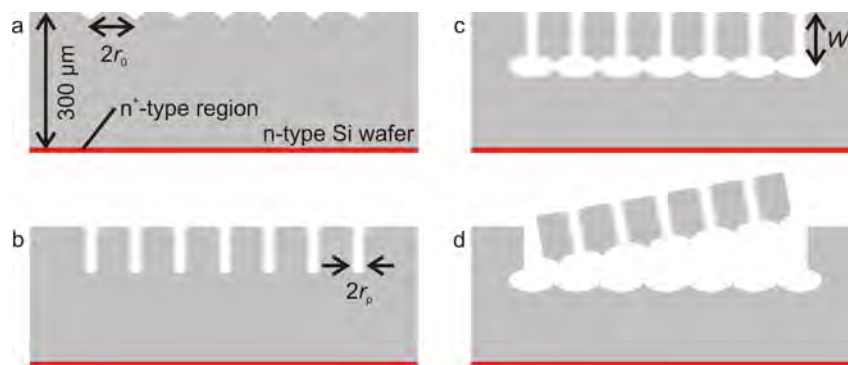


Figure 1.7: Illustration of the macroporous silicon process (a) starting with a pre-structured n-type Si wafer, (b) and (c) macroporous absorber and separation layer formation, (d) detachment of the macroporous layer. Figure from Ref. [Ern13c].

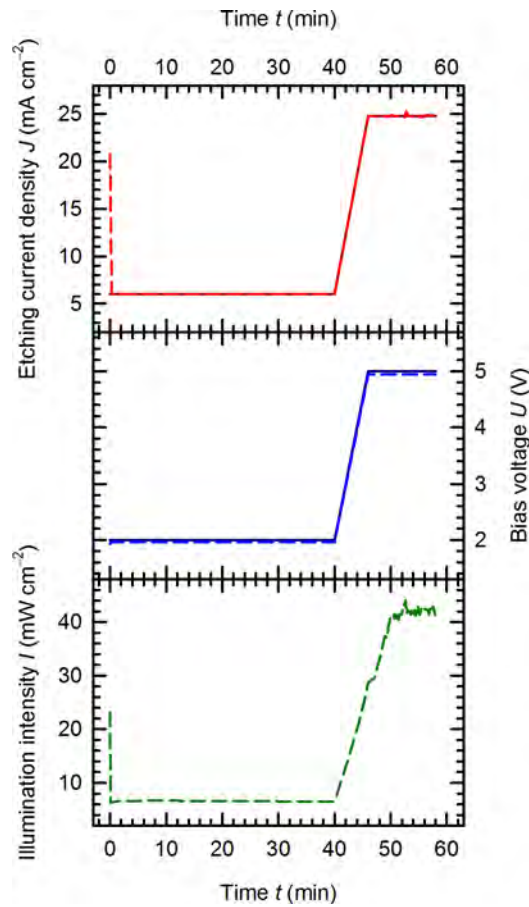


Figure 1.8: Etching current density J , bias voltage U , and illumination intensity I profile to form an approximately 30 μm thick macroporous silicon layer with a highly porous separation layer.

Parallel to the current density profile the voltage is raised from an initial value of 2 V to a value of 5 V for etching the separation layer. Since the working electrode contacts the wafer only at the rim, ohmic losses increase in direction to the center of the wafer. The increased voltage compensates the increasing ohmic losses at higher current densities.

1.8.1 Structural analysis

Figure 1.9a shows a SEM micrograph of the cross section of a low-porosity macroporous layer. One half of the sample shown in the right hand side of Fig. 1.9a was pre-structured with inverted pyramids prior to electrochemical etching; the other half was left planar (left hand side). The macropores in the pre-structured region are deeper than the pores in the region with the planar surface, because the pores start growing immediately at

the pyramids tips. Furthermore, the first few μm in the planar region are etched and roughened during the pore nucleation phase. This causes the small step between the planar and pre-structured region.

The advantage of using planar wafers for macropore formation is the less complex wafer preparation prior to the electrochemical etching. For a lateral homogeneous macropore growth over a large area, the surface preparation plays an important role, since the pores start growing preferably at surface defects. On the other hand, the use of pre-structured silicon allows more control over parameters like pore diameter and surface area of the resulting layer. Furthermore, the risk of parasitic etching of the pore walls is lower for the pre-structured wafers.

Figure 1.9b shows a free-standing macroporous Si layer. The sample is prepared from a photolithographically pre-structured wafer with the etching parameters given in Section 1.8. The pores appear noncontinuous in this SEM micrograph due to tilted breakage when preparing the cross section. This is an artifact.

The pore shape is a rounded square. The thickness of the layer is $(29 \pm 2) \mu\text{m}$. The pore distance is defined by the hexagonal pattern to $8 \mu\text{m}$. The average pore diameter is $(4.0 \pm 0.2) \mu\text{m}$.

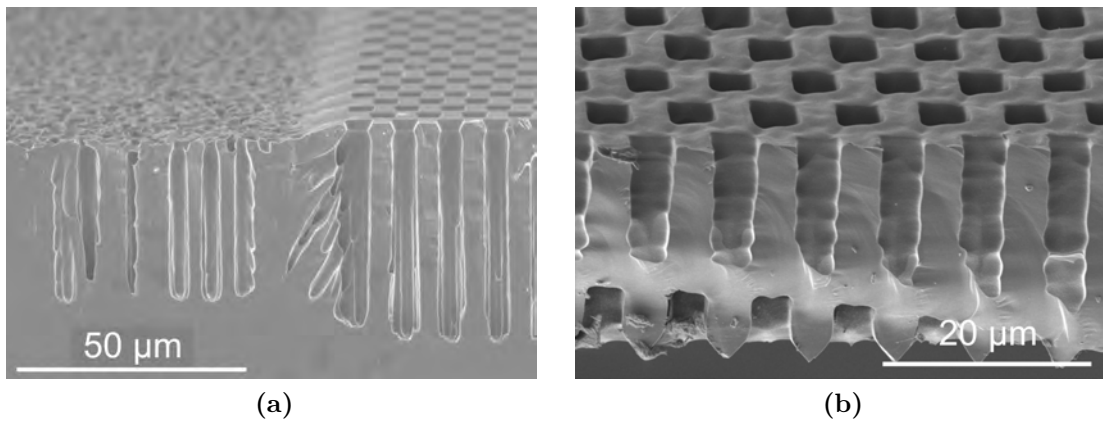


Figure 1.9: (a) SEM micrograph of the cross section of a low-porosity macroporous layer. The surface of the wafer on the right hand side is structured with inverted pyramids; the surface on the left hand side is shiny-etched prior to electrochemical etching. Figure from Ref. [Ern12b]. (b) Cross sectional SEM micrograph of a free-standing macroporous Si absorber layer after detachment from the substrate. The upper side in the micrograph is the side that was facing the electrolyte during electrochemical etching. The pores appear noncontinuous due to a tilted breakage.

1.8.2 Layer detachment

The macroporous Si layers fabricated in this work are only attached to the substrate at the unetched rim of the wafer. The layer can be easily removed from the substrate by laser-cutting the rim and taking it off. A thin razor blade is used to lift-off the macroporous Si layer from the substrate.

Figure 1.10 shows a 133 cm^2 -sized and $(29 \pm 2)\text{ }\mu\text{m}$ -thick macroporous Si layer that is detached from a pre-structured wafer with a pore distance of $8\text{ }\mu\text{m}$. A high optical absorption is expected from the dark appearance of the front side in Fig. 1.10a. The colored shimmer of the rear side in Fig. 1.10b is caused by light diffraction due to the regular patterning.

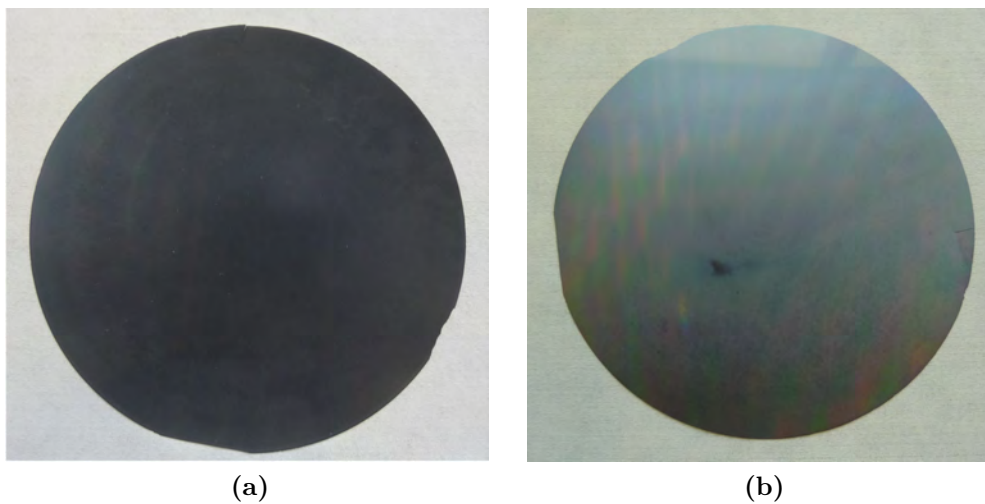


Figure 1.10: Photo of a 133 cm^2 -sized and detached free-standing macroporous silicon of the (a) front side. This is the side that was facing the substrate during electrochemical etching. (b) Photo of the rear side. This is the side that was facing the electrolyte during electrochemical etching.

1.9 Determination of the porosity

The porosity p of macroporous (or generally porous) Si is defined as the volume fraction V_{pore} of the pores over the total volume V_{total}

$$p = \frac{V_{\text{pore}}}{V_{\text{total}}}. \quad (1.7)$$

Hence, the determination of the porosity requires the measurement of the amount of dissolved silicon and the measurement of the geometrical dimensions. The following subsections describe two methods for determining the porosity of macroporous Si.

1.9.1 Gravimetric analysis

Gravimetric analysis is performed using a precision balance (AUW120D from Shimadzu). The balance resides on a weighing table and is equipped with a wind deflector. The reading precision is $10 \mu\text{g}$ with a standard error of measurement of $20 \mu\text{g}$. The typical weight difference of an etched $(1.0 \pm 0.1) \text{ cm}^2$ -sized sample and a pore depth of $(36.3 \pm 0.1) \mu\text{m}$ with a porosity of $(29.1 \pm 1.9) \%$ is $(2470 \pm 20) \mu\text{g}$ and, thus, the measurement precision is sufficient for determining the porosity.

The gravimetric analysis requires the measurement of the weight of the dissolved silicon m_{pore} and the total silicon weight m_{tot} prior to etching. The weight of the dissolved silicon is the difference of the sample weight m_1 prior to etching and the weight m_2 after etching of the pores.

Since the total Si weight m_{tot} cannot be measured directly, it is calculated as the product of the measured pore depth W , the etched area A , and the density of Si $\rho_{\text{Si}} = 2.33 \text{ g cm}^{-3}$. The pore depth is determined from SEM micrographs.

The porosity p_{wt} then calculates as:

$$p_{\text{wt}} = \frac{m_{\text{pore}}}{m_{\text{tot}}} = \frac{m_1 - m_2}{\rho_{\text{Si}}AW}. \quad (1.8)$$

1.9.2 Geometric calculation

In order to calculate the porosity of macroporous silicon layers from the measured pore morphology, a hexagonally arrangement of the randomly distributed pores with an average center-to-center distance $2r_0$ is assumed. In SEM micrographs a rounded square pore shape is observed (compare Fig. 1.9b). The geometric porosity is calculated for a circular and a squared pore shape.

In the first case, a circular pore shape with radius r_p is assumed. Hence, the geometric porosity $p_{\text{geo,circular}}$ is calculated as the circular pore area A_{pore} over the area of the hexagonal unit cell A_{hex} , thus

$$p_{\text{geo,circular}} = \frac{A_{\text{pore}}}{A_{\text{hex}}} = \frac{\pi r_p^2}{2r_0^2\sqrt{3}}. \quad (1.9)$$

In the second case, squared pores with an edge length of $2r_p$ are assumed. Thus,

$$p_{\text{geo,square}} = \frac{(2r_p)^2}{2r_0^2\sqrt{3}}. \quad (1.10)$$

1.9.3 Comparison of gravimetric and geometric approach

The gravimetric analysis and geometric approach for determining the porosity are compared by preparing macroporous samples with various constant etching current densities.

Figure 1.11 shows the porosity determined by the geometric approaches over the porosity determined by weighting. The red circles show the calculated porosity for a circular pore shape, the green boxes show the calculated porosity for a quadratical pore shape.

The porosity for quadratical pores agrees well with the porosity determined by weighting. In case of the circular pore shape, the porosity is underestimated. Thus, the shape of the pores is basically a square.

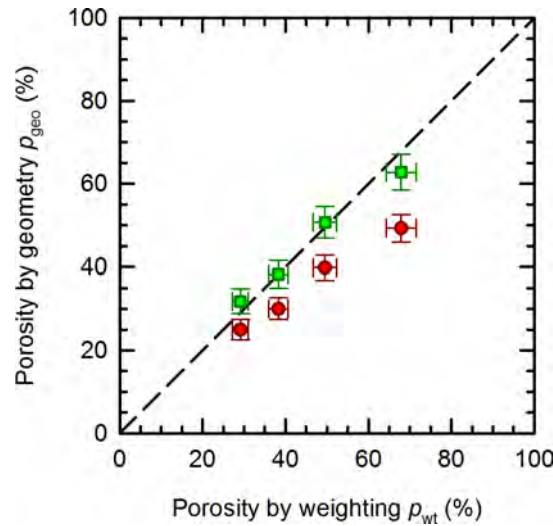


Figure 1.11: Porosity measured by geometric calculation over porosity measured by weighting.

1.10 Effective thickness

For optical characterization of the macroporous Si samples the equivalent Si thickness of a compact and planar film is required. Therefore, the effective thickness

$$W_{\text{eff}} = W (1 - p) \tag{1.11}$$

is calculated. The effective thickness is a measure of the Si material quantity and calculates from the sample thickness W and the porosity p .

2 | Modeling surface recombination velocities

Light-generated carriers in thin macroporous silicon absorbers recombine in the bulk or, more likely at the large surface of the pores. Understanding measured effective carrier lifetimes is important for process optimization and for designing a device. The surface recombination velocity (SRV) of passivated silicon surfaces by e.g. thermally grown oxide layers depends on the crystallographic orientation [Sch96], [Hur02]. Since the macroporous surface shows various surface orientations, the SRV cannot be determined using planar reference samples. Instead an average SRV needs to be determined experimentally.

In Ref. [Ern11], we derived an analytical model that determines the effective carrier lifetime of passivated macroporous silicon layers as a function of pore morphology, bulk lifetime and surface recombination. In that analytical approach, the two-dimensional problem described by a cylindrical unit cell is solved separately for each dimension. Therein, the impact of the layer thickness on the effective carrier lifetime of passivated macroporous silicon samples is investigated experimentally. The analytical model results in an average SRV $S = 75 \text{ cm s}^{-1}$ on passivated macroporous silicon samples by fitting the model to the measurements. This surface recombination velocity was higher than the surface recombination velocity $S = 24 \text{ cm s}^{-1}$ that is measured on non-porous reference samples passivated in the same process. This discrepancy could not solely be explained by the various surface orientations. Instead, the discrepancy in the surface recombination velocity is explained with the existence of local openings in the passivating layer that are observed in SEM micrographs. However, such openings are not included in the analytical model.

In this work, a three-dimensional numerical model that accounts for the non-passivated openings is set up. Some of the results presented in this chapter have been published in Ref. [Ern12c]. The numerical model is experimentally verified by preparing macroporous silicon samples with defined openings in the passivation layer.

2.1 Sample preparation

The Si substrate used in the study of this chapter is an (100)-oriented, 150 mm, float zone, chemical mechanical polished, n-type wafer with a resistivity of $(7.5 \pm 0.1) \Omega \text{ cm}$. The thickness of the wafer is $(674 \pm 10) \mu\text{m}$.

The surface of the wafer is structured with an array of hexagonally arranged inverted pyramids as shown in Fig. 2.1. The inverted pyramids are defined by photolithography. The distance of the pyramids tips is $d_0 = 8.3 \mu\text{m}$ as measured by means of SEM micrograph analysis.

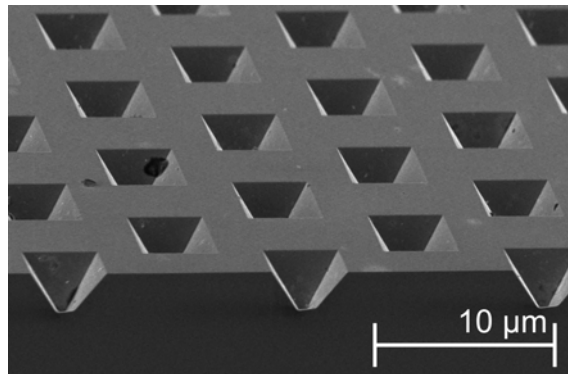


Figure 2.1: SEM micrograph showing an oblique view onto a silicon surface with inverted pyramids defined by photolithography. The distance of the pyramids tips is $8.3\ \mu\text{m}$. Figure from Ref. [Ern12c].

A phosphorus diffusion at the rear side with a sheet resistance of $40\ \Omega$ improves the contact during electrochemical etching in the $1\ \text{cm}^2$ small area etching setup. Finally, the samples are separated into $25\ \text{mm} \times 25\ \text{mm}$ -sized pieces by laser-scribing. The electrolyte is a 3 wt% aqueous hydrofluoric acid at $20\ ^\circ\text{C}$.

Figure 2.2 shows the set values of the etching current density. At a constant current density of $6\ \text{mA cm}^{-2}$, that is held for 50 min, the pores start growing at the pyramids

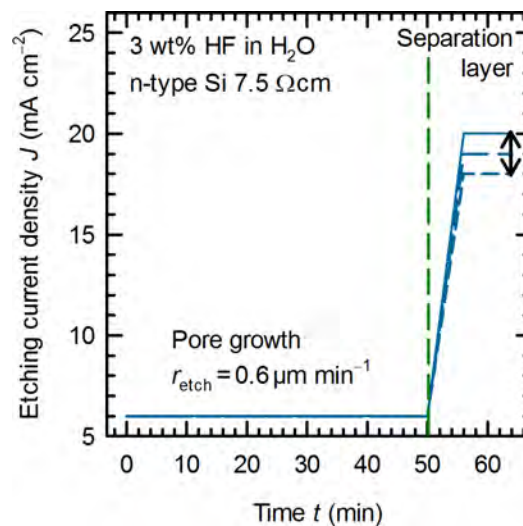


Figure 2.2: Etching current density profile to form an approximately $30\ \mu\text{m}$ thick macroporous silicon layer with a highly porous separation layer. Three different current densities between $18\ \text{mA cm}^{-2}$ (short dashed line) and $20\ \text{mA cm}^{-2}$ (solid line) are used to form the separation layer with varied porosity. Figure from Ref. [Ern12c].

tips with an etching rate of $0.6 \mu\text{m min}^{-1}$. Then, the current is increased linearly from 6 mA cm^{-2} to values of 18 mA cm^{-2} to 20 mA cm^{-2} within 6 min. At this level, the current density is maintained for 6 min to form a highly porous separation layer.

The current density and, thus, the porosity of the separation layer controls the width of weak bridges between the substrate and the separation layer.

Figure 2.3a shows a cross sectional SEM micrograph of a macroporous Si sample with a separation layer current density of 20 mA cm^{-2} . The porosity of the separation layer is 100 %, thus no weak bridges remain between the substrate and the macroporous layer. In this case, the layer is only attached to the substrate at the unetched rim of the sample. Figure 2.3b shows a SEM micrograph of the 18 mA cm^{-2} case. The width of the bridges is $\approx 800 \text{ nm}$ in this case.

In this study, three samples are prepared for each separation layer current density 18 mA cm^{-2} , 19 mA cm^{-2} and 20 mA cm^{-2} . The macroporous Si layer remains attached to the substrate.

An RCA-cleaning of the samples is followed by dry thermal oxidization in a furnace at $900 \text{ }^\circ\text{C}$ that creates a 30 nm thick passivating SiO_x -layer. Then, the samples are annealed at $400 \text{ }^\circ\text{C}$ for 90 min in forming gas (5 % H_2 :95 % N_2) atmosphere.

Finally, the surface passivated macroporous Si layers are detached from the substrate by gluing it to a glass carrier with a transparent tape and pulling it off. Consequently, non-passivated areas remain at the broken bridges. Figure 2.4a shows the substrate wafer after detachment of the macroporous Si layer. Figure 2.4b shows the macroporous Si layer that is glued to a glass carrier.

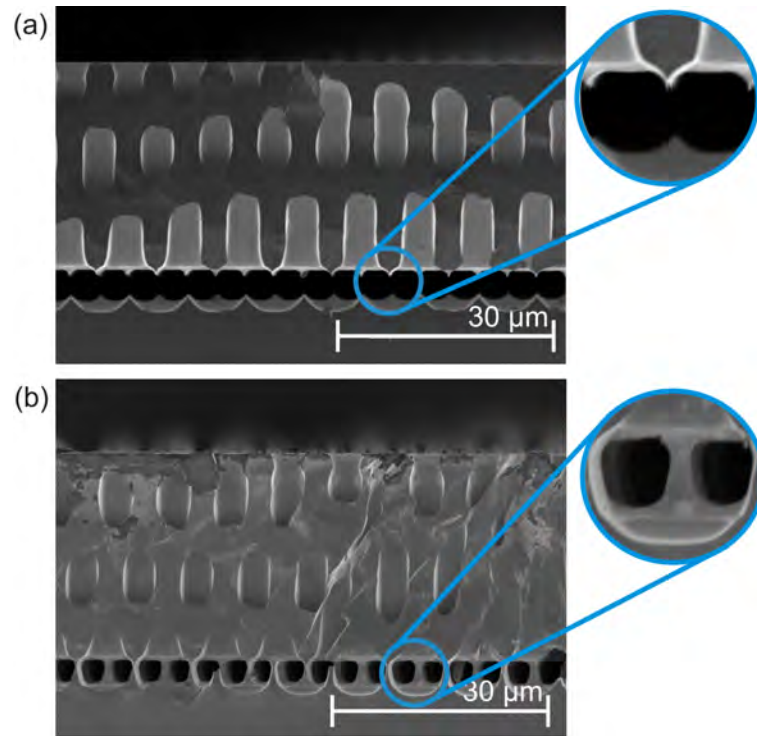


Figure 2.3: Cross sectional SEM micrographs of prepared samples with separation layer current density of (a) 20 mA cm^{-2} and (b) 18 mA cm^{-2} . The width of the weak bridges is approximately 800 nm in case (b). Figure from Ref. [Ern12c].

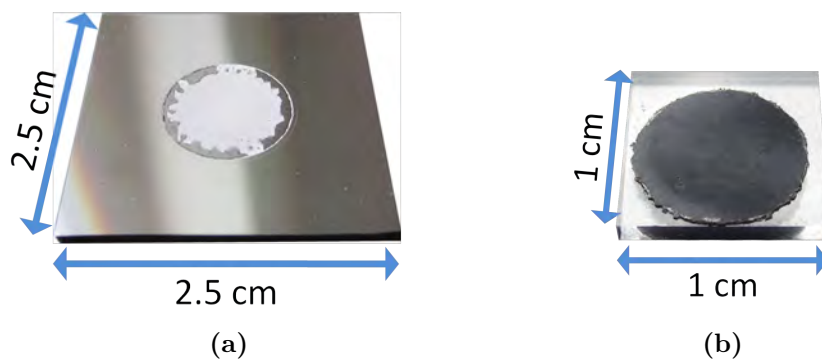


Figure 2.4: (a) Photograph of the substrate wafer after detachment of the macroporous Si layer. (b) Photograph of the macroporous Si layer glued to a glass carrier.

2.2 Experimental results

2.2.1 Geometrical analysis

The percentage Ψ of the non-passivated areas after detaching the macroporous silicon layer from the substrate is determined by means of SEM micrograph analysis. The local openings in the oxide layer are observable in the SEM micrographs presented in Fig. 2.5. In case of a final etching current density of 20 mA cm^{-2} (Fig. 2.5a) the porosity of the separation layer is 100 % and, thus, no non-passivated areas remain. The brightness and contrast of the SEM micrograph are adjusted in an image editing software (Corel Photo-Paint X4) to enhance the contrast between the passivated and non-passivated areas. Passivated and non-passivated areas appear as white and black areas, respectively. Since pores and non-passivated areas both appear black, the non-passivated areas are colorized green within the image editing software as shown in Fig. 2.6. The quotient of the number of green pixels to the number of total pixels defines the percentage Ψ of the non-passivated areas. Furthermore, the geometrical parameters of the macroporous layers are measured from cross sectional SEM micrographs as listed in Table 2.1.

2.2.2 Effective carrier lifetime

The minority carrier lifetimes of detached passivated macroporous silicon layers are measured using light-biased transient microwave detected photoconductance decay (MW-PCD, WT-2000 system from Semilab) technique. Bias illumination comes from a light bulb. The samples are illuminated from the side that was facing to the substrate prior to detachment. The optical absorption length of the $\lambda = 904 \text{ nm}$ short pulse laser is approximately $30 \mu\text{m}$ in crystalline silicon and, thus, comparable to the layer thickness.

Table 2.1: Percentage of the non-passivated areas and geometrical parameters of the macroporous layer.

Parameter	Symbol	Value
Percentage of the non-passivated areas for 20 mA cm^{-2}	Ψ_1	0 %
Percentage of the non-passivated areas for 19 mA cm^{-2}	Ψ_1	$(0.75 \pm 0.20) \%$
Percentage of the non-passivated areas for 18 mA cm^{-2}	Ψ_1	$(1.6 \pm 0.2) \%$
Thickness of the macroporous layer	W	$(29 \pm 1) \mu\text{m}$
Pore radius	r_p	$(2.4 \pm 0.1) \mu\text{m}$
Pore distance	d_0	$(8.3 \pm 0.1) \mu\text{m}$

Figure 2.7 shows the measured effective carrier lifetimes (dots) for various percentages of non-passivated areas. The mean value of the effective lifetimes is calculated from a set of three samples for each percentage of the non-passivated areas. Note that the experimental points cover the experimentally feasible range due to limits in sample preparation. A relative error in lifetime measurement of 5% is assumed. The highest effective lifetime measured is $\tau_{\text{eff}} = (10.1 \pm 0.5) \mu\text{s}$ for a fully passivated sample.

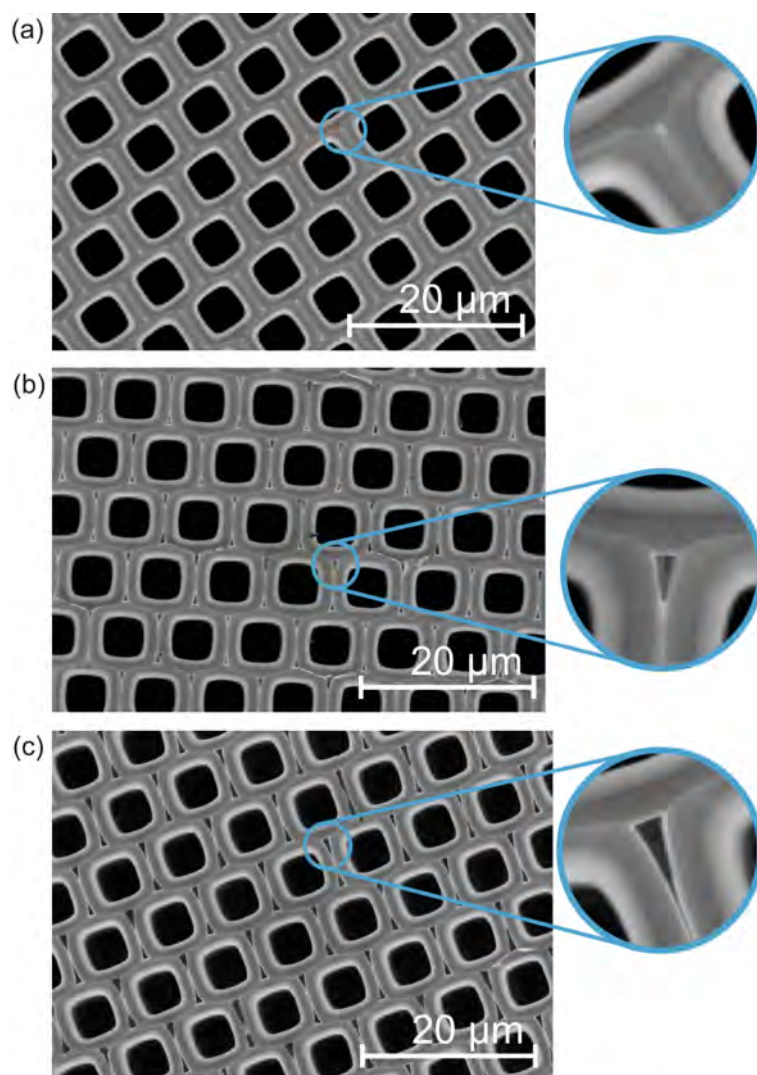


Figure 2.5: Top view SEM micrographs of surface passivated macroporous layers showing the surface facing the substrate prior to detachment. The etching current density for the separation layer is (a) 20 mA cm^{-2} , (b) 19 mA cm^{-2} and (c) 18 mA cm^{-2} . The non-passivated areas are visible in the magnifications. Figure from Ref. [Ern12c].

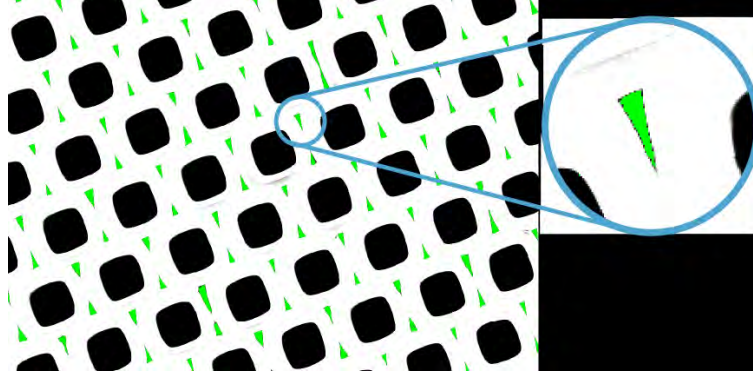


Figure 2.6: Resulting SEM micrograph after image processing and coloring the non-passivated areas in green. Figure from Ref. [Ern12c].

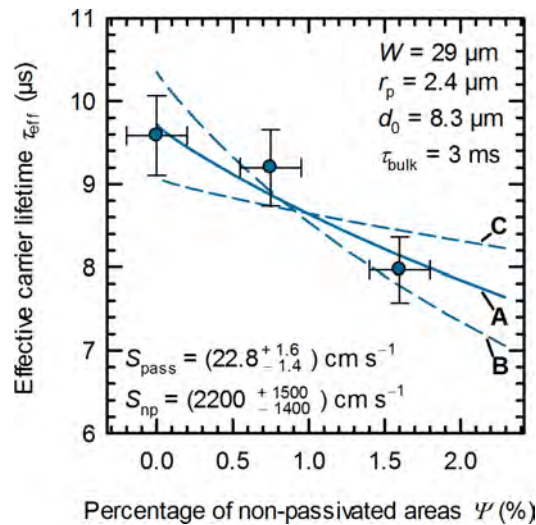


Figure 2.7: Measured effective carrier lifetimes τ_{eff} of passivated and detached macroporous silicon layers (dots) and numerical simulations (lines) as a function of the percentage Ψ of non-passivated areas. The solid line A is the numerical simulation for the SRV given in the figure. The dashed lines B and C show numerical simulations for the upper and lower boundaries of S_{pass} and S_{np} . Figure from Ref. [Ern12c].

2.3 Numerical modeling

A numerical finite element model that accounts for the geometrical properties of macroporous silicon to determine the average SRV at the passivated and non-passivated areas is set up in COMSOL Multiphysics [COM12]. In the following sections, the numerical model is applied to describe the measurements and simulate the effect of geometrical and electrical parameters on the effective carrier lifetime.

2.3.1 Geometry

Figure 2.8 schematically shows the hexagonal pattern of the macroporous structure with a pore distance d_0 . For the numerical model, cylindrical pores with radius r_p and smooth surfaces are assumed. One unit cell is extruded from the triangular base with the thickness W . The increased pore radius of the separation layer is approximated by subtracting three spheres at the top of the unit volume. The centers of the spheres lie on the pores axis. The breaking point of the weak bridge is marked in red in Figure 2.8 (d). Increasing the spheres radius leads to thinner bridges. This variation in the spheres radius corresponds to an experimental variation of the separation layer current density.

2.3.2 Equations and boundary conditions

The inhomogeneous steady-state diffusion equation for the minority carriers is given by

$$\vec{\nabla} \left(-D_p \vec{\nabla} p \right) = G - \frac{p}{\tau_{p,\text{bulk}}}. \quad (2.1)$$

Here D_p is the diffusion coefficient of the minority carriers, p the excess carrier density, and $\tau_{p,\text{bulk}}$ the minority carrier bulk lifetime. The generation rate G is assumed to be spatially homogeneous, since the optical absorption length of the short pulse laser used in the measurements is comparable to the layer thickness.

In Fig. 2.9 the surfaces exhibiting identical boundary conditions are marked in identical colors schematically. The average surface recombination velocity is S_{pass} for the surface passivated areas as shown in Fig. 2.9a of the macroporous layer, thus

$$\vec{n} D_p \vec{\nabla} p = -S_{\text{pass}} p. \quad (2.2)$$

Here \vec{n} is a unit vector perpendicular to the respective surface. The surface recombination velocity for the non-passivated areas as marked in red in Fig. 2.9b is S_{np} , thus

$$\vec{n} D_p \vec{\nabla} p = -S_{\text{np}} p. \quad (2.3)$$

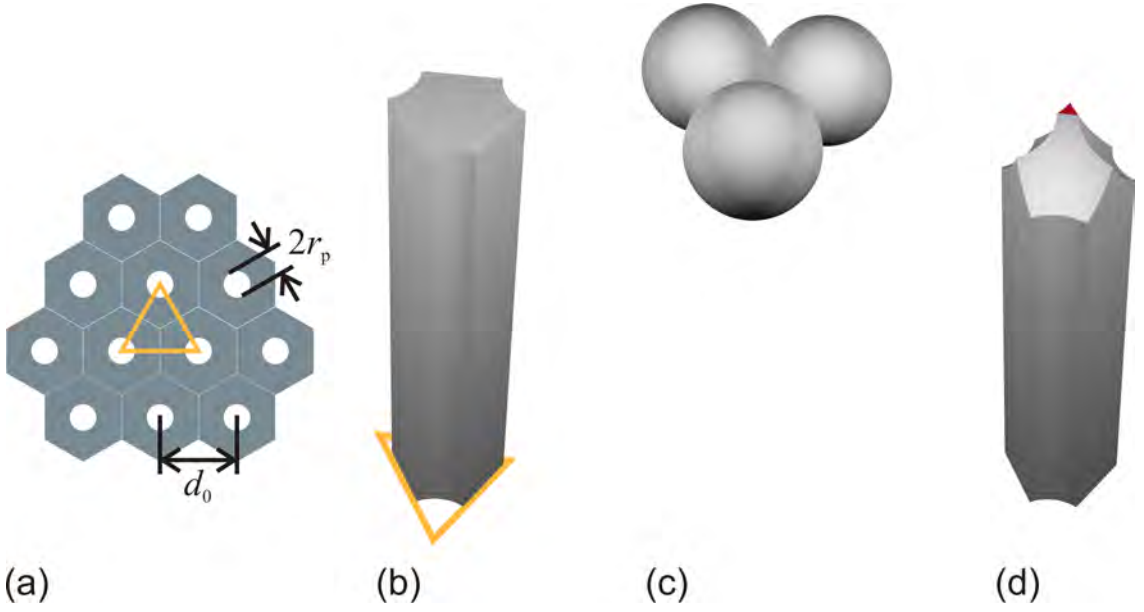


Figure 2.8: (a) Schematic of the hexagonal array with pore distance d_0 and pore diameter $2r_p$. The orange triangular defines the unit cell used in the numerical simulations. (b) Extruded unit volume with thickness W . (c) The separation layer is approximated by subtracting three spheres from the extruded unit volume. The spheres centers lie in the pores axis. (d) The area highlighted in red corresponds to the non-passivated areas of the passivated and detached macroporous silicon samples. Figure from Ref. [Ern12c].

For symmetry reasons the perpendicular component of the derivate $\vec{\nabla}p$ vanishes for the boundaries shown in Fig. 2.9c, thus

$$\vec{n}D_p\vec{\nabla}p = 0. \quad (2.4)$$

The average excess carrier density p_{av} is calculated by integrating the local excess carrier densities over the unit volume:

$$p_{av} = \frac{1}{V} \int_V p(\vec{x}) d^3x. \quad (2.5)$$

The effective minority carrier lifetimes under steady state conditions is calculated by dividing the average excess carrier density and the average carrier generation rate G that is assumed to be spatially homogeneous:

$$\tau_{eff}(p_{av}) = \frac{p_{av}}{G}. \quad (2.6)$$

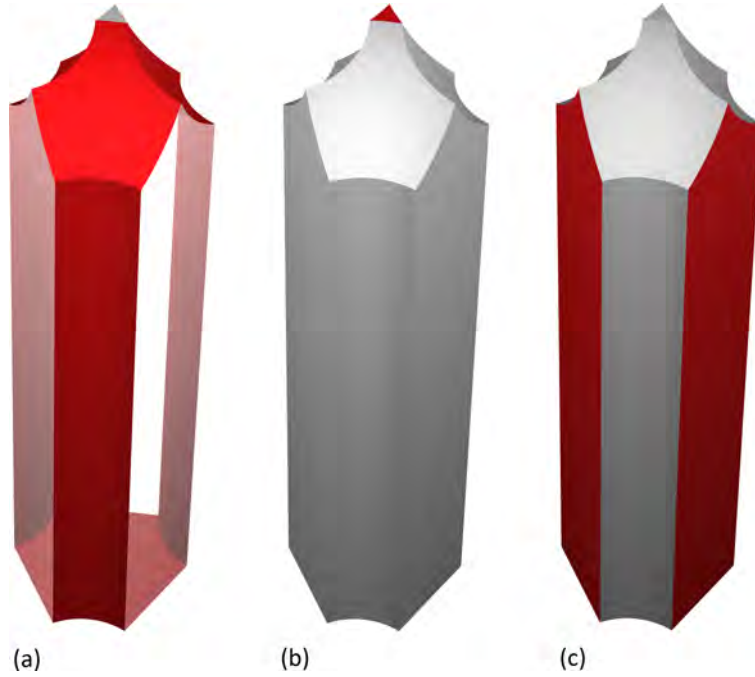


Figure 2.9: Boundary conditions for the unit cell highlighted in red: (a) Passivated surfaces with an SRV S_{pass} . (b) Non-passivated surface with SRV S_{np} . (c) Symmetric boundary conditions. Figure from Ref. [Ern12c].

2.3.3 Experimental verification

With the above model, the effective carrier lifetimes is calculated as a function of the percentage of the non-passivated areas. The geometric parameters of the macroporous layers are those listed in Table 2.1. A bulk lifetime of $\tau_{\text{p,bulk}} = 3 \text{ ms}$ typical for lowly doped n-type Si substrates and the diffusion coefficient $D_{\text{p}} = 12 \text{ cm s}^{-1}$ is used.

The model is fitted to the measured carrier lifetimes by varying the surface recombination velocities S_{pass} of the passivated areas and S_{np} of the non-passivated areas. The mean average percentage error Δ between the calculated curve and the measurements calculates as:

$$\Delta = \frac{1}{3} \sum_{i=1}^3 \left| \frac{\tau_{i,\text{sim}} - \tau_{i,\text{exp}}}{\tau_{i,\text{exp}}} \right|. \quad (2.7)$$

Figure 2.10 shows this error as a function of a S_{pass} and S_{np} in a contour plot. At the minimum of Δ (dot A) the average surface recombination velocity for the passivated surfaces is $S_{\text{pass}} = (22.8^{+1.6}_{-1.4}) \text{ cm s}^{-1}$ and $S_{\text{np}} = (2200^{+1500}_{-1400}) \text{ cm s}^{-1}$ for the non-passivated surface within an experimental error of $\Delta < 5\%$. The resulting uncertainty of S_{pass} is approximately 7%. This high accuracy is due to the strong dependence of the effective

carrier lifetime on the surface recombination velocity that originates from the large passivated surface area. The uncertainty of S_{np} is approximately 70%. This large relative error results from the fact, that the non-passivated area fraction is small with respect to the total area. The dots B and C lie inside the uncertainty range of S_{pass} and S_{np} , respectively.

Figure 2.7 shows the measured effective carrier lifetimes (dots) and the numerical simulations (lines) as a function of the percentage of non-passivated areas. The numerical simulations agree with the experimental data within the uncertainty range of the experimental data. Line A is the numerical simulation with S_{pass} and S_{np} for the minimum of Δ (dot A in Fig. 2.10). The dashed lines B and C show the 5% uncertainty in Δ of the numerical simulations for S_{pass} and S_{np} .

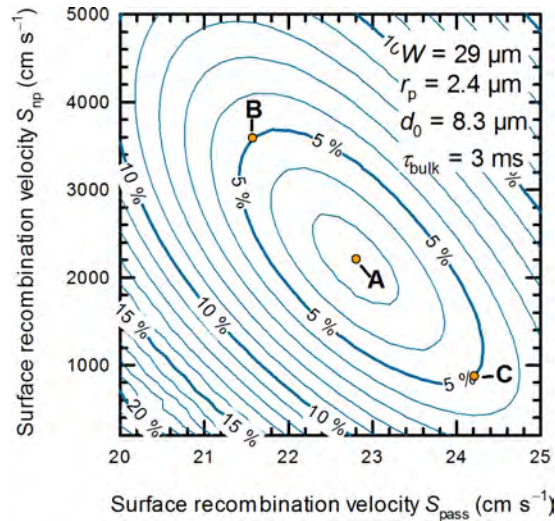


Figure 2.10: Contour plot of the mean average percentage error Δ evaluated between the fit and experimental data for various surface recombination velocities. Within a deviation of $< 5\%$ $S_{pass} = (22.8^{+1.6}_{-1.4}) \text{cm s}^{-1}$ for the passivated surfaces and $S_{np} = (2200^{+1500}_{-1400}) \text{cm s}^{-1}$ for the non-passivated surface. Figure from Ref. [Ern12c].

2.4 Impact of various parameters on the effective carrier lifetime

Table 2.2 summarizes the set of input parameters and constant values used in the simulations. Each of the input parameters is varied separately using the variation range specified in Table 2.2 for three constant percentages Ψ of the non-passivated areas.

2.4.1 Impact of the bulk lifetime τ_{bulk}

Figure 2.11a shows the effective carrier lifetimes (lines) of passivated macroporous silicon layers calculated for three percentages of the non-passivated areas. The dots show the measured carrier lifetimes from the previous section. The effective lifetime is almost independent of the bulk lifetime for values greater than 100 μs and thus does not limit the effective carrier lifetime.

Experimentally, the electrochemical formation of macropores requires bulk lifetimes in the range of few hundred μs since the holes generated at the rear side have to diffuse to the etching front. Typically, n-type CZ wafers have bulk lifetimes greater than 1 ms. Thus, the influence of the bulk lifetime on the effective carrier lifetime is negligible in all realistic cases.

2.4.2 Impact of the layer thickness W

Since the effective lifetime depends on bulk and surface recombination, a strong impact of the layer thickness on the effective lifetime is expected. The volume to surface ratio is affected by the layer thickness and, thus, higher effective carrier lifetimes for thicker layers are expected. The calculated effective carrier lifetimes as a function of the layer thickness (lines in Figure 2.11b) show the expected behaviour. The experimental data is

Table 2.2: Set of input parameters for the three-dimensional numerical model.

Parameter	Symbol	Default value	Variation range
Bulk lifetime	τ_{bulk}	3 ms	0.01 ms to 10 ms
Layer thickness	W	29 μm	10 μm to 100 μm
Pore radius	r_{p}	2.4 μm	1 μm to 4 μm
Pore distance	d_0	8.3 μm	6 μm to 11 μm
Percentage of the non-passivated areas	$\Psi_{1,2,3}$	0 %, 0.75 % and 1.6 %	held constant
SRV of the passivated surface	S_{pass}	22.8 cm s^{-1}	0.01 cm s^{-1} to 200 cm s^{-1}
SRV of the non-passivated surface	S_{np}	2200 cm s^{-1}	10^0 cm s^{-1} to 10^7 cm s^{-1}
Diffusion coefficient	D_{p}	12 $\text{cm}^2 \text{ s}^{-1}$	held constant

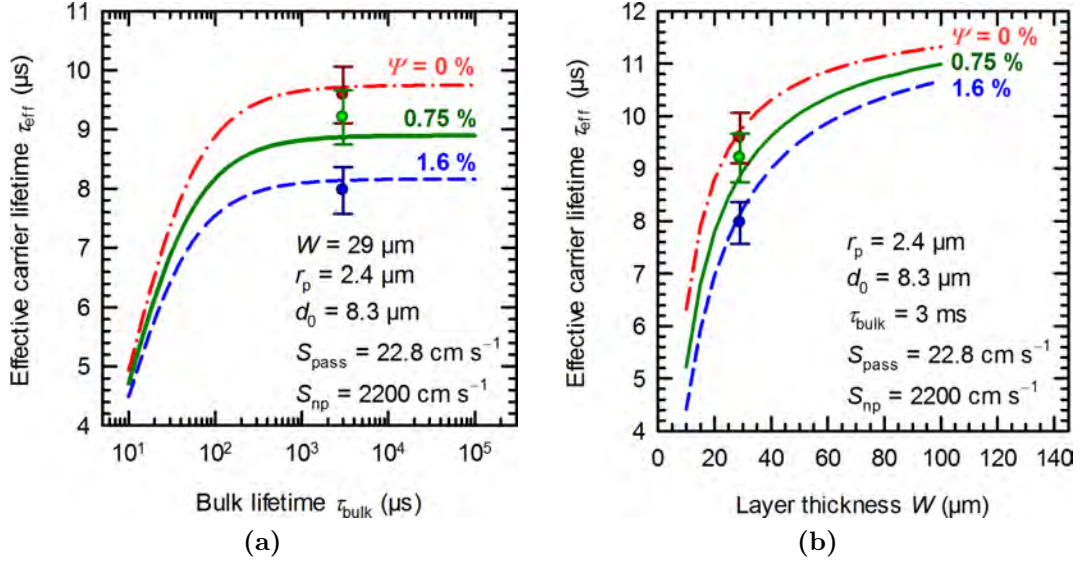


Figure 2.11: (a) Effective carrier lifetime as a function of bulk lifetime τ_{bulk} . (b) Effective carrier lifetime as a function of layer thickness W . Lines: Numerical simulations. Dots: Measurement.

shown as dots. The steepest increase in lifetime appears for thickness values below $30 \mu\text{m}$. For higher thickness the carrier lifetime approaches an upper limit, since the influence of the surface recombination at the top and bottom of the layer decreases. Hence, a layer thickness around $30 \mu\text{m}$ is an appropriate trade-off between material savings and carrier lifetime.

2.4.3 Impact of pore radius r_p and pore distance d_0

Pore radius as well as pore distance strongly affect the volume to surface ratio of macroporous Si layers. Thus, a decreasing effective carrier lifetime with increasing pore radius for a constant pore distance and an increasing effective carrier lifetime with increasing pore distance for a constant pore radius is expected.

The numerical calculations depicted in Figure 2.12a and Figure 2.12b show the expected impact of both parameters on the effective carrier lifetime. High effective carrier lifetimes require a small pore radius and a large pore distance.

Experimentally, the pore radius has a lower limit which is influenced by the viscosity of the electrolyte. The pore distance has an upper limit depending on the doping concentration and the necessity to form a highly porous separation layer [Leh97].

Effective carrier lifetimes up to $10 \mu\text{s}$ are measured for the macroporous Si layers prepared for the study in this chapter. By reducing the etching current density and, thus, the

pore radius effective carrier lifetimes $> 20 \mu\text{s}$ can be achieved for the same average surface recombination velocity.

2.4.4 Impact of surface recombination velocity S_{pass}

The surface to volume ratio of macroporous silicon samples prepared in this work is about 8 times larger compared with non-porous reference samples. Thus, it is not surprising that the effective carrier lifetime shows a strong dependence on the surface recombination velocity S_{pass} . Figure 2.13a shows the effective carrier lifetime as a function of the SRV S_{pass} . The slopes of the three curves converge at higher surface recombination velocities, where the influence of the non-passivated areas decreases. This steep correlation between the effective carrier lifetime and SRV S_{pass} results in a small uncertainty of the fitted S_{pass} as mentioned above.

2.4.5 Impact of surface recombination velocity S_{np}

Figure 2.13b shows the dependence of the effective carrier lifetime as a function of the SRV S_{np} of the non-passivated area. If the SRV of the non-passivated area is close to the SRV of the passivated surfaces the effective carrier lifetime approaches the effective carrier lifetime of the fully-passivated sample. For values $S_{\text{np}} < 10^3 \text{ cm s}^{-1}$ and $S_{\text{np}} > 10^5 \text{ cm s}^{-1}$ the curve progression is flattened and, thus, the influence of S_{np} on the effective carrier lifetime is reduced.

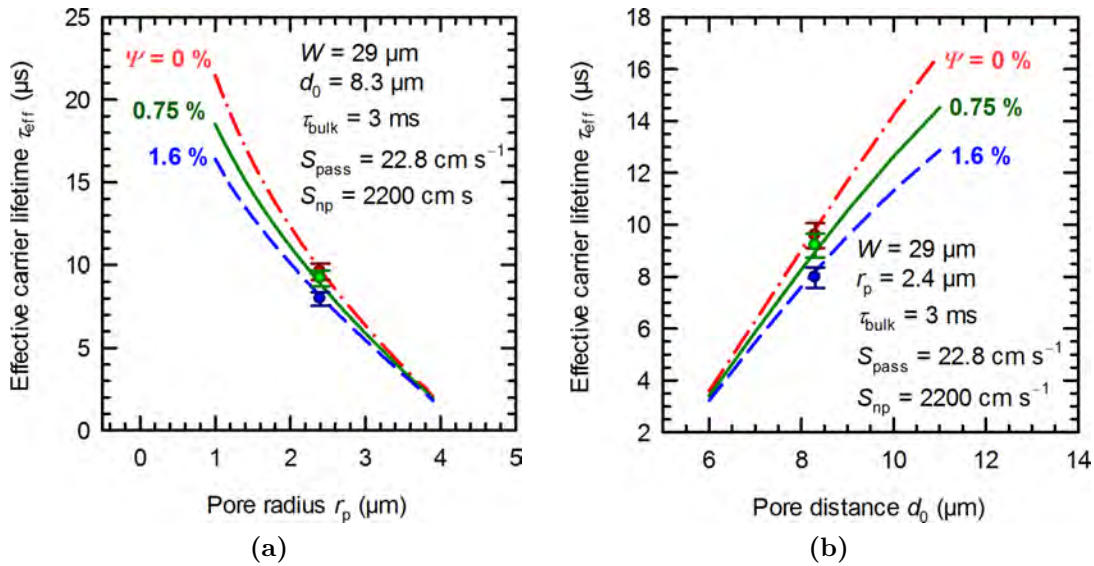
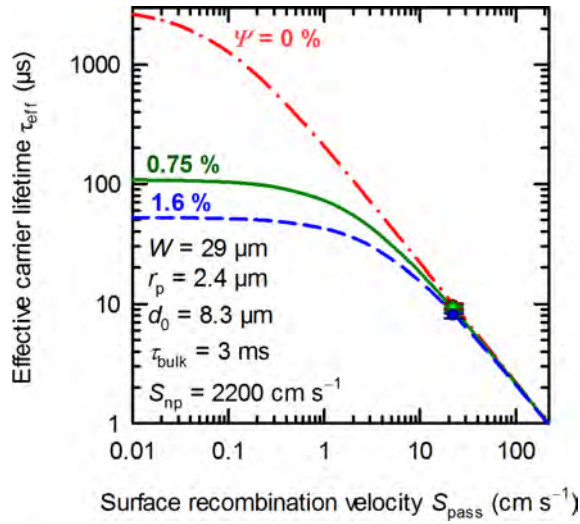
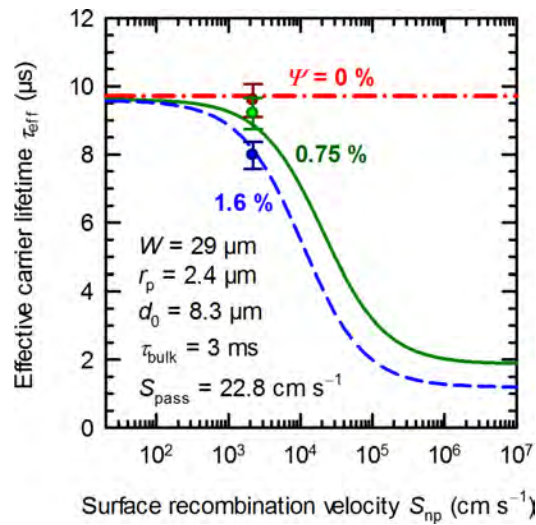


Figure 2.12: (a) Effective carrier lifetime as a function of pore radius r_p . (b) Effective carrier lifetime as a function of pore distance d_0 . Lines: Numerical simulations. Dots: Measurement.



(a)



(b)

Figure 2.13: (a) Effective carrier lifetime as a function of surface recombination velocity S_{pass} of passivated areas. (b) Effective carrier lifetime as a function of surface recombination velocity S_{np} of non-passivated areas. Lines: Numerical simulations. Dots: Measurement.

2.5 Conclusion

This chapter demonstrated the preparation of point contact openings in surface passivated macroporous Si layers. The percentage of these non-passivated local openings is experimentally varied in a range from 0 % to 1.6 % by controlling the etching parameters. The highest lifetime measured is $(10.1 \pm 0.5) \mu\text{s}$ for a fully oxide passivated $(29 \pm 1) \mu\text{m}$ -thick macroporous silicon layer.

A three-dimensional finite element numerical model is developed to determine the surface recombination velocities of the macroporous surfaces and the local openings. The model agrees with the measurements within the measurement accuracy. The average surface recombination velocity for the passivated surfaces is $S_{\text{pass}} = (22.8_{-1.4}^{+1.6}) \text{ cm s}^{-1}$ and $S_{\text{np}} = (2200_{-1400}^{+1500}) \text{ cm s}^{-1}$ for the non-passivated surface. Thus, the postulated reason for the discrepancy between the average surface recombination velocity of the analytical model and reference measurements from Ref. [Ern11] is verified and explained with the non-passivated areas.

The surface recombination velocity S_{np} determined for the non-passivated areas is surprisingly low. However, for low doping densities of $6 \times 10^{14} \text{ cm}^{-3}$ as in the case of this work, Mäkel and Cuevas [Mäc03] found effective surface recombination velocities from $1 \times 10^3 \text{ cm s}^{-1}$ to $3 \times 10^4 \text{ cm s}^{-1}$ for non-passivated surfaces depending on storage time after HF dip. This measurement is consistent with the results of this chapter.

3 | Optical characterization

Low surface reflection and efficient light trapping [Cam87, Cam90, Cam93] are required to achieve high energy conversion efficiencies. Lambertian light trapping [Goe81, Yab82] has for long been a benchmark for efficient light trapping [Tie84, Cam87]. This chapter quantifies the degree of Lambertian light trapping in macroporous Si. Some of the results presented here are submitted in Ref. [Ern13b].

Since solar cells will have a back reflector, anti-reflection coating, and free-carriers in highly doped regions, the absorption in the macroporous Si layer cannot be easily determined. Therefore, the hemispherical reflection of macroporous Si is measured without an anti-reflection coating and highly doped regions with well characterized back reflectors. An analytical model is used to describe the measurements. The model then yields the absorption in the macroporous Si layer and the back reflector separately.

The reflection of two types of macroporous Si samples is measured using a spectrophotometer with an integrating sphere. Both samples are free-standing macroporous Si layers. The pores of the first sample are hexagonally arranged and the pores of the second sample are randomly arranged.

3.1 Sample preparation

The two macroporous Si layers of this chapter are fabricated using the large area etching setup. One of the wafers is hexagonally pre-structured with inverted pyramids as described in Section 1.5. Electrochemical etching of the second wafer with a planar surface yields randomly arranged pores.

An etching current density of 6 mA cm^{-2} for 40 min creates the low-porosity absorber layer of the pre-structured wafer. The bias voltage is constant at 2 V.

Increasing of the etching current density to 25 mA cm^{-2} within 6 min forms the highly porous separation layer. The voltage is simultaneously increased to 5 V. This current and voltage is then maintained for 12 min to form a cavity underneath the absorber layer.

In case of the planar wafer etching starts with an etching current density of 8 mA cm^{-2} and a voltage of 2 V for 55 min. The current density and the bias voltage is increased to 26 mA cm^{-2} and 4 V within 10 min, respectively. The current and voltage is maintained for 4.5 min.

Applying mechanical force using a razor blade removes the macroporous Si layer from the substrate. The macroporous Si samples are free-standing and approximately 100 cm^2 -sized.

3.2 Structural analysis

Figures 3.1a and 3.1b show SEM micrographs of the “textured” side of a macroporous silicon layer with a hexagonally ordered array of macropores and with a random pore distribution, respectively. The “textured” side is the side which was facing the substrate prior to detachment.

Figures 3.2a and 3.2b show the side that was facing the electrolyte during electrochemical etching (described in Chapter 1). The surface of this side appears more smooth than the textured side in particular for the ordered array of macropores.

Figures 3.3a and 3.3b show cross sectional SEM-images of a macroporous Si layer with hexagonally ordered macropores and randomly distributed macropores, respectively. The openings at the front side are tapered due to the increase of the etching current density during separation layer formation. At the rear side where the pores started growing the pores are shaped like the neck of a bottle.

The pore morphology is determined by means of SEM micrograph analysis. The average pore distance is determined from top view SEM micrographs by averaging the distance of at least 15 pores. The average pore diameter of at least 15 pores and thickness at not less than 5 positions is measured in cross sectional SEM micrographs.

The thickness W of the macroporous silicon layer with hexagonally arranged pores is $(34 \pm 2) \mu\text{m}$. With a pore distance $d_0 = 8.0 \mu\text{m}$ and an average pore diameter of $2r_p = (4.0 \pm 0.2) \mu\text{m}$. This yields a porosity of $p = (22.7 \pm 2.3) \%$ and, thus, an effective thickness $W_{\text{eff}} = (26.3 \pm 1.7) \mu\text{m}$ is calculated using Eq. 1.11.

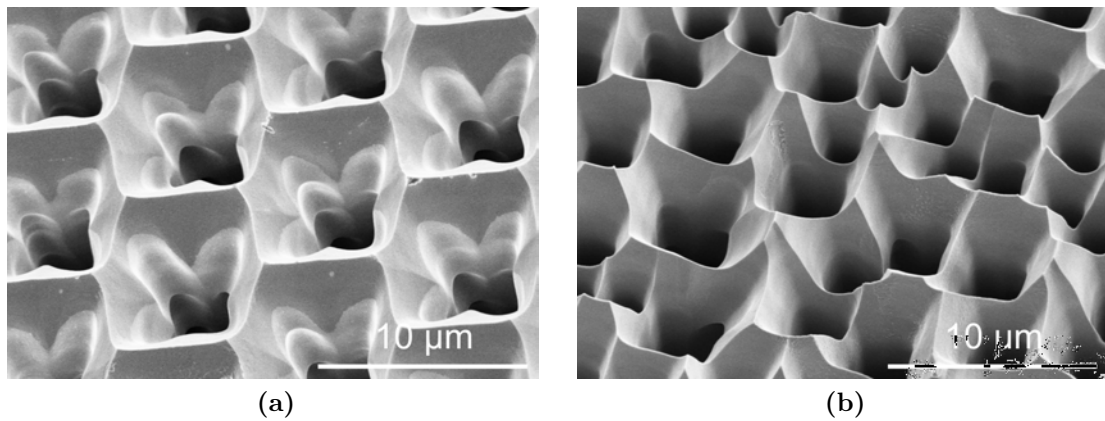


Figure 3.1: 30° tilted top view SEM micrographs of the “textured” front side of macroporous silicon layers with (a) a hexagonally ordered macropores and (b) with randomly distributed macropores. Figure from Ref. [Ern13b].

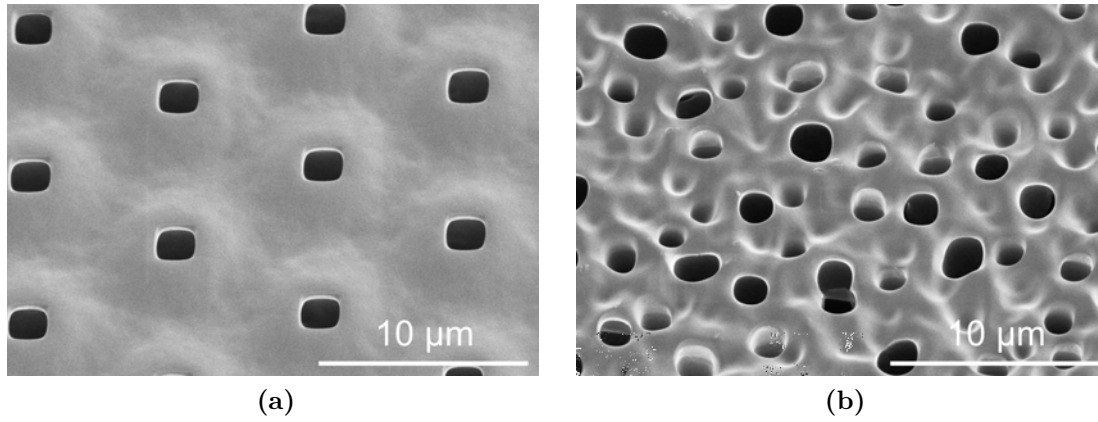


Figure 3.2: 30° tilted top view SEM micrographs of the rear side of macroporous silicon layers with (a) a hexagonally ordered macropores and (b) with randomly distributed macropores.

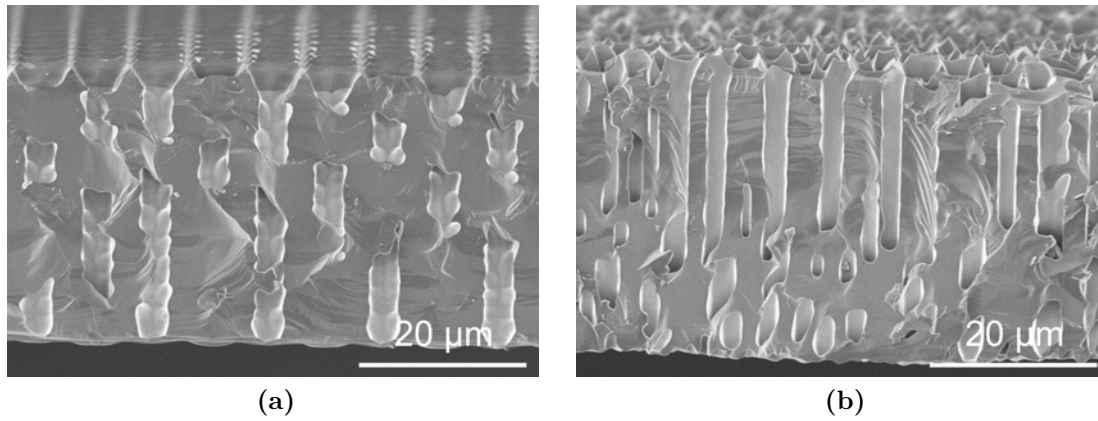


Figure 3.3: Cross sectional SEM micrographs of macroporous silicon layers with (a) a hexagonally ordered macropores and (b) with randomly distributed macropores.

The sample with a random pore arrangement is (35 ± 2) μm -thick and has an average pore distance $d_0 = (4.5 \pm 1.2)$ μm . The average pore diameter is $2r_p = (2.3 \pm 0.4)$ μm . Hence, the porosity is $p = (23.7 \pm 15.1)$ % and the effective thickness is $W_{\text{eff}} = (26.7 \pm 5.5)$ μm .

3.3 Optical measurement setup

The commercial measurement setup (Cary 5000 from Varian) consists of a deuterium (185 nm to 350 nm) and halogen (350 nm to 3300 nm) light source and a double Littrow monochromator. The monochromatic light beam is split into two separate beams using a chopper at a frequency of 30 Hz.

Figure 3.4 illustrates the integrating sphere of the spectrophotometer (view from top into the sphere).

The sample beam hits the sample under an angle of 8° to the surface normal at the sample port. The sample port opening is circular with a diameter of 38 mm. The spot size of the sample beam is square with an edge length of $3\text{ mm} \times 3\text{ mm}$. An additional back reflector can optionally be placed behind the sample. The reference beam is directed to a diffuse reflection standard. The reflection of this reflection standard is similar to the spheres reflection. Baffles in the integrating sphere shield the detectors from the directly illuminated parts of the sphere.

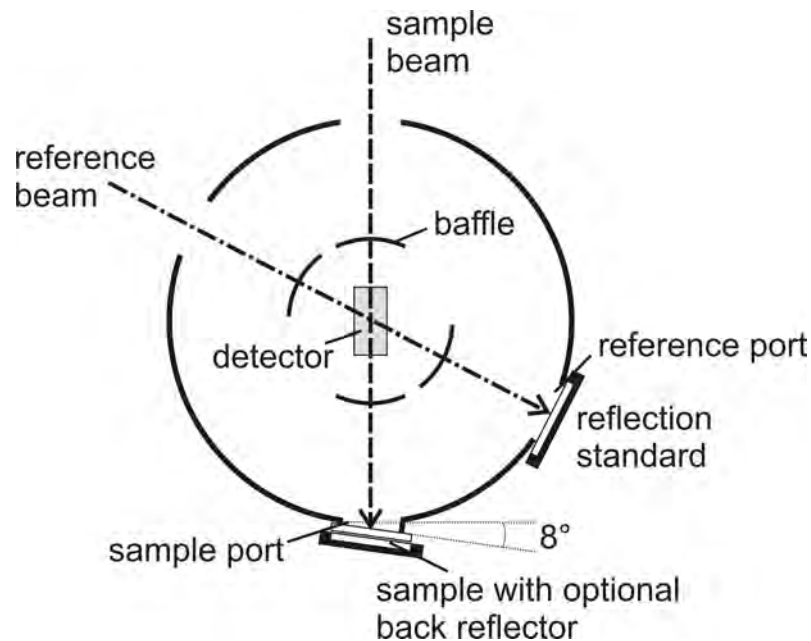


Figure 3.4: Illustration of the integrating sphere of the spectrophotometer.

3.4 Measurement theory

In order to determine the absolute reflection of a sample, three measurements (each consisting of two data sets) are required.

The known reflection ρ_{ref} of the reflection standard is similar to the reflection of the sphere. The reflection standard remains at the reference port for all measurements.

For calibration the integrating sphere, a calibrated normal with a known reflection ρ_N is first placed at the sample port. The detector signals S_N of the sample beam and $S_{\text{ref},N}$ of the reference beam are measured with the calibrated normal at the sample port. The mean reflectivity $\bar{\rho}$ of the integrating sphere then is

$$\bar{\rho} = (1 - f_0 - f_N - f_{\text{ref}}) \rho_w + f_N \rho_N + f_{\text{ref}} \rho_{\text{ref}}. \quad (3.1)$$

Here f_0 is the area fraction of both entrance ports, f_N is the area fraction of the sample port with ρ_N the reflection of the calibrated normal, ρ_w is the reflection of the sphere wall, and f_{ref} is the area fraction of the reference port with ρ_{ref} the reflection of the reflection standard.

The total energy flux Φ_t for the energy flux Φ_0 of the sample beam is

$$\Phi_t = \Phi_0 \rho_N + \Phi_0 \rho_N \sum_{i=1}^{\infty} \bar{\rho}^i = \Phi_0 \rho_N + \Phi_0 \rho_N \frac{\bar{\rho}}{1 - \bar{\rho}}. \quad (3.2)$$

Since a baffle shields the detectors from the first reflection, only subsequent reflections can be detected. Thus, the detector signal S_N for the sample beam and a detector efficiency η_1 is

$$S_N \propto \eta_1 \Phi_0 \rho_N \frac{\bar{\rho}}{1 - \bar{\rho}}. \quad (3.3)$$

Here $\frac{\bar{\rho}}{1 - \bar{\rho}}$ is the sphere multiplier that depends on the mean reflectivity $\bar{\rho}$ of the integrating sphere.

The detector signal $S_{\text{ref},N}$ for the reference beam is derived similarly, thus

$$S_{\text{ref},N} \propto \eta_2 \Phi_{\text{ref}} \rho_{\text{ref}} \frac{\bar{\rho}_N}{1 - \bar{\rho}_N}. \quad (3.4)$$

Since the detector efficiency possibly depends on the position of the first reflection, a detector efficiency η_2 is required.

Dividing of S_N and $S_{\text{ref},N}$ eliminates the sphere multiplier:

$$\frac{S_N}{S_{\text{ref},N}} = \frac{\eta_1 \Phi_0 \rho_N}{\eta_2 \Phi_{\text{ref}} \rho_{\text{ref}}}. \quad (3.5)$$

The second measurement a dark room replaces the calibrated normal at the sample port, in order to measure the background signal. The baseline correction yields a similar result to Eq. 3.5 and is

$$\frac{S_{\text{baseline}}}{S_{\text{ref,baseline}}} = \frac{\eta_1 \Phi_0 \rho_{\text{baseline}}}{\eta_2 \Phi_{\text{ref}} \rho_{\text{ref}}}. \quad (3.6)$$

Here, ρ_{baseline} is the reflection of the dark room, S_{baseline} and $S_{\text{ref,baseline}}$ are the measured detector signals of the sample and reference beam, respectively.

Finally, the sample to be measured with the reflection ρ_{sample} is placed at the sample port. The detector signals S_{sample} of the sample beam and $S_{\text{ref,sample}}$ of the reference beam then yields

$$\frac{S_{\text{sample}}}{S_{\text{ref,sample}}} = \frac{\eta_1 \Phi_0 \rho_{\text{sample}}}{\eta_2 \Phi_{\text{ref}} \rho_{\text{ref}}}. \quad (3.7)$$

From these three measurements, the absolute reflection ρ_{sample} of the sample can be calculated for a known reflection ρ_{N} as

$$\rho_{\text{sample}} = \frac{\left(\frac{S_{\text{sample}}}{S_{\text{ref,sample}}} - \frac{S_{\text{baseline}}}{S_{\text{ref,baseline}}} \right)}{\left(\frac{S_{\text{N}}}{S_{\text{ref,N}}} - \frac{S_{\text{baseline}}}{S_{\text{ref,baseline}}} \right)}. \quad (3.8)$$

3.5 Measurement results

3.5.1 Reflection of back reflectors

Figure 3.5a shows a detailed view of the macroporous Si sample with a back reflector. In this work, six diffuse Spectralon® reflectors are placed behind the sample. In one case, the space behind the sample is a dark room.

Figure 3.5b shows a photograph of the six back reflectors.

The reflection of the back reflectors and the dark room is measured separately. Figure 3.6 shows the measurement of the diffuse reflectors with a nominal reflection $R_{\text{ref}} = 0.10, 0.20, 0.40, 0.60, 0.80$ and 0.99 . The reflection of the dark room is denoted with $R_{\text{ref}} = 0.00$

3.5.2 Front side reflection

Figures 3.7a and 3.7b show the total reflection of the measurement (dots) for the macroporous samples with hexagonally arranged pores and randomly distributed pores for the rear reflector with $R_{\text{ref}} = 0.99$, respectively. Despite the missing anti-reflection coating the reflection is remarkably low for wavelength $\lambda < 900$ nm. For wavelengths $\lambda > 850$ nm silicon becomes transparent. Thus, the measured reflection increases since it does not solely consists of the front surface reflection.

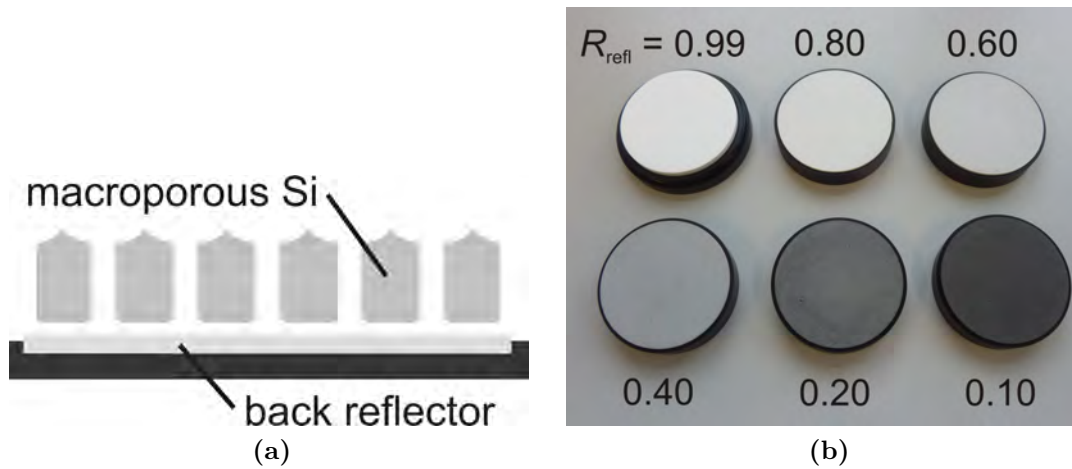


Figure 3.5: (a) Sketch of the macroporous Si sample with diffuse back reflector. (b) Photograph of the six diffuse back reflectors.

The front reflection $R_{\text{front}} = (1 - T_{\text{front}})$ is required for analytical modeling the absorption. T_{front} is the transmission at the front side of the sample. The front reflection $R_{\text{front}} = (1 - T_{\text{front}})$ equals the measured total reflection R for wavelengths $\lambda \leq 850$ nm. Since silicon is non-transparent for wavelengths $\lambda \leq 850$ nm, an analytical fit extrapolates the front side reflection for these wavelengths.

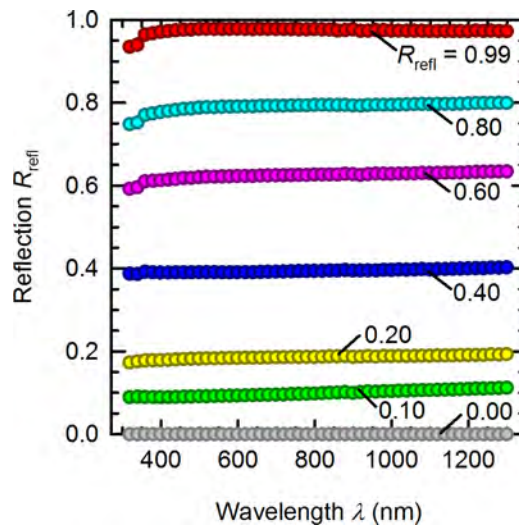


Figure 3.6: Measured hemispherical reflection of the six diffuse back reflectors and the dark room.

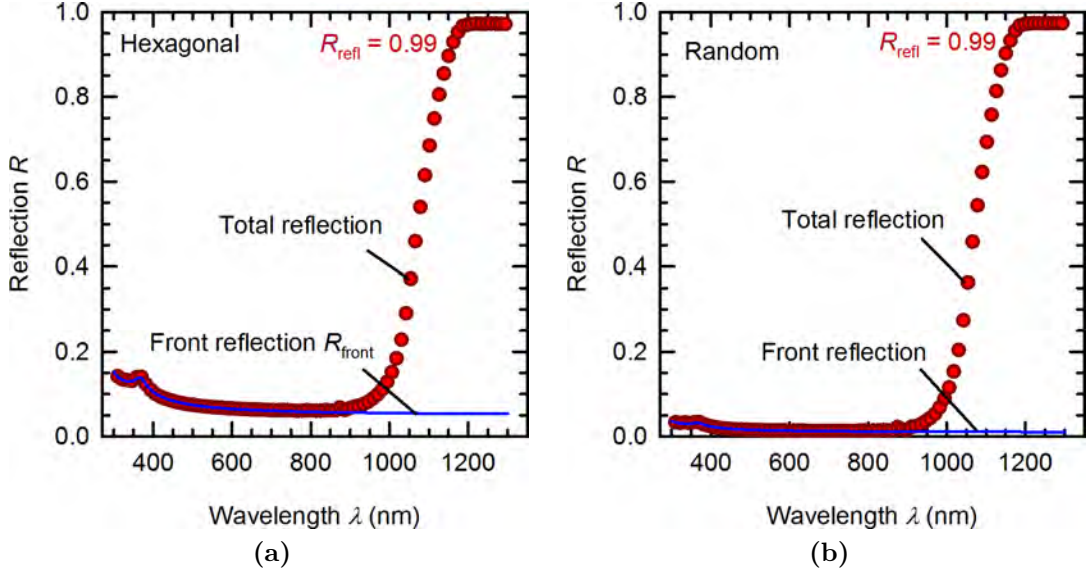


Figure 3.7: Total reflection (red circles) and calculated front reflection (blue line) of the macroporous sample with (a) hexagonally arranged pores and (b) randomly distributed pores with rear reflection $R_{\text{refl}} = 0.99$.

Therefore, the front surface reflection is fitted to the measured total reflection for wavelengths from $\lambda = 300$ nm to 850 nm using Fresnel's reflection at a planar Si surface

$$R_{\text{front}} = a \left(\frac{(n_{\text{Si}} - 1)^2 + k_{\text{Si}}^2}{(n_{\text{Si}} + 1)^2 + k_{\text{Si}}^2} \right)^b. \quad (3.9)$$

Here a is a proportionality constant, n_{Si} is the refractive index of Si, and k_{Si} is the extinction coefficient of Si from Ref. [Gre08]. The exponent b can be interpreted as the average number of interactions of a light ray with the front surface.

The fit then extrapolates the front surface reflection for wavelengths $\lambda > 850$ nm. The blue lines in Fig. 3.7a and 3.7b show the fitted front reflection for both samples. The extrapolated front reflection is almost constant for wavelengths $\lambda > 850$ nm.

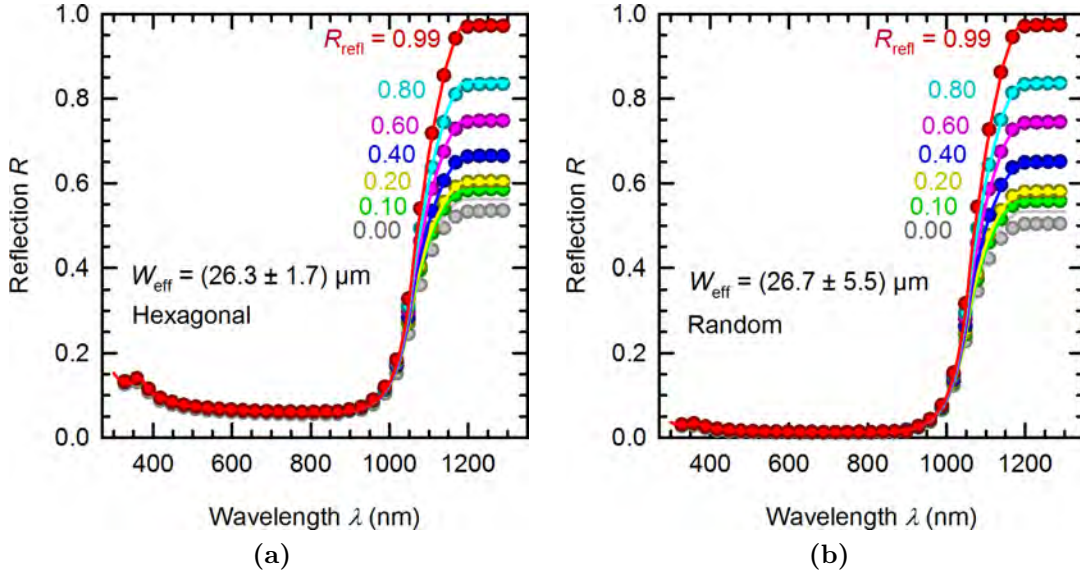
Table 3.1 shows the fitted parameters of Eq. 3.9 for the hexagonal and random pore arrangements.

3.5.3 Reflection of macroporous Si with back reflectors

Figures 3.8a and 3.8b show the reflection of the (34 ± 2) μm -thick sample with hexagonally and the (35 ± 2) μm -thick sample with randomly arranged pores for the seven measurements (dots), respectively.

Table 3.1: Coefficients for fitting the front reflection.

Sample	a	b
Hexagonal	0.3042	1.4821
Random	0.0801	1.6999

**Figure 3.8:** Measured optical reflection R (dots) of (a) a (34 ± 2) μm -thick macroporous silicon layer with hexagonally arranged pores and (b) a (35 ± 2) μm -thick macroporous silicon layer with a random pore distribution for various back reflectors R_{refl} .

For wavelengths $\lambda > 850$ nm the absorption coefficient is $\alpha < 534 \text{ cm}^{-1}$ and, thus, the absorption depth is $\frac{1}{\alpha} > 18 \mu\text{m}$. The effective thickness of the macroporous Si layers is of the same order of magnitude. Thus, an increase of the total reflection is observed for wavelengths $\lambda > 850$ nm.

3.6 Analytical modeling of the reflection

The measured total reflection is modeled analytically using the approach proposed by Brendel and Scholten [Bre99]. Then, the optical absorption in the macroporous Si layer and the back reflector is calculated separately using the verified model.

Figure 3.9 sketches the model schematically. A silicon absorber with the extrapolated front surface reflection $R_{\text{front}} = 1 - T_{\text{front}}$ and the measured rear surface reflection $R_{\text{rear}} = 1 - T_{\text{rear}}$ is placed before a back reflector with reflection R_{refl} . A gap filled with air with

a refractive index of 1 and no absorption is between the silicon absorber and the back reflector. The silicon absorber has a wavelength dependent refractive index n_{Si} and optical absorption coefficient α_{Si} . The model assumes full randomization for the first and all following paths. The only unknown variable is the transmission T_{rear} of the rear side of the macroporous Si layer.

The power flow diagram of Figure 3.9 with the eight intensities $I_{1,2,\dots,8}$ defines eight linear equations. The equations are

$$I_1 = 1 \quad (3.10)$$

$$I_2 = I_1 T_{\text{front}} + I_7 \left(1 - T_{\text{front}} \frac{1}{n_{\text{Si}}^2} \right) \quad (3.11)$$

$$I_3 = I_2 \exp(-\alpha_{\text{eff}} W_{\text{eff}}) \quad (3.12)$$

$$I_4 = I_3 T_{\text{rear}} \frac{1}{n_{\text{Si}}^2} + I_5 (1 - T_{\text{rear}}) \quad (3.13)$$

$$I_5 = I_4 R_{\text{refl}} \quad (3.14)$$

$$I_6 = I_5 T_{\text{rear}} + I_3 \left(1 - T_{\text{rear}} \frac{1}{n_{\text{Si}}^2} \right) \quad (3.15)$$

$$I_7 = I_6 \exp(-\alpha_{\text{eff}} W_{\text{eff}}) \quad (3.16)$$

$$I_8 = I_1 (1 - T_{\text{front}}) + I_7 T_{\text{front}} \frac{1}{n_{\text{Si}}^2}. \quad (3.17)$$

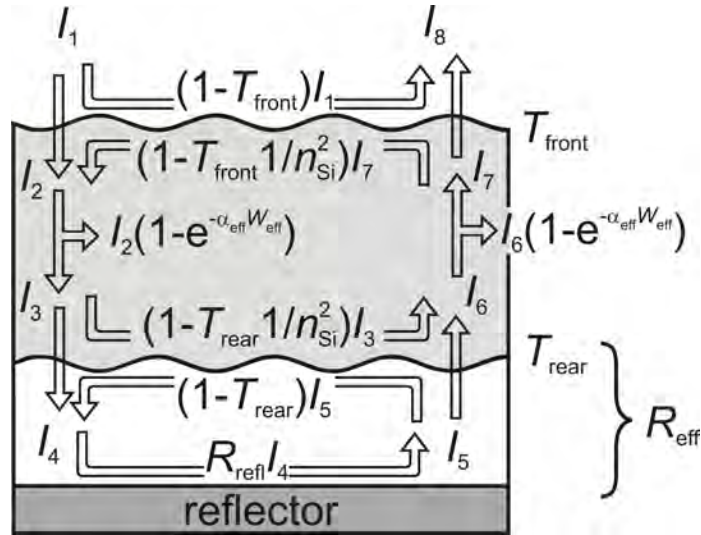


Figure 3.9: Schematic representation of a silicon absorber with a gap filled with air between the absorber and a back reflector. Redrawn from [Bre99].

The absorption coefficient α_{eff} used in some of the equations is the angle-averaged effective absorption coefficient and calculates as

$$T_{\text{eff}} = \frac{\int \exp\left(-\alpha_{\text{Si}} \frac{W_{\text{eff}}}{\cos\theta}\right) d\Omega'}{\int d\Omega'} = \exp(-\alpha_{\text{eff}} W_{\text{eff}}). \quad (3.18)$$

Here

$$\int d\Omega' = \int \cos\theta d\Omega = \int_{\varphi=0}^{2\pi} \int_{\theta=0}^{\pi/2} \sin\theta \cos\theta d\theta d\varphi \quad (3.19)$$

is the integral over the hemisphere weighted by the cosine.

Thus, the effective absorption coefficient is determined by the relation [Luq89]

$$T_{\text{eff}} = \exp(-\alpha_{\text{eff}} W_{\text{eff}}) = 2 \int_0^{\pi/2} \sin\theta \cos\theta \exp(-\alpha_{\text{Si}} W_{\text{eff}} / \cos\theta) d\theta. \quad (3.20)$$

T_{eff} has the meaning of the transmittance of fully randomized light through a planar film with an effective thickness W_{eff} .

The solution of the system of linear equations yields the total reflection

$$R = \frac{I_8}{I_1} = 1 - T_{\text{front}} \frac{n_{\text{Si}}^2 (1 - R_{\text{eff}} T_{\text{eff}}^2)}{n_{\text{Si}}^2 - R_{\text{eff}} (n_{\text{Si}}^2 - T_{\text{front}}) T_{\text{eff}}^2}. \quad (3.21)$$

Here R_{eff} is the effective back reflection, that is defined as

$$R_{\text{eff}} = \frac{I_6}{I_3} = 1 - \frac{1}{n_{\text{Si}}^2} \left(\frac{1}{1 - R_{\text{refl}}} + \frac{1}{T_{\text{rear}}} - 1 \right)^{-1}. \quad (3.22)$$

The absorption in the silicon absorber is expressed as

$$A_{\text{Si}} = (1 - \exp(-\alpha_{\text{eff}} W_{\text{eff}})) (I_2 + I_6) / I_1 \quad (3.23)$$

$$= \frac{(1 - T_{\text{eff}}) (1 + T_{\text{eff}} R_{\text{eff}}) n_{\text{Si}}^2 T_{\text{front}}}{n_{\text{Si}}^2 - R_{\text{eff}} (n_{\text{Si}}^2 - T_{\text{front}}) T_{\text{eff}}^2}. \quad (3.24)$$

Finally, the absorption in the back reflector is calculated as

$$A_{\text{refl}} = I_4 (1 - R_{\text{refl}}) / I_1 \quad (3.25)$$

$$= \frac{-n_{\text{Si}}^2 (R_{\text{eff}} - 1) T_{\text{front}} T_{\text{eff}}}{n_{\text{Si}}^2 - R_{\text{eff}} (n_{\text{Si}}^2 - T_{\text{front}}) T_{\text{eff}}^2}. \quad (3.26)$$

3.7 Fit of experimental data

The calculated total reflection from Eq. 3.21 is fitted simultaneously to the seven measurements with the rear side transmittance T_{rear} in the wavelength range from 300 nm to 1300 nm. This is the only fitted parameter. The fitted rear side transmittance T_{rear} is listed in Table 3.2 for both samples.

The calculated total reflection is shown as solid lines in Figures 3.8a and 3.8b, and is in good agreement with the measurement (dots).

The red symbols in Fig. 3.10a and 3.10b show the measured reflection data for the samples with $R_{\text{reff}} = 0.99$. The extrapolated front reflection is the dashed blue line. The results from the model are shown as solid blue lines. These are the fitted total reflection, the calculated absorption in the silicon, and the calculated absorption in the back reflector.

The uncertainty of the modeled curves stems from the uncertainty of the effective thickness. Optimized fit parameters $T_{\text{rear,up}}$ and $T_{\text{rear,low}}$ are calculated for the upper and lower uncertainty range of the effective thickness, respectively. Table 3.2 shows the rear side transmittance $T_{\text{rear,up}}$ and $T_{\text{rear,low}}$ for both samples.

The uncertainty of the measurement is below 0.005 and therefore not shown in the graph. The maximum deviation from the experiment is 0.01 in case of the hexagonally arranged pores and 0.025 in case of the randomly arranged pores. The deviation in the latter case is higher due to the higher thickness uncertainty of this sample.

The Lambertian absorption curve is calculated for zero front surface reflectance $R_{\text{front}} = 0$ and unity back surface reflection $R_{\text{eff}} = 1$ using equation 3.26. Thus, the absorption for Lambertian light trapping is simplified to [Bre99]

$$A_{\text{Lambert}} = \frac{(1 - T_{\text{eff}})(1 + T_{\text{eff}})n_{\text{Si}}^2}{n_{\text{Si}}^2 - (n_{\text{Si}}^2 - 1)T_{\text{eff}}^2}. \quad (3.27)$$

The solid red lines in Fig. 3.10a and 3.10b show the calculated absorption of a Lambertian light trapping scheme for a sample with a thickness of $(26.3 \pm 1.7) \mu\text{m}$ and $(26.7 \pm 5.5) \mu\text{m}$, respectively. The difference between the Lambertian absorption curve and the absorption in the macroporous Si absorber is mainly due to the reflection loss at the front side of the macroporous Si layer.

Table 3.2: Rear side transmittance T_{rear} for thickness W_{eff} , and $T_{\text{rear,up}}$ and $T_{\text{rear,low}}$ for the upper and lower uncertainty of the effective thickness, respectively.

Sample	W_{eff}	T_{rear}	$T_{\text{rear,up}}$	$T_{\text{rear,low}}$
Hexagonal	$(26.3 \pm 1.7) \mu\text{m}$	0.7684	0.7630	0.7897
Random	$(26.7 \pm 5.5) \mu\text{m}$	0.8225	0.8208	0.8449

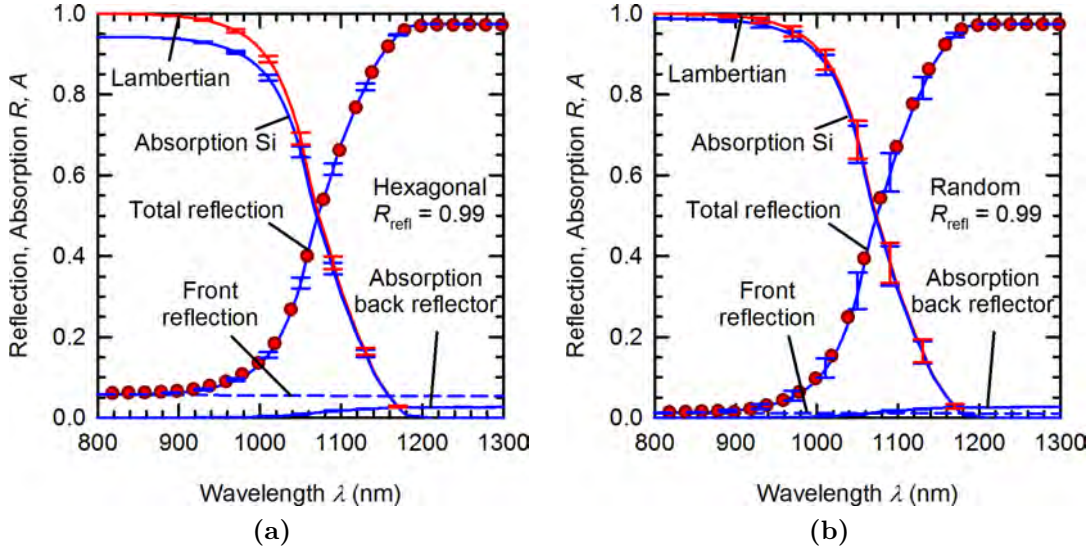


Figure 3.10: Optical reflection (red dots) measured with a back reflector with $R_{\text{refl}} = 0.99$, calculated front reflection (dashed blue line), calculated reflection and absorption (solid blue lines), and calculated Lambertian absorption (solid red line) for (a) hexagonally arranged pores and (b) randomly distributed pores.

3.8 Photogeneration current density

The photogeneration current density J_{SC}^* is calculated by integrating the product of photon flux Φ of AM1.5g spectrum from Ref. [Gue95, Gue01] at 0.1 W cm^{-2} , calculated absorption A_{Si} of the Si absorber, and elementary charge q from 300 nm to 1300 nm:

$$J_{\text{SC}}^* = q \int_{300 \text{ nm}}^{1300 \text{ nm}} \Phi A_{\text{Si}} d\lambda. \quad (3.28)$$

In case of the randomly arranged pores, the photogeneration current density is $(40.82 \pm 0.36) \text{ mA cm}^{-2}$ for the best experimental back reflector with $R_{\text{refl}} = 0.99$. The photogeneration current density for the hexagonally arranged pores is $(38.71 \pm 0.10) \text{ mA cm}^{-2}$.

Table 3.3 shows the calculated photogeneration current densities of the two macroporous Si samples for the seven measurements. As expected from the lower front surface reflection of the sample with randomly distributed pores, the photogeneration current density is higher compared to the sample with hexagonally arranged pores. The current loss of the measurement without back reflector compared with the measurement with the best experimental back reflector $R_{\text{refl}} = 0.99$ is only about 1 mA cm^{-2} . Thus, the macroporous Si absorber performs well also without a back reflector.

Table 3.3: Photogeneration current densities for the measurements with six back reflectors and without back reflector.

Back reflection R_{reff}	Hexagonal $W_{\text{eff}} = (26.3 \pm 1.7) \mu\text{m}$ $J_{\text{SC}}^* \text{ (mA cm}^{-2}\text{)}$	Random $W_{\text{eff}} = (26.7 \pm 5.5) \mu\text{m}$ $J_{\text{SC}}^* \text{ (mA cm}^{-2}\text{)}$
0	37.77 ± 0.14	39.82 ± 0.45
0.1	37.84 ± 0.13	39.89 ± 0.45
0.2	37.90 ± 0.13	39.96 ± 0.44
0.4	38.06 ± 0.12	40.14 ± 0.42
0.6	38.27 ± 0.11	40.37 ± 0.40
0.8	38.46 ± 0.10	40.57 ± 0.38
0.99	38.71 ± 0.10	40.82 ± 0.36

The Lambertian light trapping scheme yields the Lambertian limit of the photogeneration current density. The photogeneration current density of a $W_{\text{eff}} = (26.3 \pm 1.7) \mu\text{m}$ -thick absorber is $(41.40 \pm 0.10) \text{ mA cm}^{-2}$ (hexagonal case). In case of the randomly arranged pores, the photogeneration current is $(41.43 \pm 0.37) \text{ mA cm}^{-2}$ for an effective thickness of $W_{\text{eff}} = (26.7 \pm 5.5) \mu\text{m}$.

The photogeneration current density of the hexagonal macroporous absorber with the best experimental back reflector achieves a fraction 0.935 ± 0.003 of the Lambertian limit. The random structure performs better and achieves a fraction 0.985 ± 0.012 of the Lambertian limit. This difference is mainly due to the lower front reflection compared with the hexagonal structure.

3.9 Current losses

When compared to ideal Lambertian light trapping, the experiment shows current losses due to reflection at the non-ideal front side and parasitic absorption in the back reflector.

Table 3.4 and 3.5 compare the photogeneration current densities of both experimental absorbers for the back reflector $R_{\text{reff}} = 0.99$ with an absorber with ideal front side and the Lambertian absorber. The photogeneration current density of the hexagonal macroporous Si layer achieves a fraction 0.935 ± 0.003 of the Lambertian limit. The random structure achieves a fraction 0.985 ± 0.012 of the Lambertian limit. However, the major part of the losses occurs at the front side of the samples due to a non-ideal front surface reflection. No anti-reflection coating was applied to the samples. Thus, the front surface reflection, particularly in the case of the hexagonally arranged pores, can be enhanced by applying an optimized anti-reflection coating.

Table 3.4: Photogeneration current densities of experimental and ideal light trapping for the hexagonal sample with $W_{\text{eff}} = (26.3 \pm 1.7) \mu\text{m}$.

Category	Hexagonal	Ideal front side	Ideal Lambertian
Front reflection R_{front}	from exp.	0	0
Rear absorber R_{refl}	from exp.	from exp.	1
Photogen. in Si absorber (mA cm^{-2})	38.71 ± 0.10	41.36 ± 0.11	41.40 ± 0.10
Fraction of ideal Lambertian	0.935 ± 0.003	0.999 ± 0.004	1

Table 3.5: Photogeneration current densities of experimental and ideal light trapping for the random sample with $W_{\text{eff}} = (26.7 \pm 5.5) \mu\text{m}$.

Category	Random	Ideal front side	Ideal Lambertian
Front reflection R_{front}	from exp.	0	0
Rear absorber R_{refl}	from exp.	from exp.	1
Photogen. in Si absorber (mA cm^{-2})	40.82 ± 0.36	41.38 ± 0.37	41.43 ± 0.37
Fraction of ideal Lambertian	0.985 ± 0.012	0.999 ± 0.013	1

3.10 Conclusion

In this chapter experiments and simulations tools were designed and conducted to quantify the degree of Lambertian light trapping for macroporous silicon. The measured hemispherical reflection of macroporous Si with various back reflectors is measured and analytically modeled. The modeled reflection agrees well with the measured spectra.

The optical absorption of macroporous Si is then calculated using the verified model. The optical absorption spectrum is well described by Lambertian light trapping. In case of the randomly arranged pores, the photogeneration current density is $(40.82 \pm 0.36) \text{mA cm}^{-2}$ for the best experimental back reflector.

The macroporous silicon layer with randomly distributed pores show a light trapping performance that has a fraction 0.985 ± 0.012 of Lambertian light trapping schemes.

4 | Efficiency potential

The optical quality of macroporous Si as absorber material for thin crystalline solar cells was quantified in Chapter 3. In order to experimentally determine the efficiency potential of macroporous Si, measuring of implied J - V curves is beneficial.

A common method measures the open-circuit voltage V_{OC} as a function of the light intensity [Wol63]. This so called suns- V_{OC} technique is similar to the J_{SC} - V_{OC} measurement, except that the short-circuit current density J_{SC} is substituted by the incident light intensity. However, this method still requires electrical contacts for measuring the open-circuit voltage and, thus, cannot be applied to fully passivated samples without contacts.

Trupke et al. [Tru05] followed a different approach. They measure the photoluminescence (PL) signal to determine the implied open-circuit voltage V_{OC} . The method is based on the fact that both, the PL signal and the voltage of a solar cell are linked to the separation of the quasi Fermi energies. It therefore allows for contactless determination of the implied voltage as a function of the incident illumination intensity except for a calibration constant. The incident photon flux is determined using a calibrated solar cell. However, calibration of the PL signal is performed using an electrically contacted method in Trupke's approach.

In this work, the contactless transient microwave-detected photoconductance decay method is used to calibrate the PL signal. This allows measuring the implied J - V characteristics and the efficiency potential of new absorber materials without electrical contacts that cannot be measured using well-established methods. In this chapter, this new method is applied to passivated macroporous Si layers.

4.1 Sample preparation

The macroporous Si layers that have been optically characterized in Chapter 3 are attached to a silicon frame to ease handling of the samples. This bonding process is described later in Section 5.1. The resulting samples are 25 mm \times 25 mm-sized with a "usable" free-standing 20 mm \times 20 mm-sized area.

First, the samples are RCA-cleaned [Ker70]. Then, 170 cycles of plasma-assisted atomic layer deposition (PA-ALD) of Al_2O_3 generate a 20 nm-thick passivating layer on the front side of the samples and in the pores. One ALD cycle is equivalent to 0.12 nm aluminum oxide [vH07]. After flipping the samples, further 170 cycles of PA-ALD create a passivating Al_2O_3 -layer on the rear side of the samples. Since the pores see both deposition processes, the resulting Al_2O_3 -layer thickness in the pores is 40 nm.

Finally, the samples are annealed in a furnace in nitrogen atmosphere at 425 °C for 15 min to activate the Al₂O₃ passivation [Hoe06, Hoe07].

4.2 Measurement setup

Measuring of effective carrier lifetimes for calibrating the PL signal and the photoluminescence signal itself is performed sequentially in the photoluminescence measurement setup that is described in more detail in Ref. [Hin11].

4.2.1 Effective carrier lifetime

First, the effective carrier lifetime is measured by means of light-biased microwave-detected photoconductance decay (MW-PCD, WT-2000 system from Semilab) technique. In order to obtain identical measurement conditions, the MW-PCD measuring head is embedded in the PL setup as shown in Fig. 4.1.

The MW-PCD technique measures the reflection of microwaves due to free charge carriers in the Si wafer. Subsequent to a pulsed excitation, the decay of the average excess carrier density is measured. The reflectivity of microwaves is a non-linear function of the free charge carrier density [Kun86, Sch95]. This restricts the technique to using small excitation intensities. For this reason, bias illumination with the laser of the PL setup is used.

The bias illumination source is a 30 W laser diode with a central wavelength of $\lambda = 808$ nm. In order to illuminate the entire sample area, the laser beam is widened and homogenized by an array of microlenses. The samples are illuminated from the front side. For varying the bias illumination intensity, the diode current and distance of the microlens-array to the sample are adjusted. Furthermore, optical gray filters are used to reduce the illumination intensity.

The stationary bias laser illumination is superposed by low-intensity laser pulses. The pulsed excitation source is a laser diode that emits light at a wavelength of $\lambda = 904$ nm and excites the sample from the bottom. The pulse duration is ≈ 200 ns at a pulse rate of 1.6 kHz. The optical absorption length of the short pulse laser is approximately 30 μ m in crystalline silicon and, thus, comparable to the layer thickness.

4.2.2 Photoluminescence signal

Second, the MW-PCD measuring head is removed from the PL setup and a heated sample table with a calibrated reference cell is integrated in the setup. The distance between the sample and the beam optics is identical to the lifetime measurements.

The photoluminescence signal I_{PL} of the sample on the table is measured for various illumination intensities using a charge-coupled device (CCD, C9100-13 from Hamamatsu) camera. The camera is peltier-cooled to -65 °C to increase the signal-to-noise ratio. Three images for each bias illumination are recorded sequentially and averaged after subtracting

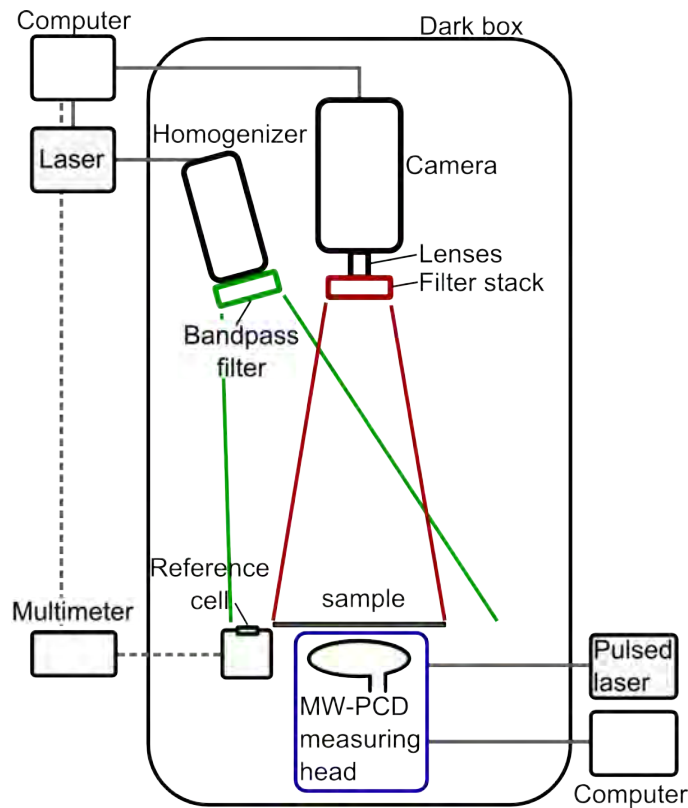


Figure 4.1: Illustration of the MW-PCD setup with laser-based bias illumination. After Ref. [Her13].

background images that are recorded without bias illumination. Thus, each PL image requires six measurements.

In order to further increase the signal-to-noise ratio, the integration time of the camera is adjusted from few seconds to several minutes for decreasing bias illumination.

The calibrated Si solar cell is used to measure the photon flux Φ of the bias illumination. The short-circuit current density of the solar cell is calibrated to the measured irradiance from a detector with known quantum efficiency at $\lambda = 808$ nm.

In contrast to the MW-PCD measurement head, the sample is heated (but not actively cooled) to a temperature of $T_0 = (304 \pm 1)$ K as measured by means of four-wire sensing of a resistive temperature device (PT-1000).

4.3 Measurement results

4.3.1 Effective carrier lifetime

The effective carrier lifetime is measured for various photon fluxes Φ of the bias illumination as measured using the calibrated Si solar cell in the PL setup.

Figure 4.2a and 4.2b show typical photoconductance decay data (red dots) measured by means of the MW-PCD technique for a bias illumination of $\Phi = 6.9 \times 10^{16} \text{ cm}^{-2} \text{ s}^{-1}$ of the sample with hexagonally arranged pores and randomly distributed pores, respectively. The solid lines show a fit for the differentially measured carrier lifetime.

Transient measurements in the presence of a bias light and with weak pulsed light yield a differential effective carrier lifetime $\tau_{\text{eff,d}} = \partial\tau_{\text{eff}}/\partial\Delta p$ instead of the actual steady-state carrier lifetime [Bre95]. The measured differential effective lifetime $\tau_{\text{eff,d}}$ depends on the injection level and, thus, the actual carrier lifetime has to be calculated from the differential carrier lifetime [Sch97].

Figure 4.3a and 4.3b show the measured differential effective carrier lifetime $\tau_{\text{eff,d}}$ (red dots) of the sample with hexagonally arranged pores and randomly arranged pores as a function of the incident photon flux Φ , respectively. The relative measurement error is 10% of the measured carrier lifetime.

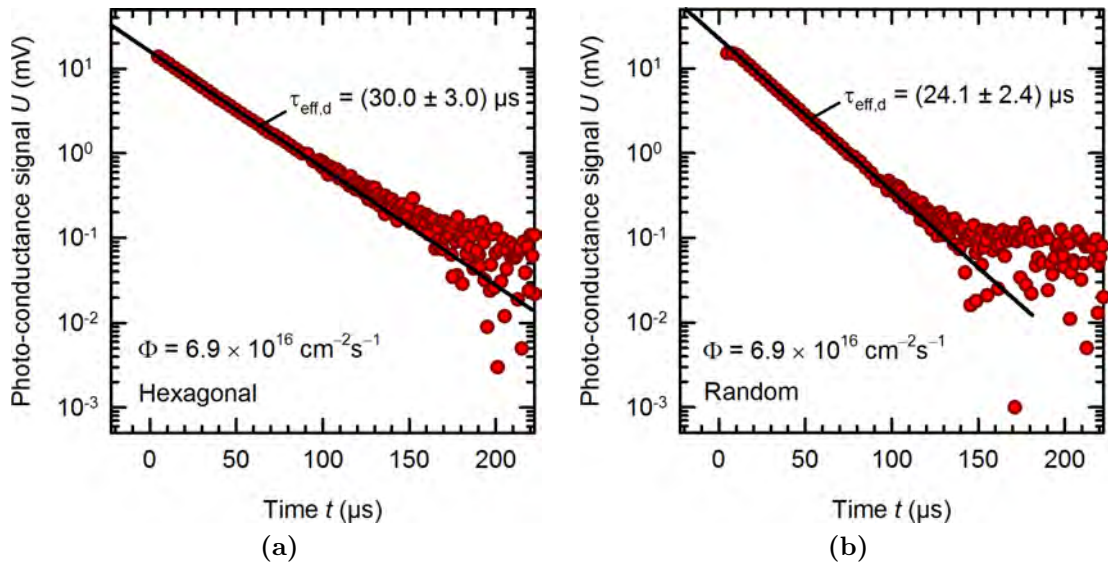


Figure 4.2: Photoconductance decay data (red dots) as measured by the MW-PCD technique of the sample (a) with hexagonally arranged pores and (b) randomly distributed pores. The solid lines show a fit for the extracted carrier lifetime.

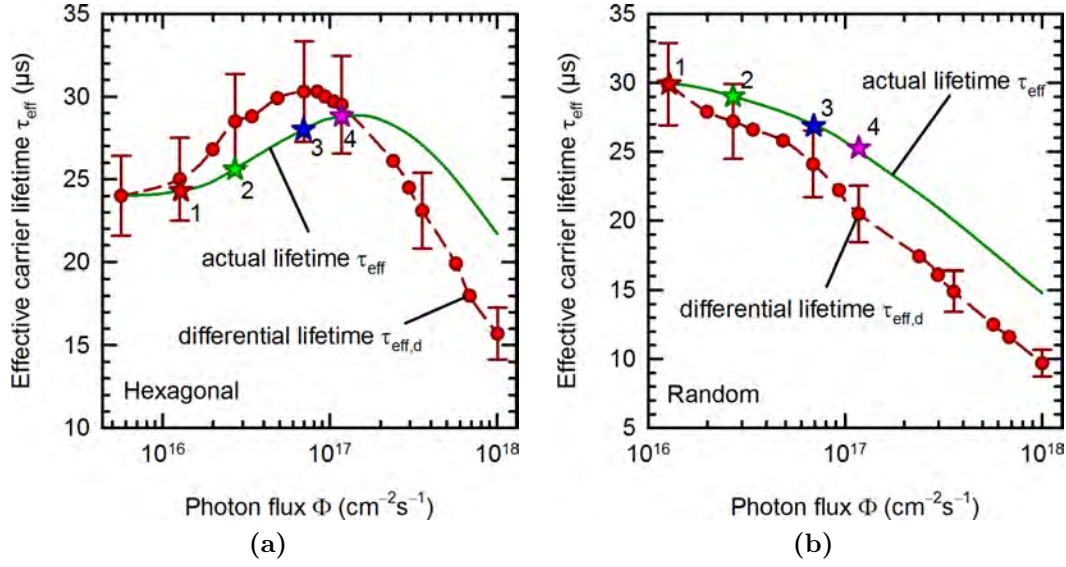


Figure 4.3: Differentially measured effective carrier lifetime $\tau_{\text{eff,d}}$ (red dots) versus the incident photon flux Φ of the sample (a) with hexagonally arranged pores and (b) randomly distributed pores. The dashed red lines are spline interpolations of the differentially measured effective carrier lifetime. The solid green lines show the actual carrier lifetime τ_{eff} as calculated from the dashed lines using the approximation of Schuurmans et al. [Sch97]. The colored stars mark the carrier lifetimes that are used for calibrating the photoluminescence-based method.

If the decay of excess carriers is described by a monoexponential decay, the differential effective lifetime $\tau_{\text{eff,d}}$ is defined as

$$\frac{1}{\tau_{\text{eff,d}}} = \frac{\partial R(\Delta p)}{\partial \Delta p}, \quad (4.1)$$

where R is the net effective recombination rate.

The net effective generation rate G and the recombination rate R are balanced under steady-state conditions, thus

$$G = \frac{\Phi A}{W_{\text{eff}}} = \frac{\Delta p}{\tau_{\text{eff}}} = R. \quad (4.2)$$

The generation rate G in Eq. 4.2 is proportional to the photon flux Φ of the bias light. Here, the optical absorption A of the sample at the wavelength $\lambda = 808$ nm of the bias illumination and the effective sample thickness W_{eff} is used.

By replacing R in Eq. 4.1 by G , the differential effective lifetime $\tau_{\text{eff,d}}$ is expressed as

$$\tau_{\text{eff,d}} = \frac{\partial \Delta p}{\partial G} = \frac{W_{\text{eff}}}{A} \frac{\partial \Delta p}{\partial \Phi}, \quad (4.3)$$

$$\partial \Delta p = \frac{A}{W_{\text{eff}}} \tau_{\text{eff,d}} \partial \Phi. \quad (4.4)$$

Integrating Eq. 4.4 over the incident photon flux Φ yields the excess carrier density Δp . The actual effective lifetime τ_{eff} is then given by the relation [Sch97]

$$\tau_{\text{eff}}(\Phi) = \frac{\Delta p}{G} = \frac{W_{\text{eff}}}{A} \frac{\Delta p}{\Phi} = \frac{1}{\Phi} \int_0^{\Phi} \tau_{\text{eff,d}}(\varphi) \, d\varphi. \quad (4.5)$$

Experimentally $\tau_{\text{eff,d}}$ cannot be measured for low photon fluxes Φ . Hence, the lower integration limit in Eq. 4.5 is replaced by the lowest experimentally accessible photon flux Φ_{min} . Then, the calculation of τ_{eff} in Eq. 4.5 can be approximated as

$$\tau_{\text{eff}}(\Phi) = \frac{\Delta p}{G} = \tau_{\text{eff,d}}(\Phi_{\text{min}}) \frac{\Phi_{\text{min}}}{\Phi} + \frac{1}{\Phi} \int_{\Phi_{\text{min}}}^{\Phi} \tau_{\text{eff,d}}(\varphi) \, d\varphi. \quad (4.6)$$

A spline curve (dashed lines) interpolates the differentially measured effective carrier lifetime in Fig. 4.3. The actual effective carrier lifetime (solid green lines) is determined from the spline interpolation using the approximation of Schuurmans et al. [Sch97]. The lowest photon flux $\Phi_{\text{min}} = 1.3 \times 10^{16} \text{ cm}^{-2} \text{ s}^{-1}$ for the random sample and $\Phi_{\text{min}} = 5.6 \times 10^{15} \text{ cm}^{-2} \text{ s}^{-1}$ for the hexagonal sample is used in Eq. 4.6.

The excess carrier density Δp can now be calculated from the actual effective carrier lifetime using that $G = R$ under steady-state conditions:

$$\Delta p = \frac{\Phi A \tau_{\text{eff}}}{W_{\text{eff}}}. \quad (4.7)$$

Figure 4.4a and 4.4b show the actual effective carrier lifetime τ_{eff} (solid green lines) in dependence on the excess carrier density Δp of the samples with randomly distributed pores and hexagonally arranged pores, respectively. The four stars mark the effective carrier lifetimes that will be used in Section 4.4 for calibrating the photoluminescence-based implied J - V method.

4.3.2 Photoluminescence signal

Figure 4.5a and 4.5b show averaged PL images of three consecutively recorded images of the sample with hexagonally arranged pores and randomly arranged pores, respectively. For the bias illumination of $\Phi = 6.8 \times 10^{17} \text{ cm}^{-2} \text{ s}^{-1}$ a camera integration time of 0.9 s is

used. In case of the lower illumination intensity of $\Phi = 6.9 \times 10^{16} \text{ cm}^{-2} \text{ s}^{-1}$ the camera integration time is 9.6s. The dashed box marks the area for averaging the PL signal I_{PL} . The PL signal depends on the incident illumination intensity.

The inhomogeneities of the PL images may result from inhomogeneities of the etching procedure and localized cracks that introduce centers of recombination. In case of the sample with randomly arranged pores the PL signal decreases from left to right in the image. Only the region with high signal is considered for determining the efficiency potential.

4.3.3 Implied voltage

The photoluminescence signal I_{PL} is proportional to the separation of the quasi-Fermi levels and therefore to the implied voltage V of a corresponding solar cell

$$I_{\text{PL}} \propto R_{\text{rad}} = Bnp. \quad (4.8)$$

Here R_{rad} is the rate of radiative recombination that is proportional to the radiative recombination coefficient B and the product of electron and hole density np .

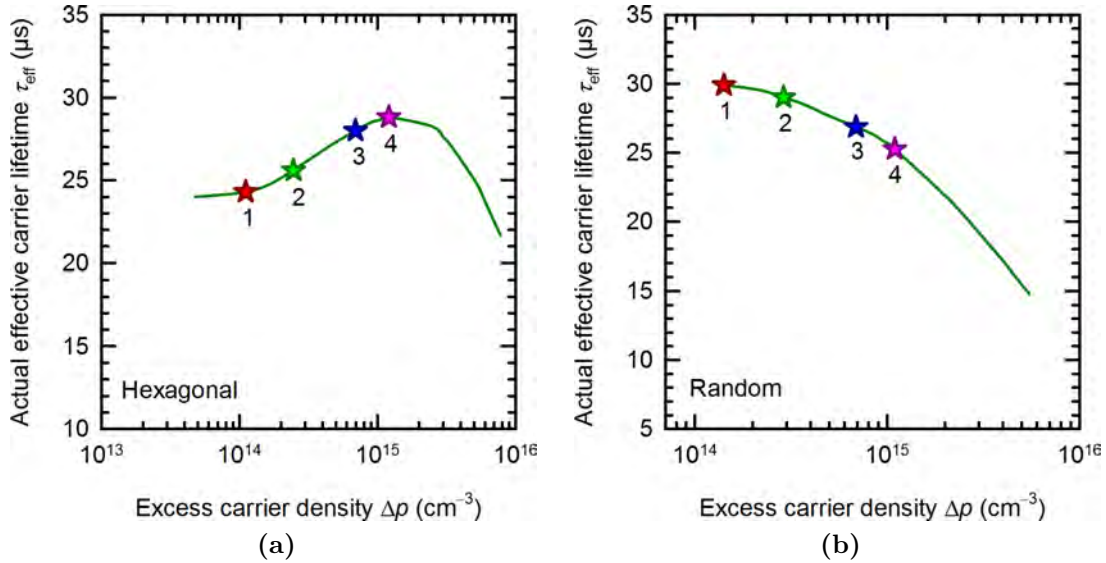


Figure 4.4: Actual effective carrier lifetime τ_{eff} (solid green lines) versus the excess carrier density Δp of the sample (a) with hexagonally arranged pores and (b) randomly distributed pores. The carrier lifetimes marked by the four stars are used for calibrating the photoluminescence-based method.

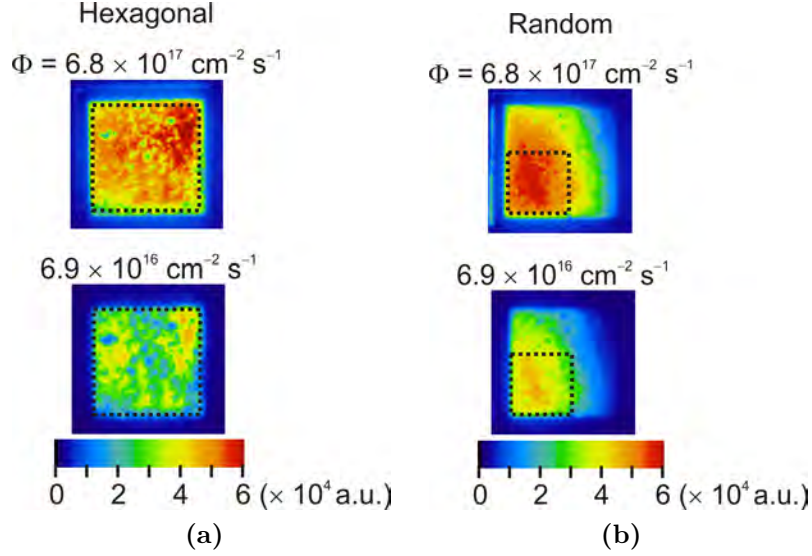


Figure 4.5: Averaged PL images for two bias illuminations of the sample with (a) hexagonally arranged pores and (b) randomly arranged pores. The dashed box marks the area for averaging the PL signal.

The radiative recombination coefficient $B = B(T, \Delta p, N_D)$ depends on the substrate doping N_D , excess carrier density Δp , and the temperature T . These dependencies are considered by using the parametrization of B from Altermatt et al. [Alt05].

Under illumination the Law of Mass Action yields

$$np = n_{i,\text{eff}}^2 \exp\left(\frac{qV}{kT}\right), \quad (4.9)$$

where qV is the separation of the quasi Fermi energies.

The effective intrinsic carrier concentration is obtained via the relation

$$n_{i,\text{eff}} = n_i(T) \exp\left(\frac{q\Delta E_g}{2kT}\right), \quad (4.10)$$

where $n_i(T)$ the temperature dependent intrinsic carrier concentration, q the elementary charge, ΔE_g the band gap narrowing, k is the Boltzmann constant, and T is the temperature. The band gap narrowing ΔE_g is calculated using the parametrization of Schenk [Sch98].

The temperature dependent intrinsic carrier concentration $n_i(T)$ is calculated by the empiric relation [Mis93]

$$\frac{n_i(T)}{\text{cm}^{-3}} = 5.29 \cdot 10^{19} \left(\frac{T}{300 \text{ K}}\right)^{2.54} \exp\left(\frac{-6726 \text{ K}}{T}\right). \quad (4.11)$$

In the following, the subscripts n and c denote the particular parameters for the PL measurement for the varied photon flux Φ_n and for photon flux Φ_c at a specific calibration point, respectively.

The photoluminescence signals $I_{\text{PL},n}$ and $I_{\text{PL},c}$ then are

$$I_{\text{PL},n} = fAB_n n_{i,n}^2 \exp\left(\frac{qV_n}{kT_n}\right), \quad (4.12)$$

$$I_{\text{PL},c} = fAB_c n_{i,c}^2 \exp\left(\frac{qV_c}{kT_c}\right). \quad (4.13)$$

The equations use the parametrized temperature, dopant, and excess carrier dependent radiative recombination coefficient $B_n = B(T_n, \Delta p_n, N_D)$ and $B_c = B(T_c, \Delta p_c, N_D)$ from Ref. [Alt05] and the effective intrinsic carrier concentration $n_{i,n} = n_{i,n}(T_n, \Delta p_n, N_D)$ and $n_{i,c} = n_{i,c}(T_c, \Delta p_c, N_D)$ from Eq. 4.10 for the particular measurement point with subscripts n and c, respectively. The proportionality factor f and absorption A is assumed to be constant.

The implied voltage V_n for the photon flux Φ_n follows from taking the logarithm of the quotient $I_{\text{PL},n}/I_{\text{PL},c}$:

$$V_n = \frac{kT_n}{q} \ln\left(\frac{I_{\text{PL},n}}{I_{\text{PL},c}}\right) - \underbrace{\frac{kT_n}{q} \left(\ln\left(\frac{B_n}{B_c}\right) + \ln\left(\frac{n_{i,n}^2}{n_{i,c}^2}\right) \right)}_{=C(T, N_D, \Delta p)} + \frac{T_n}{T_c} V_c. \quad (4.14)$$

Here, the calibration voltage V_c has to be determined separately.

Figure 4.6a and 4.6b show the incident photon flux Φ as a function of the implied voltage V calculated from the relative PL signal using Eq. 4.14 for $C = 0$. The camera integration time for the lowest bias illumination of $\Phi = 1.5 \times 10^{15} \text{ cm}^{-2} \text{ s}^{-1}$ is 750 s for each of the three images and three background images. Thus, the total time for measuring the PL signal for this bias illumination intensity is 75 min.

Section 4.4 determines the calibration voltage V_c from the effective carrier lifetime measurements.

4.3.4 Systematic temperature error

The sample table heats the macroporous Si layer to $T_0 = 304 \text{ K}$ during photoluminescence measurement. Since the sample table is not actively cooled, the sample heats up due to the laser illumination.

The derivation of the implied voltage in the following subsection therefore accounts for the temperature T_n of each measurement point. A linear dependence of the sample temperature to the photon flux Φ_n is assumed, thus

$$T_n = T_0 + \frac{\Phi_n}{\Phi_{\text{max}}} \Delta T. \quad (4.15)$$

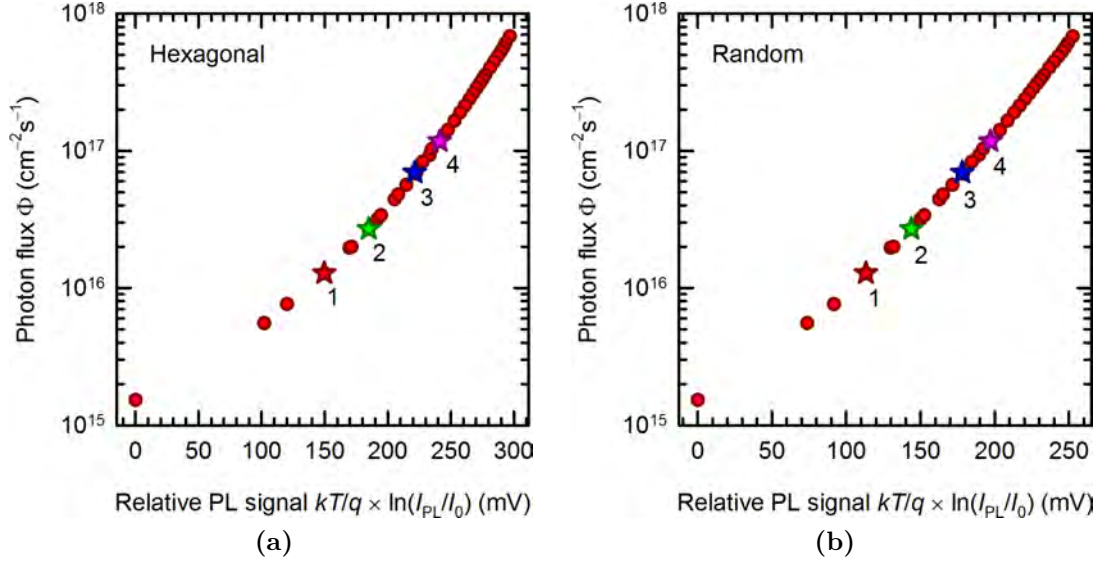


Figure 4.6: Incident photon flux Φ versus the implied voltage V as calculated from the relative PL signal using Eq. 4.14 for the sample with (a) hexagonally arranged pores and (b) randomly arranged pores. The data points marked by the four stars are used to calibrate voltage-axis.

T_0 is the temperature without illumination and ΔT is the temperature increase for the photon flux Φ_{max} . When measuring the carrier lifetime, no heating table is used. Since the temperature was not measured in this case, the same temperature change with illumination is assumed.

Four-wire sensing of a resistive temperature device (Pt1000) measures the sample temperature T_0 on the heated table without illumination. In this case, the sample temperature is $T_0 = (304 \pm 1)$ K.

In order to measure the temperature increase under illumination conditions, a thermographic camera measures the thermographic image without illumination and under illumination with $\Phi_{\text{max}} = 2.7 \times 10^{17} \text{ cm}^{-2} \text{ s}^{-1}$. The camera signal is calibrated by measuring the sample temperature with the Pt1000 sensor on a hot plate for temperatures ranging from 297 K to 324 K. The camera signal increases linearly with the measured temperature.

Figure 4.7 shows the thermographic image for the hexagonal and random sample with and without illumination. A temperature increase of $\Delta T = 5$ K is observed when illuminating with $\Phi_{\text{max}} = 2.7 \times 10^{17} \text{ cm}^{-2} \text{ s}^{-1}$.

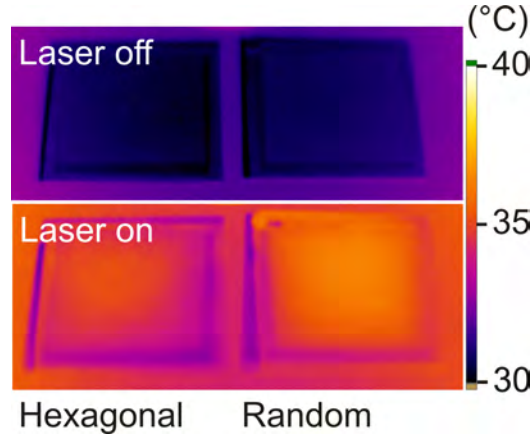


Figure 4.7: Thermographic image of the macroporous Si samples without illumination and under laser illumination at $\Phi_{\max} = 2.7 \times 10^{17} \text{ cm}^{-2} \text{ s}^{-1}$ approximately equivalent to illumination of one sun.

4.4 Voltage calibration

Calibration of the measurement is performed at the four points marked with stars in Figs. 4.6a and 4.6b. The measurement of the actual effective carrier lifetimes τ_{eff} for these four illumination intensities from Section 4.3.1 is used to determine the calibration voltage V_c in Eq. 4.14.

The product of the carrier densities np is

$$np = \Delta p (\Delta p + N_D) = n_{i,c}^2 \exp\left(\frac{qV_c}{kT_c}\right) \quad (4.16)$$

for the calibration point c and, thus

$$\Delta p = -\frac{1}{2}N_D + \frac{1}{2}\sqrt{N_D^2 + 4n_{i,c}^2 \exp\left(\frac{qV_c}{kT_c}\right)}. \quad (4.17)$$

Generation G equals recombination R , hence the expression from Eq. 4.2 can be used to substitute Δp by

$$\Delta p = \frac{\Phi A \tau_{\text{eff}}}{W_{\text{eff}}}. \quad (4.18)$$

Here $A = 0.939$ and $A = 0.985$ is the optical absorption at a wavelength of $\lambda = 808 \text{ nm}$ of the sample with hexagonally arranged pores and randomly arranged pores from Chapter 3, respectively. The effective sample thickness $W_{\text{eff}} = (26.3 \pm 1.7) \mu\text{m}$ for the sample with hexagonally arranged pores. In case of the randomly arranged pores, the effective thickness

is $(26.7 \pm 5.5) \mu\text{m}$. The photon flux Φ and effective carrier lifetime τ_{eff} is shown in Table 4.1 for the four calibration points.

The open-circuit voltage V_c for calibrating the PL signal evaluated from the measured effective carrier lifetime τ_{eff} then is

$$V_c = \frac{kT_c}{q} \ln \left(\frac{\Phi_c A \tau_{\text{eff}} (\Phi_c A \tau_{\text{eff}} + N_D W_{\text{eff}})}{W_{\text{eff}}^2 n_i (T_c)^2} \right). \quad (4.19)$$

Table 4.1 shows the effective carrier lifetime τ_{eff} , photon flux Φ_c of the bias illumination, and the calibration constant V_c for the four calibration points of both samples.

The implied J - V characteristic can also be directly calculated from the effective carrier lifetime using Eq. 4.19. However, carrier lifetimes could not be measured at low bias light intensities. Thus, measuring at low carrier injection densities requires a more sensitive, for instance a photoluminescence-based, method.

Table 4.1: Effective carrier lifetime τ_{eff} , photon flux Φ_c of the bias illumination, and calibration constant V_c for the four calibration points.

Sample	Calib. point	τ_{eff} (μs)	Φ_c ($\text{cm}^{-2} \text{s}^{-1}$)	V_c (mV)
Hexagonal	1	24.3	1.3×10^{16}	558.3
Hexagonal	2	25.6	2.7×10^{16}	579.7
Hexagonal	3	28.0	6.9×10^{16}	608.2
Hexagonal	4	28.8	1.2×10^{17}	624.1
Random	1	29.9	1.3×10^{16}	564.9
Random	2	29.0	2.7×10^{16}	584.2
Random	3	26.9	6.9×10^{16}	607.9
Random	4	25.3	1.2×10^{17}	620.8

4.5 Calibration results

4.5.1 Implied J - V curves

The implied current density J is calculated from the measured photon flux Φ_n and the optical absorption A of the sample at a wavelength of $\lambda = 808$ nm. The implied current density J is shifted by the photogeneration current density J_{SC}^* from the optical absorption measurement in Chapter 3. Thus,

$$J = J_{\text{SC}}^* - q\Phi_n A. \quad (4.20)$$

Table 4.2 lists the required parameters from the optical measurement.

The implied voltage V from Eq. 4.14 is

$$V_n = \frac{kT_n}{q} \ln \left(\frac{I_{\text{PL},n}}{I_{\text{PL},c}} \right) - \frac{kT_n}{q} \left(\ln \left(\frac{B_n}{B_c} \right) + \ln \left(\frac{n_{i,n}^2}{n_{i,c}^2} \right) \right) + \frac{T_n}{T_c} V_c. \quad (4.21)$$

Figure 4.8a and 4.8b show the implied J - V curves for the four calibration points of the samples with randomly distributed pores and hexagonally arranged pores, respectively.

Table 4.3 lists the extracted parameters determined from the implied J - V curves for the four calibration points of both samples. The average efficiency potential of the four calibrations is (21.5 ± 0.4) % for samples with randomly arranged pores and (20.2 ± 0.4) % for samples with hexagonally arranged pores.

The discrepancy between both samples is mainly due to the lower optical absorption of the macroporous Si layers with hexagonally arranged pores. However, the optical absorption of the hexagonal sample could easily be increased by applying an anti-reflection coating, as described in Chapter 3.

However, when evaluating the implied J - V curves, the experimentally measured input data is afflicted with measuring errors. Subsection 4.6 therefore addresses the possible impact of erroneous input parameters.

4.5.2 Ideality Factor

The slope of the natural log of the current J as a function of the voltage V is q/nkT , where n is the local ideality factor.

Table 4.2: Absorption A at a wavelength of $\lambda = 808$ nm and photogeneration current density J_{SC}^* from Chapter 3 for both samples.

Parameter	Randomly arranged pores	Hexagonally arranged pores
A at 808 nm	0.985	0.939
J_{SC}^*	(40.82 ± 0.36) mA cm ⁻²	(38.71 ± 0.10) mA cm ⁻²

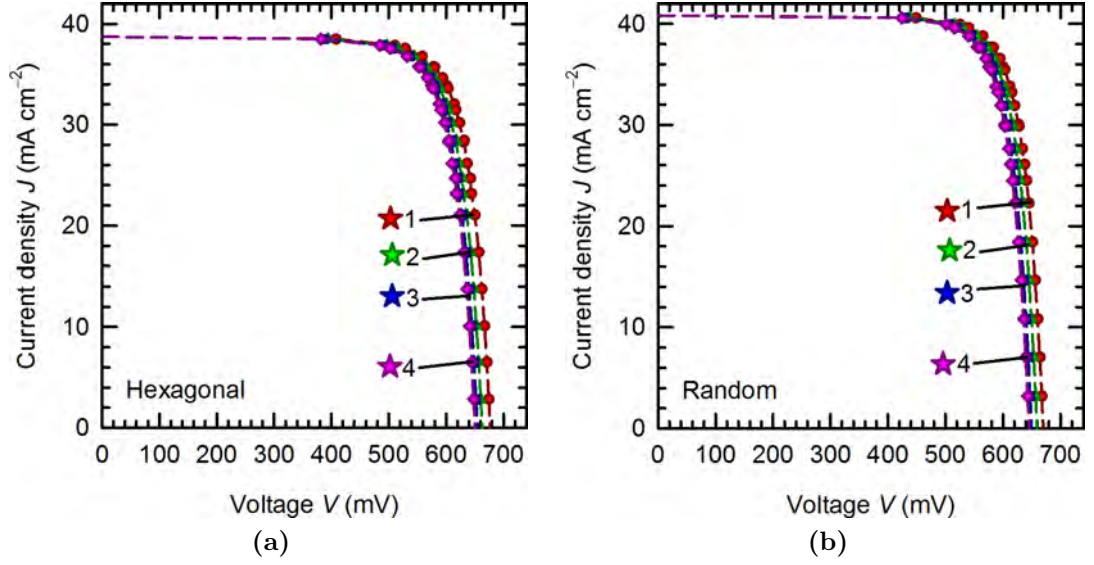


Figure 4.8: Implied J - V curves for the four calibration points (1-4) of the sample (a) with hexagonally arranged pores and (b) randomly distributed pores. The dashed lines are guides to the eye.

Table 4.3: Extracted parameters from implied J - V curves for the hexagonal and random sample for the four calibration points.

Sample	Calib. point	V_{OC} (mV)	V_{mpp} (mV)	J_{mpp} (mA cm ⁻²)	FF (%)	η (%)
Hexagonal	1	678	580	35.7	78.9	20.7
Hexagonal	2	664	566	35.7	78.7	20.2
Hexagonal	3	655	558	35.7	78.5	19.9
Hexagonal	4	651	554	35.7	78.4	19.8
Random	1	671	583	37.7	80.2	22.0
Random	2	660	573	37.7	80.0	21.6
Random	3	651	563	37.7	79.9	21.2
Random	4	646	559	37.7	79.8	21.0

Figure 4.9a and 4.9b show the local ideality factor n as a function of the voltage V for the calibration point 2 (green triangles). For the hexagonal sample, the local ideality factor is $n = 1.25$ at the open-circuit voltage $V_{OC} = 664$ mV and $n = 1.74$ at the maximum power point $V_{mpp} = 566$ mV. The local ideality factor of the random sample is $n = 1.16$ at the open-circuit voltage $V_{OC} = 660$ mV and $n = 1.48$ at the maximum power point $V_{mpp} = 573$ mV.

Since the photoluminescence signal $\ln\left(\frac{I_{PL}}{I_0}\right) \propto V$, the ideality factor can be extracted directly from the photoluminescence measurement. The gray dots in the figures show this ideality factor. It shows a similar dependency compared with the ideality factor that is calculated from the implied J - V curves.

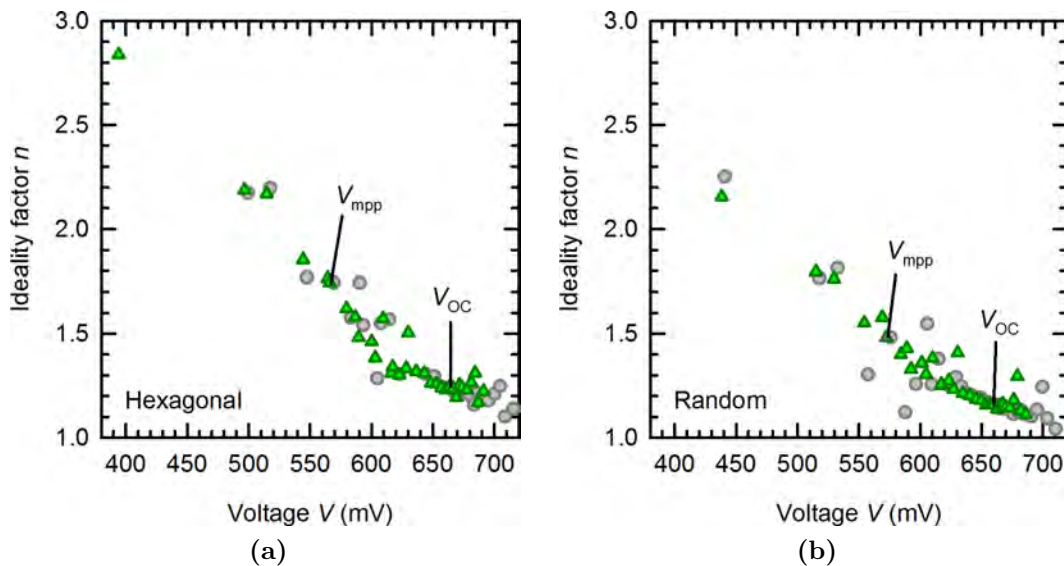


Figure 4.9: Ideality factor n as a function of the voltage V of the sample (a) with hexagonally arranged pores and (b) randomly distributed pores. The green triangles show the ideality factor determined from the implied J - V curves. The gray circles show the ideality factor directly extracted from the PL measurement.

4.6 Statistical error analysis

Various input parameters influence the extracted cell parameters from the implied J - V curves. In order to determine the resulting measurement error of the cell parameters, the input parameters of the evaluation procedure are randomly varied within their respective error range. 50×10^3 simulations for each sample ensure a sufficiently large database to determine the measurement error. This procedure is performed at the calibration point 2 which yields an efficiency most closely to the mean value.

4.6.1 Effective thickness

The effective thickness W_{eff} of the macroporous Si layer directly affects the determination of the open-circuit voltage V for calibrating the PL measurement in Eq. 4.19. Furthermore it causes the uncertainty of the photogeneration current density J_{PS}^* that is determined in Chapter 3.

In order to account for the uncertainty of the photogeneration current density, a linear dependence of the uncertainty of the photogeneration current density ΔJ_{PS}^* from the effective thickness W_{eff} is assumed. Hence, the randomly calculated photogeneration current density $J_{\text{PS,calc}}^*$ relates to a random error of the effective thickness $\Delta W_{\text{eff,rand}}$:

$$J_{\text{PS,calc}}^* = J_{\text{PS}}^* + \frac{\Delta W_{\text{eff,rand}}}{\Delta W_{\text{eff}}} \Delta J_{\text{PS}}^*. \quad (4.22)$$

Here J_{PS}^* is the measured value and ΔJ_{PS}^* is the corresponding uncertainty. $J_{\text{PS,calc}}^*$ is the photogeneration current density that is used instead of J_{PS}^* in Eq. 4.20. ΔW_{eff} is the measurement error of the effective thickness W_{eff}^* .

Table 4.4 shows the parameters required for calculating the photogeneration current density J_{PS}^* from the effective sample thickness W_{eff} for both samples.

4.6.2 Illumination intensity

The photon flux of the incident laser light is measured using a calibrated monitor solar cell. The maximum deviation $\Delta\Phi$ of three measurements of the illumination intensity is determined for the lowest photon flux of $\Phi = 1.5 \times 10^{15} \text{ cm}^{-2} \text{ s}^{-1}$. At this illumination

Table 4.4: Parameters for calculating the photogeneration current density J_{PS}^* from the effective thickness W_{eff} .

Sample	J_{PS}^* (mA cm ⁻²)	ΔJ_{PS}^* (mA cm ⁻²)	W_{eff} (μm)	ΔW_{eff} (μm)
Hexagonal	38.71	0.10	26.3	1.7
Random	40.82	0.36	26.7	5.5

intensity the maximum deviation is $\Delta\Phi < 3\%$. Hence, an uncertainty of $\Delta\Phi = 3\%$ is used for the error analysis.

4.6.3 Sample temperature

Section 4.4 considers the sample temperature as systematic error. This section accounts for the statistical error of the sample temperature T_0 and the temperature increase ΔT , since the sample temperature is not exactly known during measuring the effective carrier lifetime and photoluminescence measurement.

The temperature influences various input parameters, such as n_i , B , and kT/q . Both parameters influence the systematic temperature error from Eq. 4.15.

The statistical temperature error is considered with $T_0 = (304 \pm 1)$ K and the temperature increase $\Delta T = (5 \pm 1)$ K.

4.6.4 Effective carrier lifetime

The relative measurement uncertainty of the effective carrier lifetime τ_{eff} is typically 10%. An identical uncertainty is assumed for the actual carrier lifetime in Eq. 4.19 when calculating the calibration constant.

4.6.5 Doping density

The radiative radiation coefficient and the calculation of the calibration voltage in Eq. 4.19 depend on the doping density N_D .

The measured substrate resistivity is (1.5 ± 0.2) Ω cm. This corresponds to a dopant concentration of $N_D = (3.2 \pm 0.4) \times 10^{15}$ cm^{-3} .

4.7 Results of statistical error analysis

4.7.1 Statistical error

The statistical error is extracted from the distribution of the characteristic parameters.

Figure 4.10a and 4.10b show the distribution of the calculated efficiencies for the sample with hexagonally and randomly arranged pores, respectively. The data is fitted with the Gaussian distribution (red line) and yields the standard deviation $\Delta\eta_{\text{meas}} = 0.1\%$ for both samples.

The uncertainties of the open-circuit voltage ΔV_{OC} , maximum power point voltage ΔV_{mpp} , and the maximum power point current density ΔJ_{mpp} are determined in the same way. Table 4.5 shows these uncertainties.

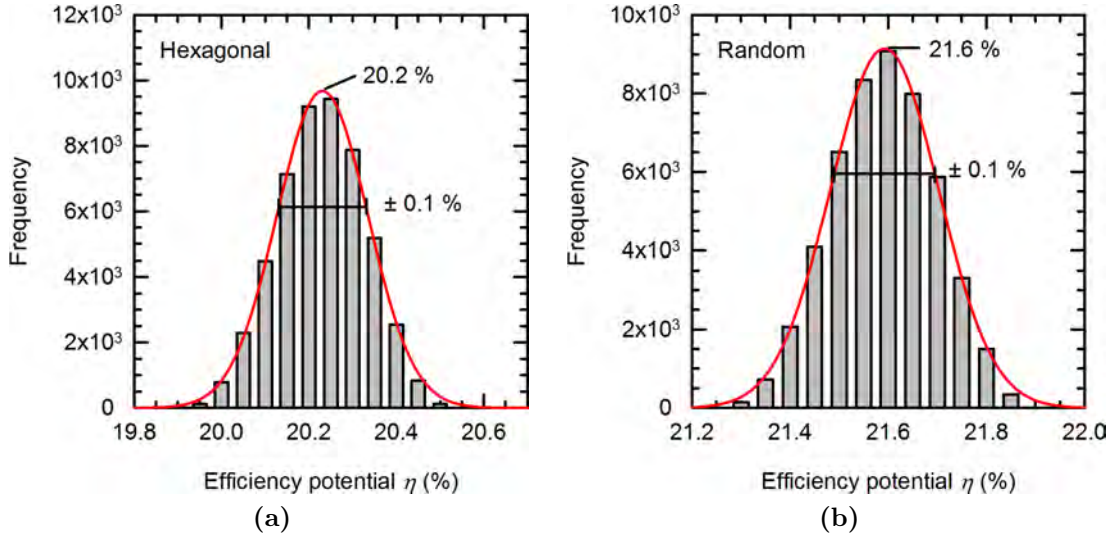


Figure 4.10: Distribution of the calculated efficiency for the sample with (a) hexagonally arranged pores and (b) randomly arranged pores. The red line is a fit of the Gaussian distribution to the data.

Table 4.5: Statistical uncertainty of extracted parameters from PL measurement for the hexagonal and random sample at calibration point 2.

Sample	ΔV_{OC} (mV)	ΔV_{mpp} (mV)	ΔJ_{mpp} (mA cm ⁻²)	$\Delta \eta_{meas}$ (%)
Hexagonal	3	3	0.1	0.1
Random	5	5	0.3	0.1

4.7.2 Correlation coefficients

In order to determine the particular impact of the measurement parameters (W_{eff} , Φ , T_0 , ΔT , τ_{eff} , and N_D) on the efficiency η from the implied J - V characteristics, the 50×10^3 efficiencies are plotted against a selected input parameter. As an example, Figure 4.11 shows the efficiency η as a function of the doping concentration N_D for the randomly arranged pores. The black line is a linear fit with a slope of 0.2687 ± 0.0005 . The scattering of the efficiency for a constant temperature is due to the uncertainty of the further input parameters. The efficiency shows a linear dependency also on the other parameters.

The slope of the linear fit yields the correlation coefficients $c_{W_{eff}}$, c_{Φ} , c_{T_0} , $c_{\Delta T}$, $c_{\tau_{eff}}$, and c_{N_D} between the efficiency η and the corresponding input parameter. Table 4.6 lists these correlation coefficients for both samples.

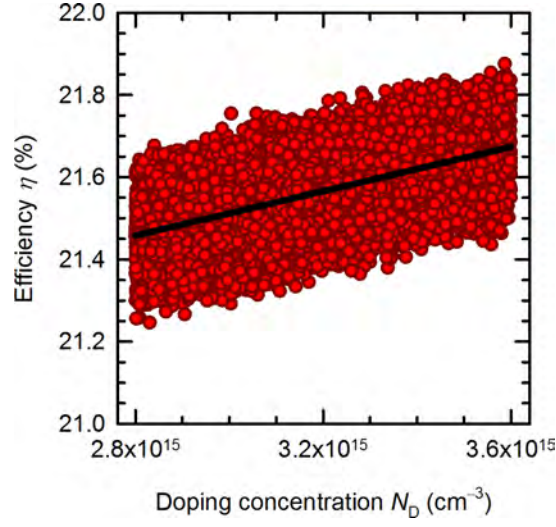


Figure 4.11: Calculated efficiency η versus doping concentration N_D for the randomly arranged pores. The black line is a linear fit to the data.

Table 4.6: Correlation coefficients $c_{W_{\text{eff}}}$, c_{Φ} , c_{T_0} , $c_{\Delta T}$, $c_{\tau_{\text{eff}}}$, and c_{N_D} for the efficiency η as a function of the varied parameters (W_{eff} , Φ , T_0 , ΔT , τ_{eff} , and N_D).

Coefficient	Hexagonal	Random
$c_{W_{\text{eff}}} (\% \mu\text{m}^{-1})$	-0.0053 ± 0.0001	-0.0029 ± 0.0001
$c_{\Phi} (1 \times 10^{-14} \% \text{cm}^2 \text{s})$	0.0038 ± 0.0001	0.0039 ± 0.0001
$c_{T_0} (\% \text{K}^{-1})$	-0.0843 ± 0.0003	-0.0883 ± 0.0002
$c_{\Delta T} (\% \text{K}^{-1})$	-0.0069 ± 0.0002	-0.0070 ± 0.0005
$c_{\tau_{\text{eff}}} (\% \mu\text{s}^{-1})$	0.0392 ± 0.0001	0.0365 ± 0.0001
$c_{N_D} (1 \times 10^{-15} \% \text{cm}^3)$	0.2587 ± 0.0004	0.2687 ± 0.0005

The efficiency most strongly correlates with the doping density N_D . The sample temperature T_0 and the effective carrier lifetime τ_{eff} also have a high impact on the efficiency. However, the impact of the other input parameters on the efficiency is negligible.

4.8 Efficiency potential results

The total uncertainty $\Delta\eta$ of the implied J - V characteristics is calculated by quadratically adding the calibration failure $\Delta\eta_{\text{calibration}}$ from Section 4.5.1 and the measurement uncertainty $\Delta\eta_{\text{meas}}$ from Section 4.7:

$$\Delta\eta = \sqrt{\Delta\eta_{\text{calibration}}^2 + \Delta\eta_{\text{meas}}^2}. \quad (4.23)$$

Thus, the efficiency potential η determined by the photoluminescence based method is $(20.2 \pm 0.4)\%$ for samples with hexagonally arranged pores and $(21.5 \pm 0.4)\%$ for samples with randomly arranged pores.

4.9 Discussion

In this work, a PL-based method using the MW-PCD measurement for calibrating the PL signal is applied to macroporous Si. Furthermore, the measured photogeneration current density is used to scale the incident photon flux. Consequently, this procedure yields implied J - V curves.

The implied J - V curves yield an efficiency potential $\eta = (20.2 \pm 0.4)\%$ for the sample with hexagonally arranged pores and $\eta = (21.5 \pm 0.4)\%$ for the sample with randomly arranged pores.

4.9.1 Effective carrier lifetime

The actual carrier lifetimes in Fig. 4.4 show a dependency on the excess carrier density which differs for the sample with hexagonally arranged pores (Fig. 4.4a) and the sample with randomly arranged pores (Fig. 4.4b). However, the carrier lifetime decreases for both samples with increasing excess carrier density for $\Delta p > 1 \times 10^{15} \text{ cm}^{-3}$.

First, the decrease in lifetime is discussed. This characteristic drop can probably be explained by the $\tau_{\text{eff}} \propto \Delta p^{-1}$ dependency of an emitter region under high injection [Kan85], since the negatively charged aluminum oxide layer [Hez89] induces an inversion layer in the n-type Si. Recombination in the inversion layer is likely to cause the decrease of the effective carrier lifetime.

However, high injection conditions are not perfectly fulfilled for accurately determining the emitter saturation current density from the measurement. The emitter saturation current density J_{0e} of the aluminum oxide is estimated with the procedure of Kane and Swanson [Kan85] for $\Delta p > 4 \times 10^{15} \text{ cm}^{-3}$ and yields $J_{0e} = 50 \text{ fA cm}^{-2}$ to 70 fA cm^{-2} . These are typical values for emitter recombination [Hoe12]. However, Werner et al. recently reported J_{0e} values as low as 2 fA cm^{-2} to 7 fA cm^{-2} for Al_2O_3 -passivated n-type Si wafers with a similar substrate resistivity [Wer13]. The difference to the measurement of this work is possibly explained with the different sample structures. In contrast to the

planar Si wafers, the macroporous Si layers have various surface orientations and a higher microscopic surface roughness.

Second, we speculate about the increase of the carrier lifetime towards higher carrier densities for $\Delta p < 1 \times 10^{15} \text{ cm}^{-3}$ of the sample with hexagonally arranged pores. This is possibly caused by an enhanced recombination at poorly passivated sample edges or at local defects in the passivation layer which has been recently reported for poorly passivated edges of Al_2O_3 -passivated n-type Si samples [Kes12, Vei13]. The characteristic $\tau_{\text{eff}} \propto \Delta p$ dependency is caused by an increased transport of holes in the inversion layer to the poorly passivated regions. Holes are the majority carriers in the inversion layer and electrons are the majority carriers in the bulk. Thus, the transport of both carrier types to the passivated regions is enhanced.

4.9.2 Photoluminescence images

The photoluminescence images in Fig. 4.5a and 4.5b show some inhomogeneities. The PL image of the sample with hexagonally arranged pores in Fig. 4.5a shows local inhomogeneities that blur with decreasing illumination intensity. These local irregularities are probably due to small local cracks in the macroporous Si layer. A similar effect was seen at poorly passivated edges of Al_2O_3 -passivated n-type Si samples [Kes12, Vei13]. This is also a possible explanation for the dependency of the carrier lifetime from the carrier density.

In contrast, the sample with randomly arranged pores does not show these local inhomogeneities and increase of the carrier lifetime for $\Delta p < 1 \times 10^{15} \text{ cm}^{-3}$. In this case, the PL signal decreases from left to right for this sample. This decrease is most likely due to etching inhomogeneities.

4.9.3 Error analysis

The temperature systematically increases with the incident photon flux Φ . For this reason, the temperature dependencies of several input parameters was considered in the evaluation of the J - V curves from the photoluminescence measurement.

For instance, considering the temperature dependence of the radiative recombination coefficient B causes a slight change of the open-circuit voltage of approximately 1 mV compared to a constant temperature.

Furthermore, the temperature dependence of the intrinsic carrier concentration $n_i(T)$ causes a 14 mV change of the extracted open-circuit voltage.

However, the temperature dependence of further input parameters such as the optical absorption A and the effective carrier lifetime τ_{eff} were not included in the calculation. The band gap energy decreases with increasing temperature [Mac58, Blu74]. Consequently, this causes the temperature dependence of the optical absorption A , the radiative recombination coefficient B , and the spectrum of the rate of spontaneous emission [Tru03].

The evaluation accounts for the temperature dependence of the radiative recombination coefficient, but not for the shift of its spectrum. The detection range of the Si CCD camera overlaps with the luminescence signal only for a small wavelength range $\lambda > 1000$ nm where the quantum efficiency of the camera strongly decreases to higher wavelengths [Hin11]. Thus, a small shift of the luminescence signal can cause a significant change of the detected signal.

Furthermore, the 10% error of the carrier lifetime changes the open-circuit voltage by approximately 3 mV. Thus, only a moderate impact on the calibration of the J - V curve is expected, as long as the temperature dependence only slightly affects the carrier lifetime.

4.9.4 Outlook

For future optimization, this work recommends to actively control the sample temperature during measuring the carrier lifetime and photoluminescence signal. This would eliminate the systematic temperature increase as a function of the photon flux Φ . Furthermore, using SiO_x instead of Al_2O_3 for passivating n-type macroporous Si samples would eliminate the injection dependence of the carrier lifetime and, thus, calculating the actual carrier lifetime from the differentially measured lifetime would not be required.

5 | Device fabrication and characterization

In this chapter, three different approaches for processing a solar cell using macroporous Si as the absorber layer are presented and discussed.

While fabrication a solar cell device from macroporous Si several technological challenges had to be solved. First, the handling of such thin films is addressed in Section 5.1. Mechanical support is required during several device processes such as wet-chemical cleaning and furnace processes at elevated temperatures.

One challenge is to individually address the front surface, rear surface and pore walls of the macroporous Si layer. The individual processing of the pore walls is addressed in Section 5.2.

Furthermore, shunting of conducting layers, such as the Al fingers, through the macropores has to be avoided. This challenge is addressed in the device process of Section 5.3.

5.1 Handling of thin films

Handling of thin macroporous Si layers has to be adapted due to the increased risk of breakage. For mechanical support of the fragile layers a laser-bonding method was developed in this work. In principle, a thin macroporous layer is bonded to a supporting substrate with this technique.

As the layer has to withstand several processes during solar cell fabrication, there are three main goals to be fulfilled. The first goal is to prevent contamination of the supported macroporous Si layer with other materials than Si – the reason is, that other materials could limit the possible processes, e.g. high-temperature steps or wet-chemical processes. The second goal is to provide sufficient mechanical stability to withstand high temperatures as well as wet-chemical processes. The third one is to provide access to both sides of the macroporous Si layer for subsequent process steps.

Figure 5.1 illustrates the procedure. (a) A CZ-Si wafer with a quadratic opening is used as the supporting wafer for the macroporous Si layer. The macroporous layer has to be a little larger (few mm) than the wafer frame. The macroporous layer is then arranged between the supporting wafer and the wafer frame. The magnetic retention force between a magnetic foil (which is an array of neodymium magnets arranged on a metal foil in this work) at the bottom and a metal frame on top clamps both wafers and the macroporous layer.

(b) In the next step, the pulsed laser is used to bond the macroporous layer with the supporting wafer. Therefore, single laser spots are shot in a distance of 100 μm into the area that is supported by the underlying wafer. Figures 5.2a and 5.2b show top view SEM

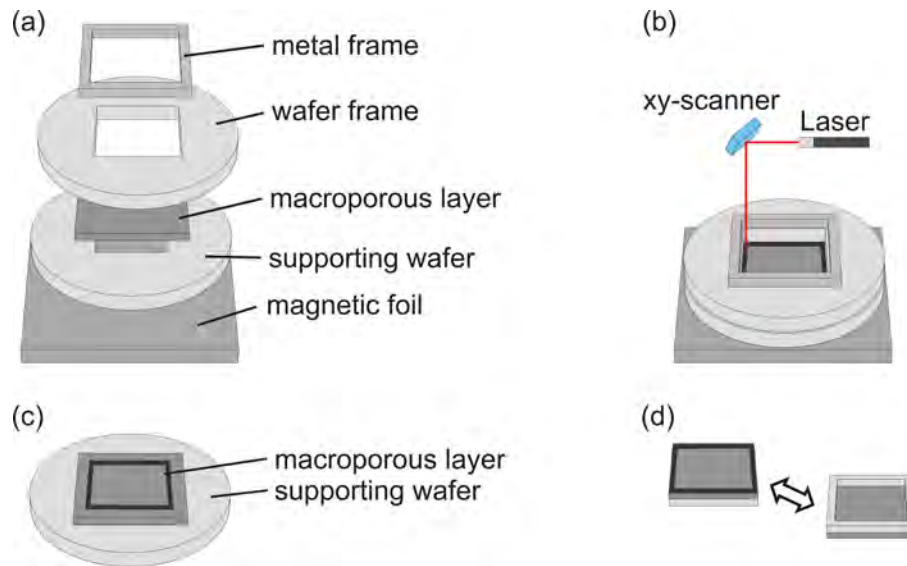


Figure 5.1: Illustration of the laser-bonding procedure. (a) Arrangement of the components. (b) Laser-bonding of the macroporous Si layer to the supporting wafer. (c) Removing of components and laser-scribing of the frame. (d) Macroporous Si layer in frame can be accessed from both sides.

micrographs of these laser spots. In this work, 10 parallel dot-lines are used to provide sufficiently high mechanical stability.

(c) Finally, the magnetic clamp and frame wafer is removed. Then, the outer frame is cut by the same laser and a supported macroporous Si layer remains (d). The typical sample size fabricated in this work is $25\text{ mm} \times 25\text{ mm}$, since this size allows to use most of the laboratory processes.

In this work also 100 mm and 150 mm wafers with more than one opening are used as supporting substrate. This allows for batch processing of 4 and 9 macroporous layers, respectively. In this case, the supporting wafer has 4 and accordingly 9 $20\text{ mm} \times 20\text{ mm}$ -sized openings.

Figures 5.3a and 5.3b show cross sectional SEM micrographs of a macroporous silicon sample laser-bonded to a silicon frame. During the laser-bonding process silicon from the macroporous Si layer and substrate is melted and ejected. Some of the molten silicon recrystallizes at the intersection from substrate to the thin macroporous Si layer and establishes a mechanical interconnection. It is important that the macroporous layer is in direct contact to the substrate during the laser-bonding procedure which is realized by the magnetic clamp. A small gap between layer and substrate would hinder mechanical bonding to the substrate.

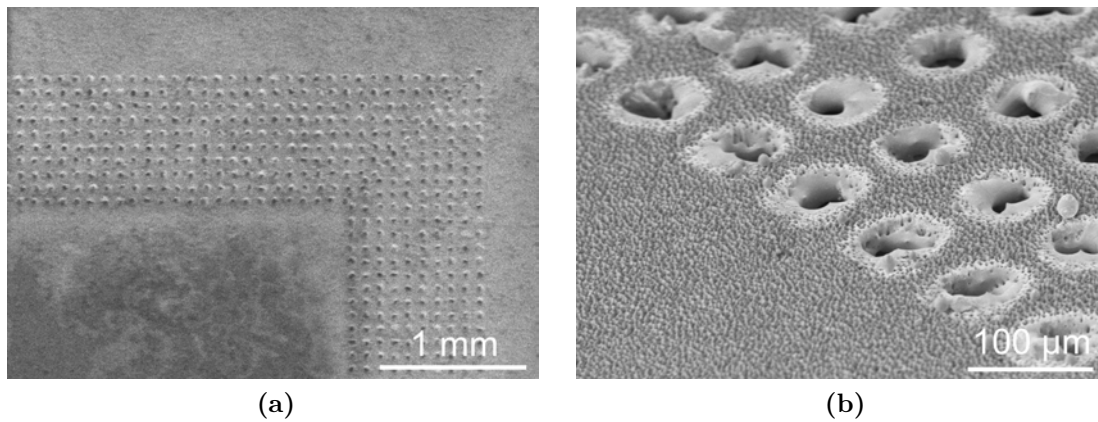


Figure 5.2: (a) Top view SEM micrograph of a macroporous silicon sample attached to a silicon frame by means of laser-bonding. (b) Tilted top view SEM micrograph of the laser-bonding spots.

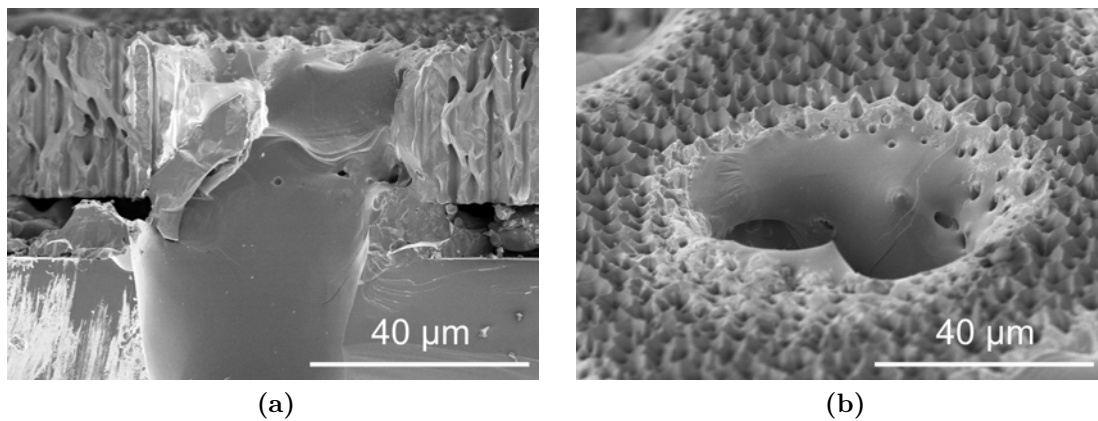
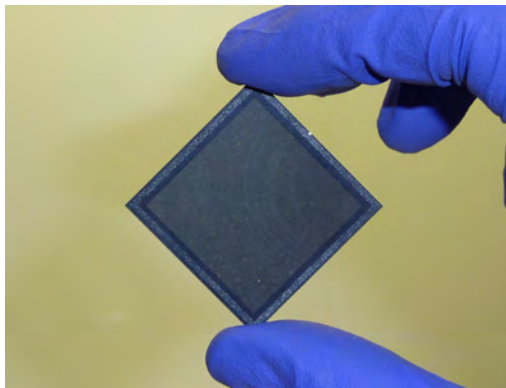


Figure 5.3: (a) Cross sectional SEM micrograph of a laser-bonding spot. (b) Magnified tilted top view SEM micrograph of a laser-bonding spot.

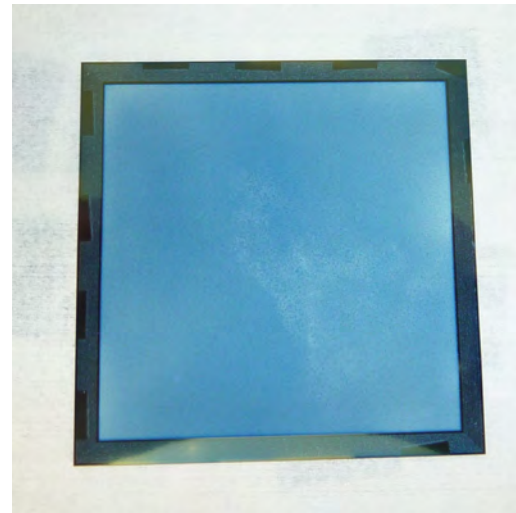
Figure 5.4a shows a photograph of a $25\text{ mm} \times 25\text{ mm}$ -sized macroporous Si layer that is attached to a silicon frame. The free-standing and both-sided accessible area is $20\text{ mm} \times 20\text{ mm}$.

However, laser-bonding of large macroporous silicon layers is also demonstrated in this work. Figure 5.4b shows a $85\text{ mm} \times 85\text{ mm}$ large macroporous layer attached to a supporting frame. The edge width of the frame is 5 mm in this case and the number of parallel dot-lines is increased to 20. The sample is shown after performing a wet chemical standard RCA-cleaning [Ker70], thermal oxidization at $900\text{ }^\circ\text{C}$ in a furnace, and plasma-enhanced chemical vapor deposition (PE-CVD) of SiN_x . This demonstrates a

sufficiently high mechanical stability of the bonding procedure. The blue color results from a thin oxide layer growth in the furnace.



(a)



(b)

Figure 5.4: (a) Photography of a 25 mm \times 25 mm-sized macroporous silicon layer attached to a silicon frame by means of laser-bonding method. (b) Photography of a 85 mm \times 85 mm-sized macroporous silicon layer attached to a silicon frame by means of laser-bonding method. The blue color results from a thin oxide layer growth in the furnace.

5.2 Individual addressing of surfaces

Due to the large surface area of the macropores an efficient passivation of the pore walls is necessary. In contrast to Chapter 4, a passivating layer is required only on the pore walls since the top and bottom part of the macroporous Si layer has to be accessible for contacting. Since no technique can provide a selective pore wall passivation, but only a selective surface passivation, the surface selective passivation is combined with a conformal technique.

Figure 5.5 illustrates the principle sequence how this challenge is solved. First, the front and rear surface are coated with a surface selective deposition technique. This layer acts as a protection layer. Then, a surface conformal technique is used to deposit a passivating layer at the pore walls. Finally, the protection layer at the front and rear side is selectively removed.

The following subsections explain the processing sequence used in this work. The process starts with a free-standing macroporous Si layer (a).

5.2.1 Surface selective deposition

(b) Plasma-enhanced chemical vapor deposition (PE-CVD) of silicon nitride (SiN_x) is used to selectively deposit the outer surfaces of macroporous layers (Plasmalab 80 Plus from Oxford Instruments). The deposition is highly surface selective due to the low process

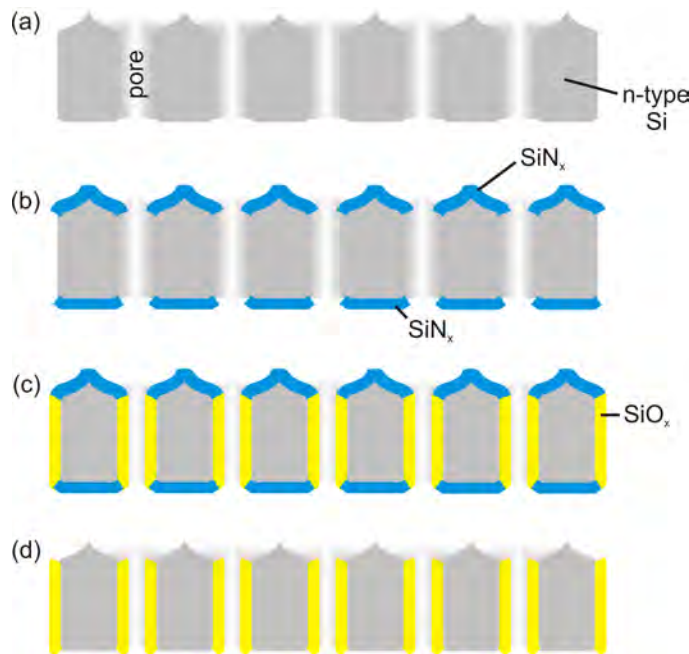


Figure 5.5: Illustration of the processing sequence for selective pore wall passivation.

pressure. The physical reason is that the direction of the ionized particles is only weakly affected by particle collisions due to the low particle density.

The macroporous Si layer is coated with a 70 nm thick SiN_x -layer on both sides with a refractive index of $n = 1.9$ after an RCA-cleaning step. The process pressure is 0.2 mbar and the set-temperature is 400 °C.

Figure 5.6a shows a cross sectional SEM micrograph of a macroporous layer with a 200 nm-thick SiN_x -layer for better visualization of the surface selective deposition. Only a thin silicon nitride film is deposited in the pores opening as shown in detail in the SEM micrograph in Fig. 5.6b. The SiN_x film covers the outer surface of the macroporous layer, but deposits hardly in the pores.

5.2.2 Pore wall passivation

(c) Then, a further RCA-cleaning step is followed by a wet thermal oxidization at 900 °C for 60 min. The RCA-cleaning procedure mainly consists of two cleaning steps SC-1 and SC-2 in order to remove particles and organic impurities as well as metallic impurities, respectively. Both steps are followed by a rinse in deionized (DI) water and a dip in 1 wt% hydrofluoric acid (HF) and a further rinse in DI-water. However, the HF-dips prior to the oxidization slightly etches the SiN_x -layer. The impact of the HF-dip duration is studied in Subsection 5.2.4.

In contrast to the surface selective PE-CVD deposition process, furnace processes such as thermal oxidization at atmospheric pressure lead to a surface conformal growth where Si is accessible. This is the case in the pores. The oxidization process results in an 80 nm-thick silicon oxide (SiO_x) layer on the pore walls.

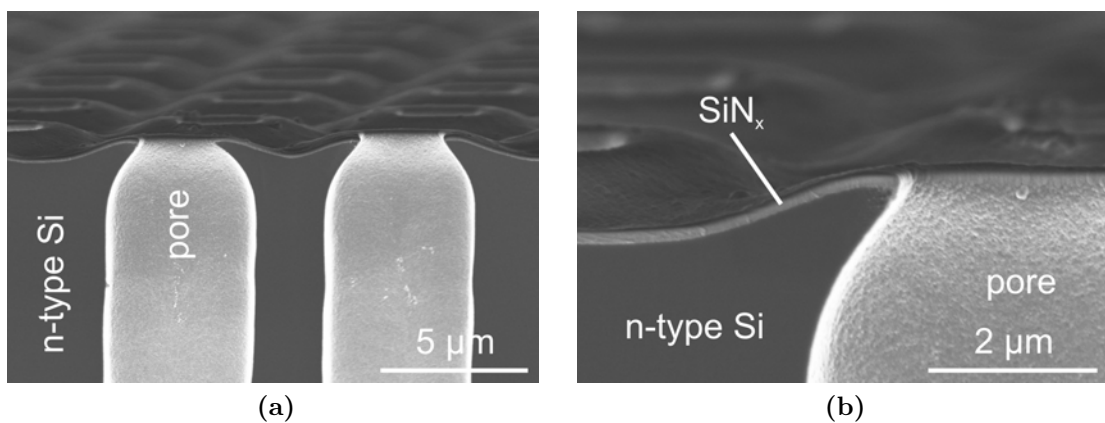


Figure 5.6: (a) Cross sectional SEM micrograph of a macroporous Si layer coated with 200 nm of SiN_x . (b) Magnification of the front surface. The SiN_x -layer is deposited on the outer surface, but hardly in the pores.

5.2.3 Selective etching

(d) Finally, the SiN_x -protection layer is selectively removed by means of wet chemical etching. For this purpose, the thermal oxidation an 1 min dip in 1 wt% HF removes a thin oxide layer grown on the SiN_x -layer [Rai76]. This step is required to make the SiN_x -layer accessible to the selective nitride etching solution. Then 85 wt% ortho-phosphoric acid (H_3PO_4) at a temperature of 140 °C is used to selectively remove the SiN_x -layer [Wil96]. Finally, the samples are rinsed in DI-water and dried with a nitrogen gas flow.

Table 5.1 shows the etching rates of SiN_x ($n = 1.9$) and SiO_x in 1 wt% HF and H_3PO_4 . H_3PO_4 etches SiN_x after oxidization with an etching rate of $(1.8 \pm 0.1) \text{ nm min}^{-1}$. The etching rate of SiO_x in H_3PO_4 is negligible.

5.2.4 Impact of HF-dip duration

SEM micrographs (compare Fig. 5.6a) show that the SiN_x thickness decreases with the distance from surface. Hence, isotropically etching of SiN_x in HF allows to control the remaining depth of SiN_x in the pores. In this experiment, the HF-dip time prior to the oxidization process is varied from 0.5 min to 15 min. The SiN_x deposition pressure is 0.2 mbar.

Figure 5.7 show cross sectional SEM micrographs of the front side of MacPSi-layers with 0.5 min and 15 min HF-dip time. The oxide reaches up to the edge of the pore for the 15 min HF-dip (Fig. 5.7b). Furthermore, some oxide is grown at the small tip at the surface between the pores. For the 0.5 min HF-dip (Fig. 5.7a) the oxide layer starts at a depth of $(3.4 \pm 0.6) \mu\text{m}$ measured from the pore opening.

During development of solar cells in this work it turned out, that full SiO_x -coverage of the pore walls is beneficial for the cell performance, since no unpassivated regions remain.

Table 5.2 shows the experimental results. The oxide depth is smaller for the rear side. The reason is the different shape of the pore walls: At the front side, the pore openings are cone shaped. Hence, SiN_x deposits much deeper into the pores compared with the bottleneck-shaped pores at the rear side. This is a kind of shadowing effect in the latter case. The oxide depth decreases with increasing HF-dip time and vanishes for HF-dip times ≥ 10 min. However, the pore shape varies between different samples and, thus, can lead to different results.

Table 5.1: Etching rates in HF and H_3PO_4 .

Sample	1 wt% HF (nm min^{-1})	85 wt% H_3PO_4 at 140 °C (nm min^{-1})
SiN_x as deposited	3.1 ± 0.1	not measured
SiN_x after oxidization	0.7 ± 0.1	1.8 ± 0.1
SiO_x	5.7 ± 0.2	< 0.01

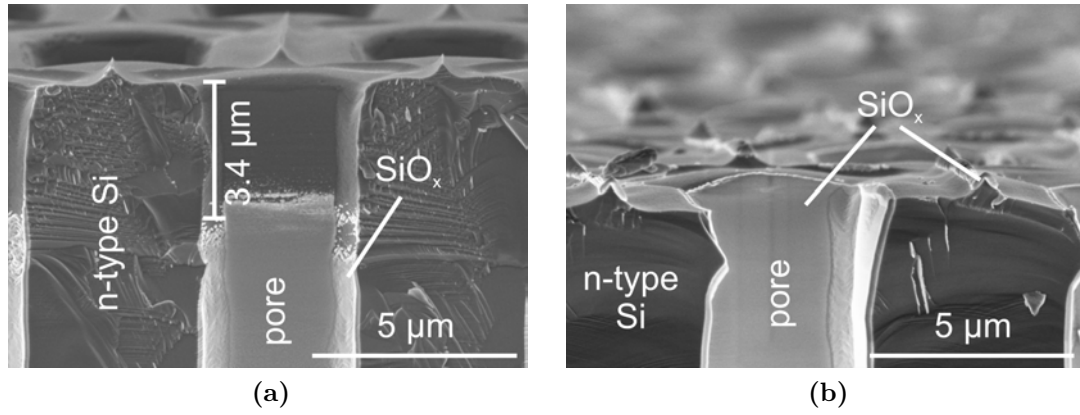


Figure 5.7: SEM micrographs of a pore wall passivated MacPSi-layers with (a) 0.5 min and (b) 15 min HF-dip prior to oxidation.

Consequently, an HF-dip time of 10 min after SiN_x deposition is used in the following solar cell processes.

Table 5.2: Variation of HF-dip time.

HF-dip time t (min)	Oxide depth front d_f (μm)	Oxide depth rear d_r (μm)
0.5	3.4 ± 0.6	1.9 ± 0.3
5.0	1.0 ± 0.2	0.6 ± 0.2
10.0	< 0.1	< 0.1
15.0	< 0.1	< 0.1

5.3 MacPSi heterojunction solar cells

This section demonstrates the processing of a heterojunction solar cell from a macroporous silicon layer. Some of the results presented here have been published by Ernst et. al in Ref. [Ern12a]. Figure 5.8 sketches the solar cell. An intrinsic amorphous silicon (a-Si)/p⁺-type a-Si/indium tin oxide (ITO) layer stack is on the front side and an intrinsic a-Si/n⁺-type a-Si/ITO layer stack is on the rear side. The pore walls are passivated with a thermally grown SiO_x-layer.

5.3.1 Solar cell preparation

Figure 5.9 shows the processing sequence. The device process starts with (100)-oriented, Czochralski-grown, 150 mm, n-type Si substrate wafers. The thickness of the wafer is (305 ± 20) μm thick and the resistivity is (1.5 ± 0.2) Ωcm . The wafer is photolithographically patterned with inverted pyramids prior to pore etching. The distance of the hexagonally arranged pyramid tips is $2r_0 = 8.3$ μm . The etching procedure is described in Chapter 1.

The pore diameter determined by SEM micrograph analysis is $2r_p = (4.7 \pm 0.2)$ μm . Thus, the geometrically calculated porosity is $p = (29.1 \pm 2.5)$ %. With the thickness $W = (33 \pm 2)$ μm of the macroporous Si layer the effective thickness is $W_{\text{eff}} = (23.4 \pm 1.6)$ μm .

85 mm \times 85 mm-sized and (33 ± 2) μm -thick macroporous Si layers are detached from the substrate wafer. The MacPSi-layer is laser-bonded to a 150 mm substrate wafer and separated into nine 25 mm \times 25 mm-sized pieces as described in Section 5.1. After that, the accessible area of the MacPSi-layers is 20 mm \times 20 mm. Planar, non-porous reference samples are processed along with these MacPSi-samples.

The pore walls of the MacPSi-samples are passivated using a thermally grown silicon oxide layer as described in Section 5.2. The total HF-dip time prior to oxidization is 10 min. Then a heterojunction solar cell processing sequence with hydrogenated a-Si is

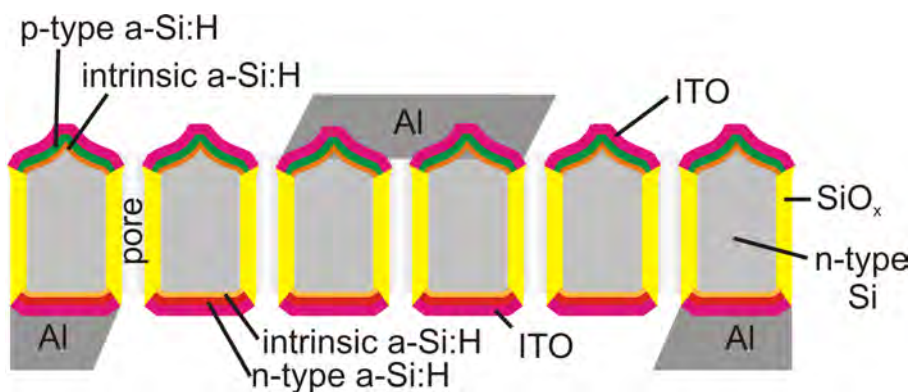


Figure 5.8: Schematic of the macroporous silicon solar cell (*not to scale*).

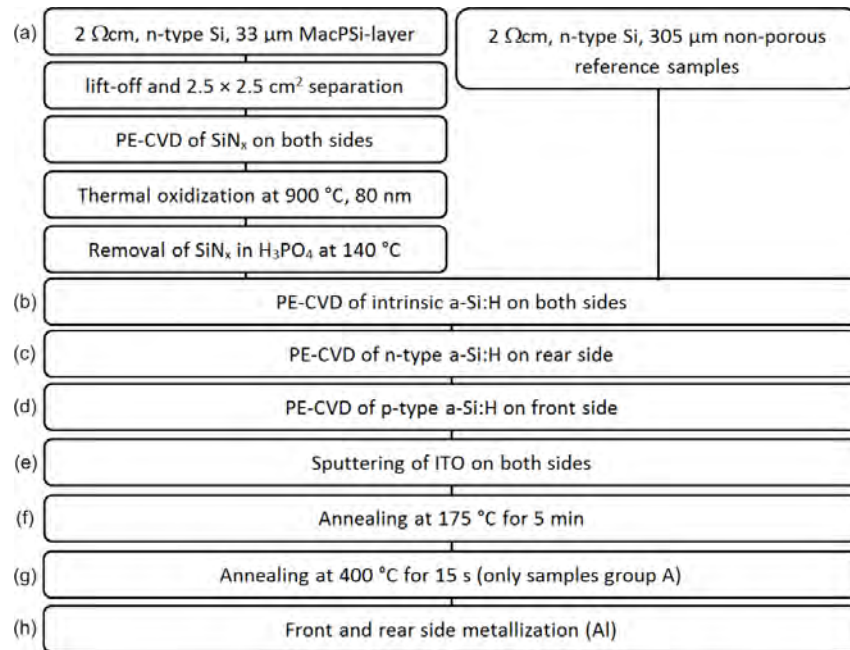


Figure 5.9: Processing sequence of the heterojunction solar cells.

applied to the MacPSi-samples and the reference samples [Tan92]. After an RCA-cleaning procedure (a), a 5 nm thick intrinsic a-Si layer is deposited on both sides of the samples by means of PE-CVD (CS 400P PE-CVD-clustersystem from von Ardenne) (b).

A 15 nm thick phosphorus-doped hydrogenated a-Si layer is deposited on the rear side of the samples (c). This is the side that was facing the electrolyte during electrochemical etching. Subsequently, a 15 nm thick boron-doped hydrogenated a-Si layer is deposited on the front side (d).

Then, a 120 nm thick conductive ITO layer is sputtered onto both sides of the samples (e). In this process, a thin unwanted ITO layer is deposited at the pore walls. This layer is removed in 1.85 vol% hydrochloric acid (HCl) for 120 s to 150 s. The final ITO thickness is approximately 80 nm and also acts as anti-reflection coating.

Annealing of the samples on a hot plate in air at 175 °C for 5 min improves the surface passivation of the samples (f).

The samples are separated into two groups (A and B). The samples of group A receive an additional annealing step on a hot plate in air at 400 °C for 15 s (g). The samples of group B do not receive this additional annealing procedure.

Evaporation of the Al grid fingers through a shadow mask at an angle of 55° to the surface normal avoids penetration of Al into the pores. This prevents electrical shunting through the pores (h).

Figure 5.10 shows the metalization scheme. The front side fingers (black lines) are interconnected by a busbar. The rear side fingers (red lines) are at interdigitated positions

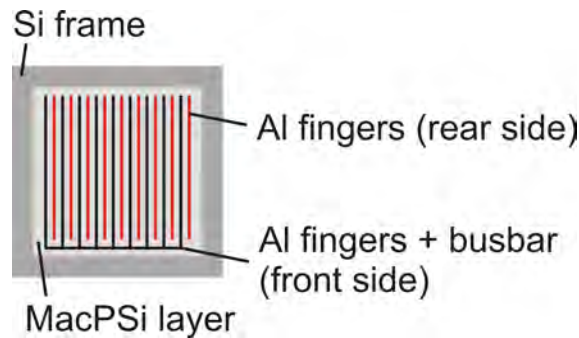


Figure 5.10: Illustration of the metalization scheme. Black lines: Front side metalization, red lines: rear side metalization.

relative to the front-side grid to further reduce the risk for shunting. The spacing between the fingers is 2 mm and the width of the Al fingers is 125 μm . Subsequent to metalization, the Si handling frame is removed and the cell area is defined to 3.92 cm^2 by laser scribing.

In order to provide mechanical stability for device characterization of the MacPSi-samples, the rear side of the macroporous solar cells is glued to a 100 μm thick metal foil with an adhesive and conductive foil (9713 from 3M).

Figure 5.11a shows a SEM micrograph of an (33 ± 2) μm -thick identically processed MacPSi-solar cell. The oblique internal structure in the Al layer results from the oblique evaporation. No Al is observed in the pores as verified by an energy-dispersive X-ray analysis.

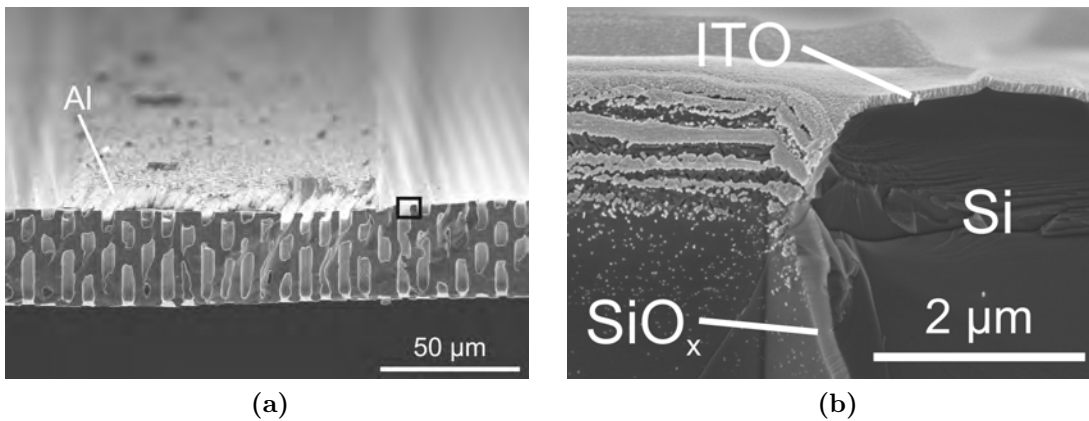


Figure 5.11: (a) Cross section SEM micrograph of an identically processed macroporous silicon solar cell with an Al finger. (b) Cross section SEM micrograph of the oxide layer on the pore walls as well as the ITO layer at the surface. Figures from Ref. [Ern12b].

Figure 5.11b shows a magnified SEM micrograph of the oxide passivation layer on the pore walls as well as the ITO layer on top. The ITO layer extends approximately $1\ \mu\text{m}$ deep into the pores where the silicon oxide layer starts. This is against the expectations from the previous Subsection 5.2.4, but can be explained by the different pore shape on the front side (compare Figs. 5.7 and 5.11). However, the transition zone between the ITO layer and the oxide layer is not clearly defined which possibly causes unpassivated regions.

5.3.2 Cell results

The illuminated J - V curves of the MacPSi and the reference cells are measured at a cell temperature of $25\ ^\circ\text{C}$ under illumination by halogen lamps. The lamp to cell distance is adjusted to reproduce the short-circuit current density of a reference cell calibrated at Fraunhofer ISE CalLab under $0.1\ \text{W cm}^{-2}$ of AM1.5g-illumination. With the same measurement setup the dark J - V curves and $J_{\text{SC}}-V_{\text{OC}}$ curves are measured.

Furthermore the external quantum efficiency under one sun bias light and reflectance of the cells are measured. In order to correct the short-circuit current densities of the illuminated J - V measurements a spectral mismatch correction is applied [Kin91].

Table 5.3 shows the J - V measurement results of the best MacPSi and reference cells that received an additional annealing at $400\ ^\circ\text{C}$ (group A) and of the cells that received only the annealing at $175\ ^\circ\text{C}$ (group B).

Sputtering of ITO degrades the surface passivation of the hydrogenated a-Si:H layer. Low temperature annealing at temperatures $T \leq 200\ ^\circ\text{C}$ is known to recover the passivation degradation of the ITO deposition [Zha11]. However, higher annealing temperatures causes a degradation of the minority carrier lifetime of such heterojunction devices due to irreversible hydrogen effusion.

The reference samples show the expected behavior: The reference cell (group B) with the low temperature annealing achieves high open-circuit voltages of $700\ \text{mV}$. With the additional annealing at $400\ ^\circ\text{C}$ the open-circuit voltage is reduced to $659\ \text{mV}$.

However, the additional annealing step improves the cell performance of the MacPSi-sample of group A despite the high temperatures. Section 5.3.3 therefore investigates the impact of the annealing procedure on the SiO_x layer and the a-Si-layer stack.

Figure 5.12a shows the dark J - V characteristics of the best MacPSi solar cell from group A (annealed at $400\ ^\circ\text{C}$). The two-diode model [Sah57] with ideality factors $n_1 = 1$ and $n_2 = 2$ is fitted to the measurement. The blue line is a plot for $n = 2$. A lumped shunt resistance of $20 \times 10^3\ \Omega\ \text{cm}^2$ is extracted from the model and, thus, verifies that shunting through the pores was avoided successfully.

The series resistance is $(2.0 \pm 0.2)\ \Omega\ \text{cm}^2$. The series resistance is mainly caused by the contact to the conductive foil as measured on non-porous reference samples. The fill factor $FF = 67.5\ \%$ of a reference sample glued to a metal foil is significantly lower than the fill factor $FF = 74.2\ \%$ of a reference sample measured without the conductive adhesive. This drop in fill factor corresponds with a series resistance of $R_{\text{series}} \approx 1.7\ \Omega\ \text{cm}^2$.

Table 5.3: Electrical solar cell results of the heterojunction solar cell.

Sample	A (cm ²)	J_{SC} (mA cm ⁻²)	V_{OC} (mV)	FF (%)	η (%)
MacPSi ^A	3.92 ^C	21.3	494	68.7	7.2
MacPSi ^B	3.92 ^C	9.8	455	66.5	3.0
Planar ref. ^A	4.25 ^D	28.9	659	74.2	14.1
Planar ref. ^B	4.25 ^D	32.1	700	76.7	17.2

^A Annealing at 175 °C for 5 min and at 400 °C for 15 s

^B Annealing at 175 °C for 5 min

^C Illuminated area is cell area.

^D Illuminated area is aperture area.

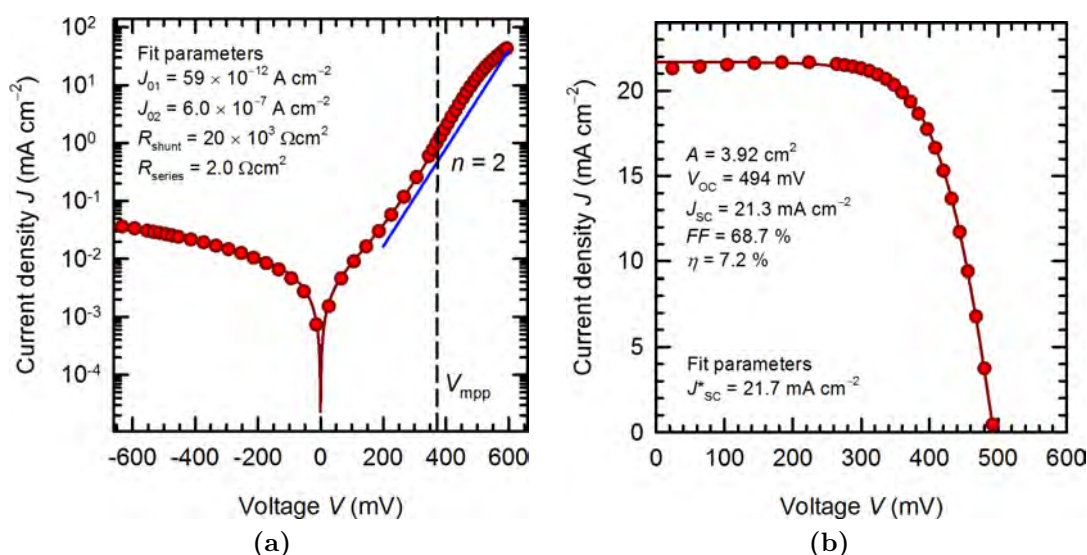


Figure 5.12: (a) In-house measured dark (circles) and fitted (line) J - V curve of the best MacPSi cell from group A. The blue line is a plot for $n = 2$. (b) In-house measured (circles) and fitted (line) J - V curve of the best MacPSi cell from group A under one sun illumination. Figures from Ref. [Ern12a].

The recombination current density $J_{01} = 59 \times 10^{-12}$ A cm⁻² as consistently determined by fitting the dark J - V curve and the so-called Suns- V_{OC} measurement [Wol63].

Figure 5.12b shows the illuminated J - V curve corrected for the spectral mismatch of the illumination source. Rather unusual, the current density increases with increasing voltage in the range of 0 mV to 250 mV. This could possibly be caused by an injection dependent surface recombination velocity at the pore walls. The fit of the illuminated J - V curve is done with all parameters as determined by fitting the dark J - V curve. The only parameter varied to fit the experimental data is the photogeneration current density J_{SC}^* .

Figure 5.13a shows the measured internal quantum efficiency IQE of the best MacPSi cells from group A and B, respectively. The annealing procedure considerably improves the quantum efficiency but still a high current loss is present compared with the IQE measurement of the reference cell from group A. The low IQE at wavelengths $\lambda > 500$ nm is caused by a high recombination at the pore walls. At low wavelengths $\lambda < 500$ nm a strong current loss appears due to parasitic absorption in the a-Si/ITO-layer stack [Hol12].

Figure 5.13b shows the inverse internal quantum efficiency IQE^{-1} versus absorption length α^{-1} . The slope for $\alpha^{-1} < W_{\text{eff}}$ yields an effective diffusion length $L_{\text{eff}} = (44 \pm 5) \mu\text{m}$ [Aro80]. This value can be understood by assuming that surface recombination at the oxide-passivated pore walls dominates (as investigated in Section 5.3.3) and yields a base saturation current density

$$J_{0,b} = \frac{qD_p n_i^2}{N_D L_{\text{eff}}} = 10 \times 10^{-12} \text{ A cm}^{-2} \quad (5.1)$$

that is of the same order of magnitude as the value $J_{01} = 59 \times 10^{-12} \text{ A cm}^{-2}$. Here q is the elementary charge, $D_p = 12 \text{ cm}^2 \text{ s}^{-1}$ the minority carrier diffusion coefficient, $n_i = 1 \times 10^{10} \text{ cm}^{-3}$ the intrinsic carrier concentration and $N_D = 3.2 \times 10^{15} \text{ cm}^{-3}$ is the donor concentration of the base.

For non-porous oxide-passivated reference samples a surface recombination velocity (SRV) of $S = (150 \pm 20) \text{ cm s}^{-1}$ is measured after sputtering an ITO layer on both sides of

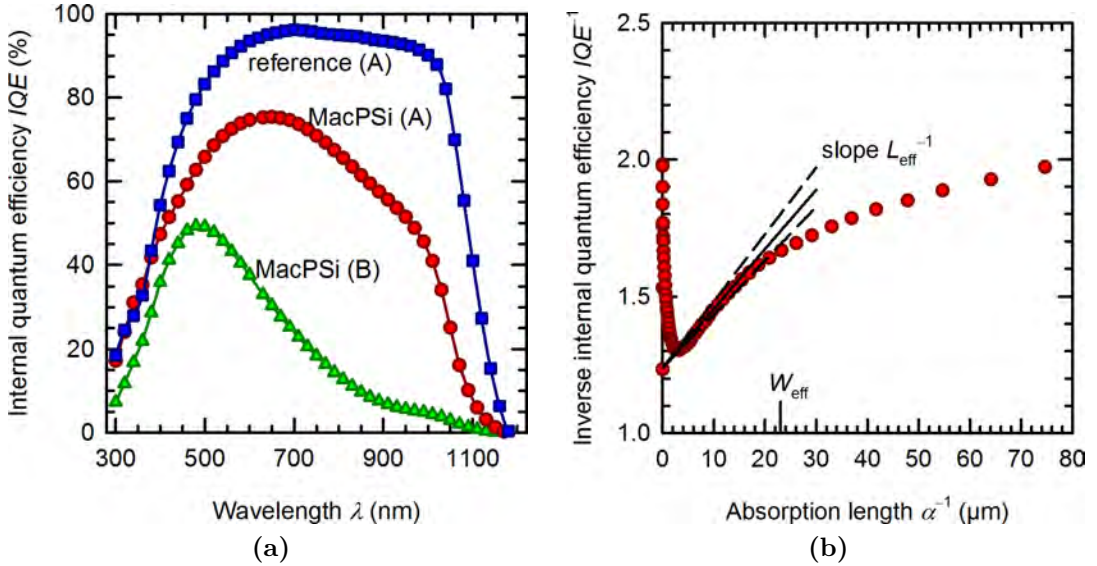


Figure 5.13: (a) Measured internal quantum efficiency IQE of the best MacPSi cells from group A and B. (b) Inverse internal quantum efficiency IQE^{-1} versus absorption length α^{-1} . Figure from Ref. [Ern12a].

the samples and subsequent annealing at 175 °C for 5 min and 400 °C for 15 s. Expressing surface recombination at the pore walls with the cylindrical surface area $A_{\text{pore}} = 2\pi r_p W$ as an effective lifetime $\tau_{\text{bulk,pore}}$ gives the relation

$$V_{\text{Si}} \left(\frac{1}{\tau_{\text{bulk,pore}}} - \frac{1}{\tau_{\text{bulk}}} \right) = S A_{\text{pore}} \quad (5.2)$$

$$\left(2\sqrt{3}r_0^2 - \pi r_p^2 \right) W \left(\frac{1}{\tau_{\text{bulk,pore}}} - \frac{1}{\tau_{\text{bulk}}} \right) = S 2\pi r_p W \quad (5.3)$$

Here V_{Si} is the silicon volume for a hexagonal unit cell with a cylindrical pore and $\tau_{\text{bulk}} = 3$ ms is the minority carrier bulk lifetime as determined by reference measurements on aluminum oxide passivated samples. If the pore walls have the SRV of the reference samples an effective bulk diffusion length of $L_{\text{bulk,pore}} = \sqrt{D_n \tau_{\text{bulk,pore}}}$ is expected, where $\tau_{\text{bulk,pore}}$ is calculated from Eq. 5.3. The effective diffusion length L_{eff} is given by [Bas93]

$$L_{\text{eff}} = L_{\text{bulk,pore}} \frac{1 + \frac{S_{\text{rear}} L_{\text{bulk,pore}}}{D_n} \tanh \frac{W}{L_{\text{bulk,pore}}}}{\frac{S_{\text{rear}} L_{\text{bulk,pore}}}{D_n} + \tanh \frac{W}{L_{\text{bulk,pore}}}} \quad (5.4)$$

The resulting value is $L_{\text{eff}} = (79 \pm 11) \mu\text{m}$ with the surface recombination velocity $S_{\text{rear}} = (50 \pm 30) \text{ cm s}^{-1}$ of the a-Si passivated rear surface. The discrepancy to $L_{\text{eff}} = 44 \mu\text{m}$ as determined by the *IQE*-analysis is possibly due to poorly passivated pore wall regions at the intersection between the oxide and the ITO layer (see Fig. 5.11b) which is not considered in this calculation. Another possible candidate is a higher surface recombination due to various crystal-orientations at the pore walls [Sch96]. The measured $L_{\text{eff}} = 44 \mu\text{m}$ is in agreement with an average SRV at the pore walls of 300 cm s^{-1} rather than $(150 \pm 20) \text{ cm s}^{-1}$.

5.3.3 Annealing of the samples

The difference between the cell references and the MacPSi cells is the oxide layer at the pore walls. The working hypothesis is that the oxide passivation degrades due to the direct plasma exhibition during the a-Si and ITO deposition.

In order to understand this behavior, two sets of reference samples from non-porous planar n-type Si wafers are prepared: The first set represents the front- and rear surface with an a-Si/ITO-layer stack. The second set of samples represents the pore walls with an SiO_x /ITO-layer stack, since a thin unwanted ITO-layer is deposited at the pore walls and, thus, covers the oxide layer. Figure 5.14 shows the processing sequence for both sample sets.

The effective carrier lifetime is measured at an excess carrier density of $\Delta p = 1 \times 10^{15} \text{ cm}^{-3}$ after every processing step using the quasi-steady-state photoconductance decay method [Sin96] for carrier lifetimes $\tau_{\text{eff}} \geq 100 \mu\text{s}$ and transient photoconductance decay method for carrier lifetimes $\tau_{\text{eff}} < 100 \mu\text{s}$ (both with WCT-120 from Sinton Instruments).

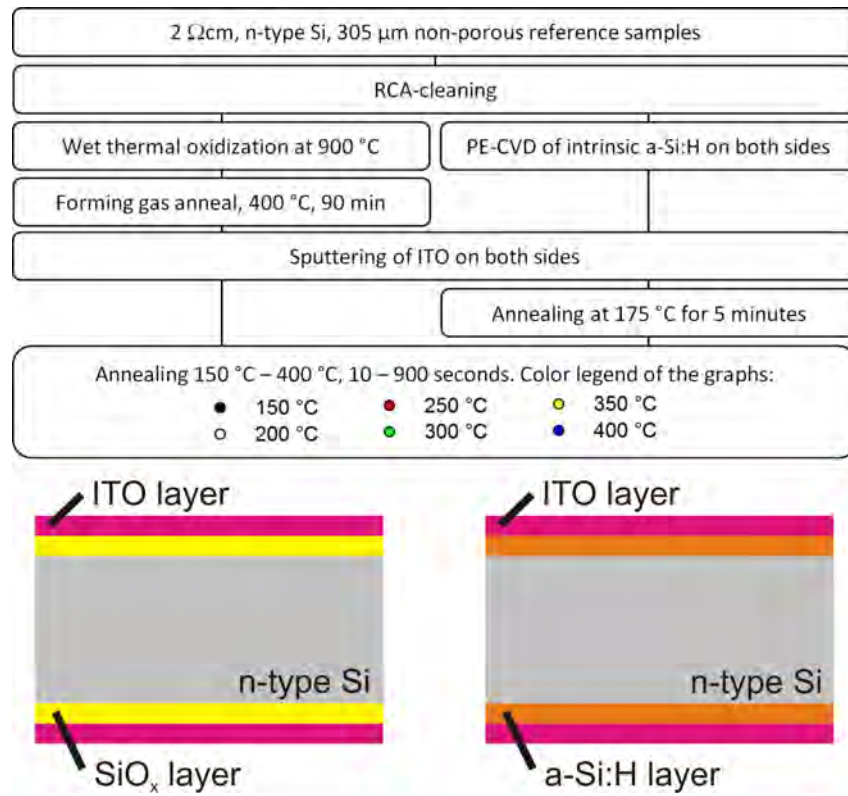


Figure 5.14: Process flow diagram of the annealing experiment.

Then, the samples are annealed on a hot plate in air and the effective carrier lifetime is measured as a function of annealing temperature and time. Figure 5.15a shows the measured effective carrier lifetimes of the a-Si/ITO samples. On the left part of the graph (gray background) shows the carrier lifetimes after the particular processing step. On the right hand side of the graph the annealing variation is shown. After the a-Si deposition the samples are well passivated with a carrier lifetime of $(1500 \pm 100) \mu$ s. Subsequent to the ITO-deposition the carrier lifetime is reduced to $(200 \pm 20) \mu$ s. However, as known from the literature the a-Si passivation is improved by an annealing step at 175 °C for 5 min. The carrier lifetime is then $(1100 \pm 100) \mu$ s. The lifetime shows no substantial degradation at annealing temperatures $T \leq 200$ °C for annealing times up to 15 min. However, with higher annealing temperatures the carrier lifetime decreases. This effect is increasing with increasing temperatures.

Figure 5.15b shows the effective carrier lifetimes of oxide passivated reference samples that received a forming-gas annealing at 400 °C for 90 min. The measured effective carrier lifetime of $(700 \pm 30) \mu$ s is reduced to only few μ s after the ITO-deposition. Annealing at temperatures $T \leq 250$ °C the effective carrier lifetime is only slightly increased. With higher annealing temperatures between 300 °C to 400 °C the carrier lifetime approaches a

maximum of (110 ± 10) μs . That is far below the lifetime prior to the ITO-deposition and proves the assumption of SiO_x passivation degradation.

In order to make a prediction which annealing temperature and time is optimal for the passivation of the macroporous samples the effective carrier lifetime is calculated using the numerical model for fully passivated macroporous layers, as described in Chapter 2. First, the surface recombination velocity S is calculated from the measured effective carrier lifetimes using the relation from Ref. [Luk87]:

$$S = \frac{W}{2} \left(\left(\frac{1}{\tau_{\text{eff}}} - \frac{1}{\tau_{\text{bulk}}} \right)^{-1} - \frac{1}{D_p} \left(\frac{W}{\pi} \right)^2 \right)^{-1} \quad (5.5)$$

Here $D_p = 12 \text{ cm s}^{-2}$ is the minority carrier diffusion coefficient and $\tau_{\text{bulk}} = 3 \text{ ms}$ is the bulk lifetime as determined by reference measurements on aluminum oxide passivated samples.

The surface recombination velocity of the front- and rear-side $S_{\text{front}} = S_{\text{rear}}$ of the macroporous samples is determined from the measured carrier lifetimes of the reference samples with an a-Si/ITO-layer stack at both sides (compare Fig. 5.15a). The surface recombination velocity S_{pore} at the pore walls is calculated from the carrier lifetimes of the oxidized reference samples with an ITO-layer at both sides (compare Fig. 5.15b).

The expected effective carrier lifetime of a macroporous layer with a pore distance $d_0 = 8.3 \mu\text{m}$, pore diameter $d_p = 4.7 \mu\text{m}$ and a thickness $W = 30 \mu\text{m}$ is calculated for all pairs of annealing temperatures and time.

Figure 5.16 shows the calculated carrier lifetimes for a macroporous Si layer. The highest lifetimes can be achieved for temperatures $T > 300^\circ\text{C}$. A further increase of the lifetime is not expected, since the recovery of the SiO_x passivation already reached its maximum value. Therefore, annealing at 400°C for 15 sec was chosen for the solar cells prepared in this work. The chosen temperature and annealing time is a compromise between degradation of the a-Si:H passivation and recovering of the SiO_x passivation.

5.3.4 Discussion

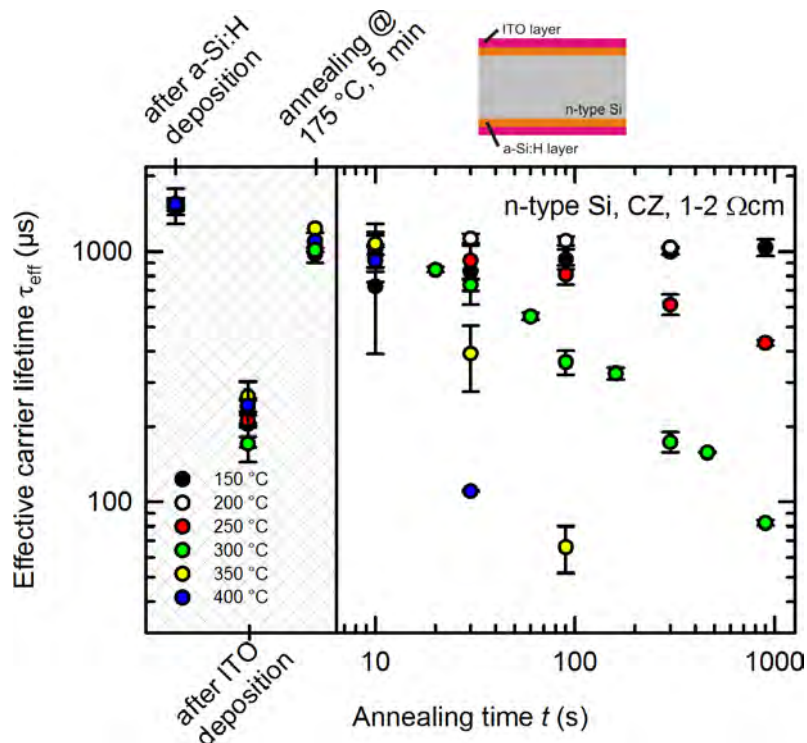
The heterojunction device process developed in this work successfully avoided shunting through the pores and included the selective passivation process of the pore walls.

However, the macroporous silicon heterojunction solar cells fabricated in this work are limited by the high recombination at the pore walls. The well passivating oxide layer with a surface recombination velocity $S = (20 \pm 1) \text{ cm s}^{-1}$ degrades during deposition of the ITO layer. Albeit annealing at temperatures between 300°C to 400°C can recover the oxide-passivation to $S = (120 \pm 15) \text{ cm s}^{-1}$ the passivation of the a-Si at the front- and rear side rapidly degrades in the same annealing procedure. The maximum efficiency achieved is $\eta = 7.2\%$ with annealing of the samples at $T = 400^\circ\text{C}$ for 15 sec.

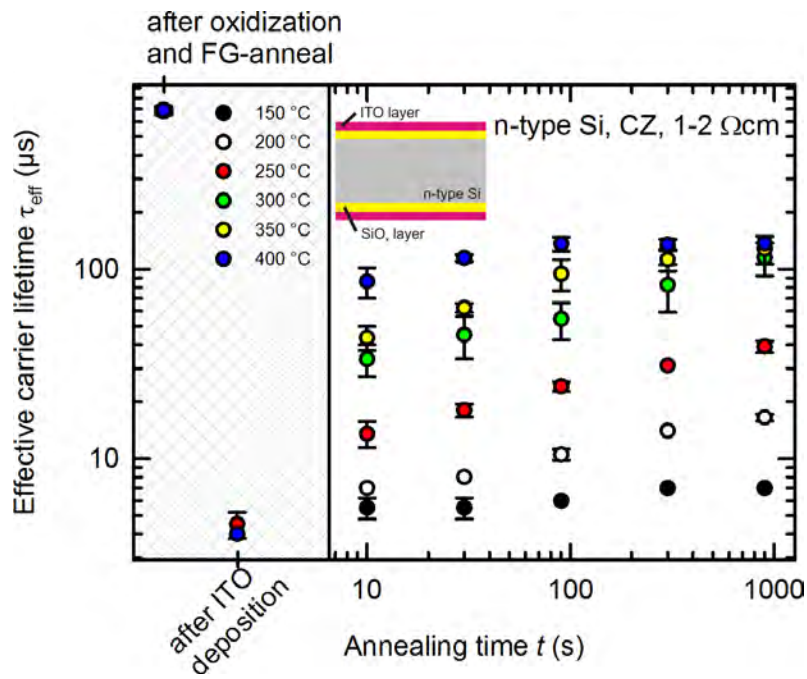
Recombination at poorly passivated regions at the intersection between the oxide and the ITO layer is another candidate for limiting the solar cell performance.

Apparently, the oxide-passivation is not the perfect choice for passivating the pore walls in this heterojunction process. An alternative is to use a conformal deposition process of well passivating intrinsic a-Si. Such a process would also simplify the processing sequence by eliminating the SiN_x deposition, thermal oxidization and selective wet chemical etching in H_3PO_4 . Unfortunately, conformal a-Si deposition is no standard-process.

In conclusion, future work will have to optimize the pore wall passivation and reduce the number of processing steps.



(a)



(b)

Figure 5.15: Measured effective carrier lifetimes of (a) reference samples with an a-Si:H/ITO-layer stack at both sides. (b) oxidized reference samples with an ITO-layer at both sides.

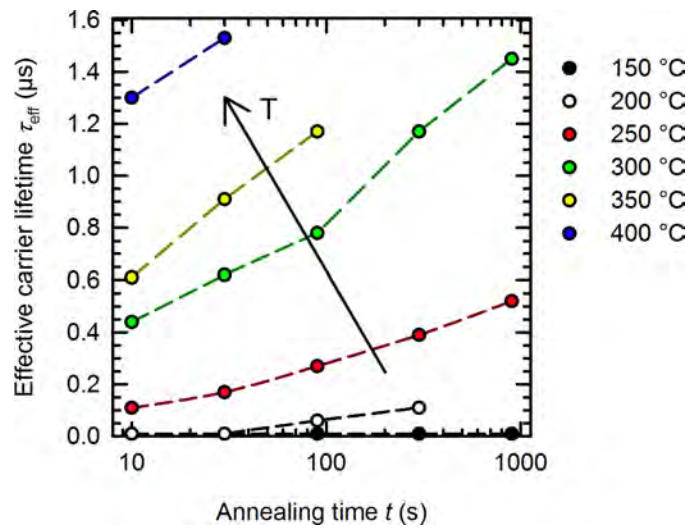


Figure 5.16: Calculated carrier lifetimes of macroporous silicon layers for various annealing temperatures and times. Lines are guide to the eye.

5.4 MacPSi solar cells with epitaxial emitter

This section investigates the epitaxial layer growth onto a macroporous Si layer. Furthermore, solar cells with such an epitaxial layer are processed. Some of the results presented here have been published in Ref. [Ern13a]. Figure 5.17 illustrates the epitaxial growth process on the rear side of a macroporous Si layer. The rear side epitaxial emitter closes the macroporous surface and, thus, eases device fabrication. In the further description these type of solar cells are termed “MacEpi solar cells”.

5.4.1 Sample preparation

Figures 5.17a to 5.17e sketch the macroporous silicon fabrication process. The process starts with identical substrates as described in Section 1.5. The wafer is photolithographically patterned with inverted pyramids in a hexagonal arrangement. The distance of the pyramid tips is $2r_0 = 8.0 \mu\text{m}$.

Figures 5.17b and 5.17c illustrate the etching of the macroporous absorber and of the separation layer, respectively. The etching procedure is describe in Section 1.8. The etched area is 133 cm^2 and has a circular shape. The separation layer is a cavity with a porosity of 100 %. The macroporous layer remains attached to the substrate only at the un-etched rim of the wafer [Ern10].

The wafer is cleaned with an RCA-cleaning procedure and subsequently atmospheric pressure chemical vapor deposition (AP-CVD) is applied at $1100 \text{ }^\circ\text{C}$ using SiHCl_3 as Si source. In this process a thin p-type silicon layer epitaxially grows onto the macroporous

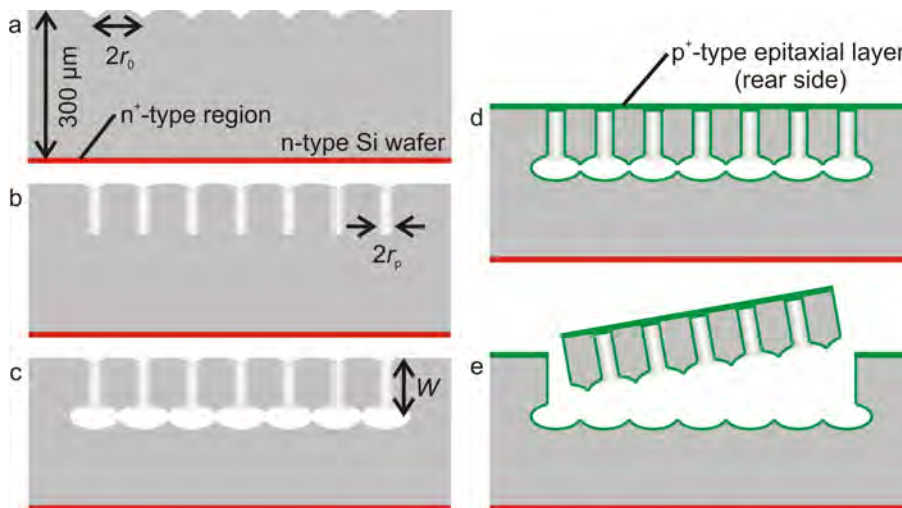


Figure 5.17: Illustration of the MacEpi process (a) starting with a pre-structured n-type Si wafer, (b) and (c) macroporous absorber and separation layer formation, (d) p⁺-type epitaxial layer growth, and (e) detachment of the layer. Figures from Ref. [Ern13a]

side of the wafer. The growth rate is $1 \mu\text{m min}^{-1}$ as measured on planar reference samples. Figure 5.17d shows the epitaxial films in green.

Figure 5.17e illustrates the detachment of the macroporous layer from the substrate.

5.4.2 Structural analysis

Figure 5.18a shows a SEM micrograph of a detached macroporous silicon layer after epitaxy. The epitaxial growth onto the rear side fully closes the pores. The pores are still open on the front side. The process results in a $W = (35 \pm 2) \mu\text{m}$ -thick sample.

Before epitaxy the pore diameter of a reference sample is $2r_p = (4.7 \pm 0.2) \mu\text{m}$. This corresponds to a porosity $p = (31 \pm 3)\%$. The area enlargement factor f compared with both sides of a planar sample is 5.35. Without pores, the surface enlargement is $f = 1$.

After epitaxy, the pore diameter of $2r_p = (3.7 \pm 0.2) \mu\text{m}$ is smaller due to the thin epitaxial layer growth on the pore walls. The porosity thus decreases to $p = (19 \pm 2)\%$.

Figure 5.18b shows an enlargement of the bottom section of Fig. 5.18a. The p^+ -type epitaxial layer that closes the macropores is brighter due to its potential contrast [Ave72]. The thickness of the epitaxial layer on the rear side is $d_{\text{rear}} = (3.0 \pm 0.2) \mu\text{m}$.

The epitaxial layer is also visible on the pore wall and has a thickness of $d_{\text{bottom}} = (0.6 \pm 0.2) \mu\text{m}$. The position of the pn-junction is marked by a dashed line on the left-hand side of Fig. 5.18b.

Figure 5.19a shows an enlargement of the top section of the sample shown in Fig. 5.18a. The pores are open on the front side. The potential contrast reveals that a thin epitaxial layer grew. This layer covers the entire surface of the n-type macropores. The dashed lines sketch the pn-junction on the left-hand side of Fig. 5.19a. The thickness of the epitaxial

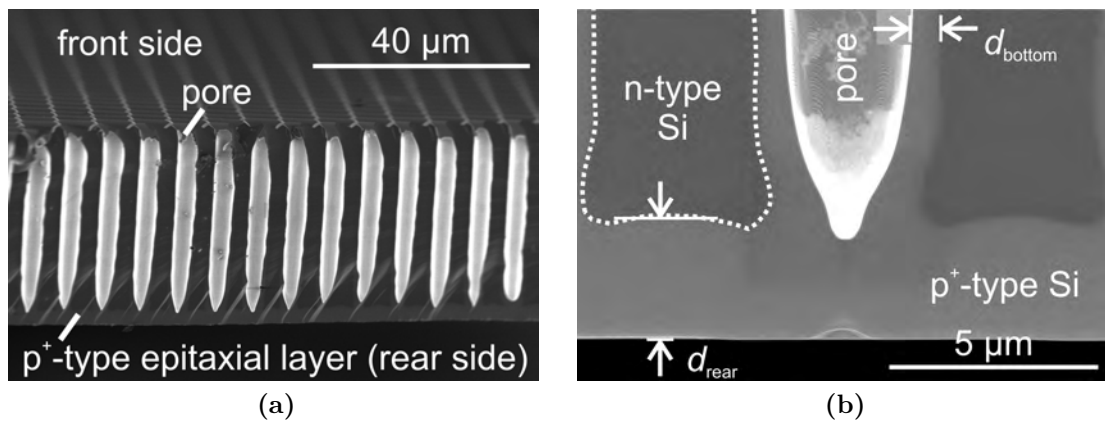


Figure 5.18: (a) Cross sectional scanning electron micrograph of a $(35 \pm 2) \mu\text{m}$ thick macroporous silicon layer with a $(3.0 \pm 0.2) \mu\text{m}$ thick p^+ -type epitaxy layer at the rear side. (b) Detailed cross sectional SEM micrograph of the p^+ -type epitaxy layer at the rear side and the pore walls. The dashed line sketches the pn-junction. Figures from Ref. [Ern13a].

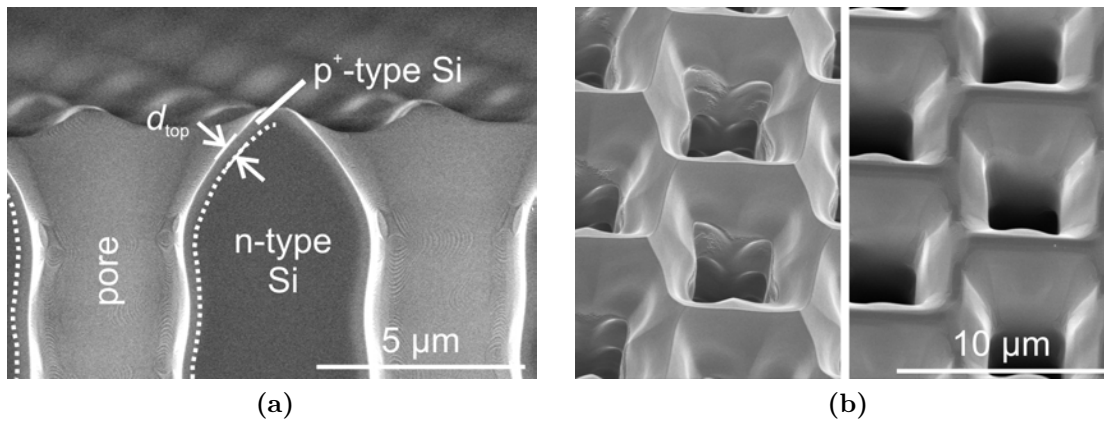


Figure 5.19: (a) Detailed cross sectional SEM micrograph of the p⁺-type epitaxy layer at the front side. The dashed line on the left half sketches the pn-junction. (b) Top-view SEM micrographs of the surface of detached macroporous silicon layers. The SEM micrograph on the left-hand side shows a MacPSi-layer prior to epitaxy. The SEM micrograph on the right-hand side shows the surface after the epitaxy. Figures from Ref. [Ern13a].

layer in this top region is $d_{\text{bottom}} = (0.3 \pm 0.1) \mu\text{m}$. A thin p-type layer growth is also observed in SEM micrographs (not shown here) on the substrate where the macroporous Si layer is separated as depicted in Fig. 5.17f.

The average thickness of the epitaxial layer from bottom to top of the pores is $d_{\text{av}} = (0.4 \pm 0.1) \mu\text{m}$ and determined by evaluating several SEM micrographs of one pore. Figure 5.20 shows these seamlessly stitched SEM micrographs. Starting at the closed bottom of the pore ($z = 0$) the gray intensity values in x -direction are measured. The measured intensity values are averaged over a 1 μm wide range in z -direction (as illustrated by the dashed box in Fig. 5.20).

Figure 5.21a shows an example intensity profile. The position of the epitaxial layer is highlighted in red.

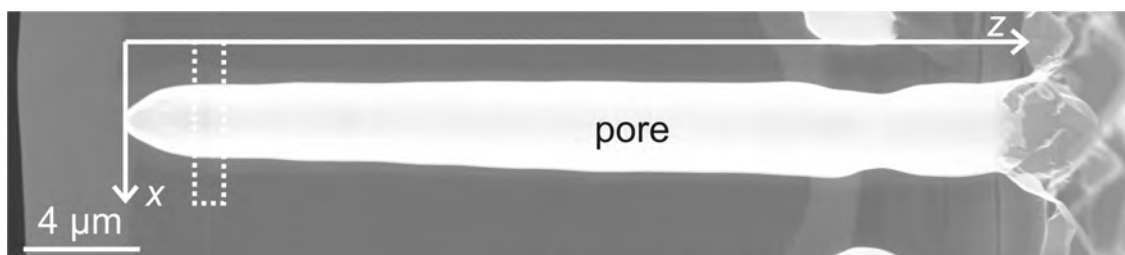


Figure 5.20: Stitched SEM micrographs for evaluating the epitaxial layer thickness in the pore. The dashed box is moved parallel to the z -axis.

The box is then moved in $1\ \mu\text{m}$ steps parallel to the pore. For each intensity profile plot the thickness of the epitaxial layer at the pore walls is determined by averaging the measured thickness at both sides. The accuracy of reading is 10 pixel for the center part of the pore and 15 pixel for the top and tail part of the pore, where the contrast is reduced due to breakage artifacts. One pixel in the SEM micrograph is equivalent to $6.5\ \text{nm}$.

Figure 5.21b shows the thickness of the epitaxy layer at the pore walls along the z -axis parallel to the pores. The thickness of the epitaxial layer at the first $10\ \mu\text{m}$ decreases from $550\ \text{nm}$ to $300\ \text{nm}$ and then stays constant at this value. The epitaxial layer thickness apparently increases for $z \geq 24\ \mu\text{m}$ and is probably due to the reduced contrast caused by the breakage artifacts. The average thickness of the epitaxial layer is $(0.4 \pm 0.1)\ \mu\text{m}$.

5.4.3 Doping profile

The acceptor concentration is measured by electrochemical capacitance voltage profiling (CVP21 profiler from WEP). Figure 5.22 shows the dopant concentration profile for an epitaxial layer deposited on a planar reference wafer (circles) and onto a macroporous silicon sample (triangles). The acceptor concentration is constant at a level of $(3.5 \pm 0.2) \times 10^{18}\ \text{cm}^{-3}$. The reference epitaxial layer is $(4.7 \pm 0.2)\ \mu\text{m}$ thick and, thus, has a sheet resistance of $R_{\text{ref}} = 35\ \Omega$.

The apparent increase of the acceptor concentration at a depth of $(2.8 \pm 0.2)\ \mu\text{m}$ for the macroporous silicon sample is an artifact. SEM micrographs taken after profiling show

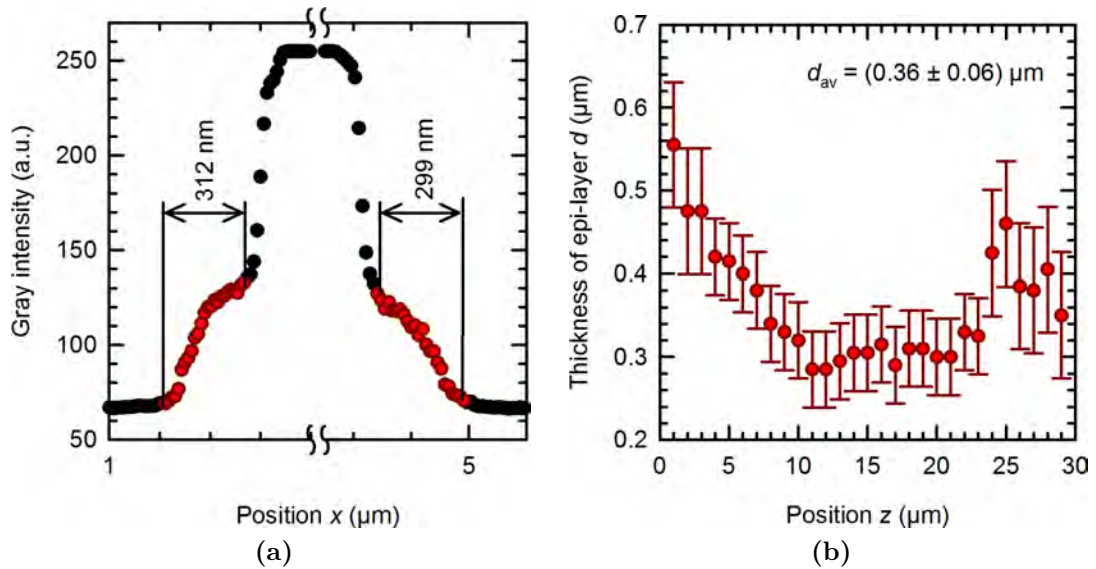


Figure 5.21: (a) Sample gray intensity profile of the epitaxial layer at the pore walls (highlighted in red). (b) Thickness of the epitaxial layer at the pore walls as a function of the position z measured from the epitaxial layer at the rear side.

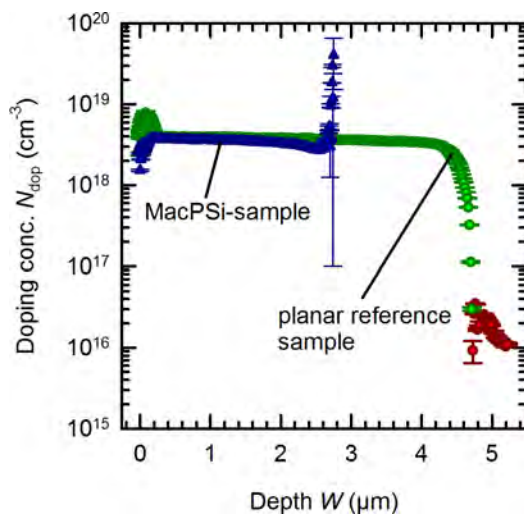


Figure 5.22: Doping concentration profile of the p-type epitaxial layer measured on a planar reference wafer (green and red dots) and on a macroporous silicon sample (blue triangles). Figure from Ref. [Ern13a].

open pores at the epitaxial surface. At this time the etched area increases abruptly which causes a sudden increased capacitance.

The sheet resistance of the (3.0 ± 0.2) μm -thick epitaxial layer on the macroporous sample is $R_{\text{MacEpi}} = 55 \Omega$.

The sheet resistance in the pores is $R_{\text{Pore}} = 450 \Omega$ when assuming that the acceptor concentration is also $3.5 \times 10^{18} \text{ cm}^{-3}$.

5.4.4 Carrier lifetime

The effective carrier lifetime of a macroporous silicon sample is measured after epitaxial growth. Surface passivation is required to achieve large effective lifetimes. First, the detached MacEpi film is separated into $25 \text{ mm} \times 25 \text{ mm}$ -sized pieces by laser cutting. These samples are then RCA cleaned. A 20 nm-thick Al_2O_3 layer is deposited onto both sides of the sample by plasma-assisted atomic layer deposition (PA-ALD). Due to the conformal growth of the Al_2O_3 layer the resulting layer thickness is 40 nm in the pores. Subsequently, the samples are annealed in air on a hot plate at 425°C for 20 min to improve the interface [Hoe06, Hoe07].

Figure 5.23 shows the photoconductance decay as measured using the MW-PCD technique. The effective lifetime extracted from the transient is $\tau_{\text{eff}} = (12.8 \pm 1.3) \mu\text{s}$.

An average surface recombination velocity $S = (22 \pm 4) \text{ cm s}^{-1}$ is required for this lifetime when assuming a bulk lifetime that is only limited by auger and radiative recombination processes in the numerical model from Chapter 2. This S value describes the recombination in the epitaxial layer and at its surface.

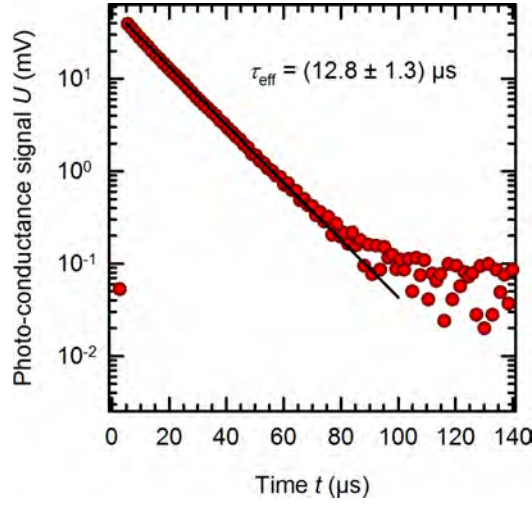


Figure 5.23: Photoconductance decay (red circles) of a surface passivated MacEpi layer as measured by the MW-PCD technique. The solid black line is a fit for a carrier lifetime of 12.8 μs . Figure from Ref. [Ern13a].

The corresponding saturation current density [Cue04]

$$J_0 = q2f \frac{n_i^2}{N_D} = (12.6 \pm 2.4) \times 10^{-13} \text{ A cm}^{-2} \quad (5.6)$$

follows from the elementary charge q , the surface enlargement factor $f = 5.35$, the intrinsic carrier concentration $n_i = 1 \times 10^{10} \text{ cm}^{-3}$, and the donor concentration $N_D = 3 \times 10^{15} \text{ cm}^{-3}$.

5.4.5 Solar cell preparation

Subsequent to the epitaxy, a laser cuts the detached MacEpi films into 25 mm \times 25 mm-sized pieces. Then, the samples are bonded to a silicon frame as described in Section 5.1.

Figure 5.24 sketches the solar cell with the epitaxial pore closure on the rear side of the device. The front side has open pores. The cell process starts with an RCA-cleaning. Then, a 70 nm thick SiN_x film with a refractive index of $n = 1.9$ is deposited by PE-CVD onto the front side. A further RCA-cleaning is followed by a wet thermal oxidization at 900 $^\circ\text{C}$ that creates a 80 nm thick passivating oxide layer on the pore walls and on the rear side. In 140 $^\circ\text{C}$ hot 85 wt% ortho-phosphoric acid the SiN_x layer is selectively removed from the front side.

By etching in 20 vol% potassium hydroxide (KOH) at 70 $^\circ\text{C}$ for 15 s the thin p-type layer at the front side is removed. In this step, the oxide layer on the pore walls and on the rear side acts as protection layer.

Another RCA-cleaning is followed by a 60 Ω phosphorous diffusion from POCl_3 at 865 $^\circ\text{C}$ in a quartz furnace. The phosphosilicate glass is then removed in an 1 wt% HF-solution.

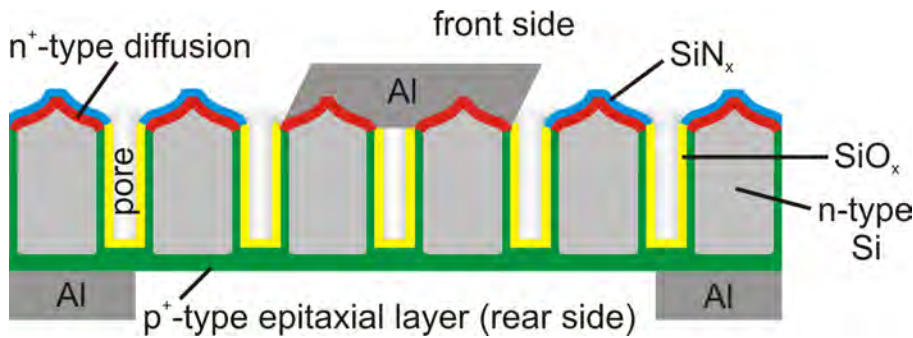


Figure 5.24: Schematics of the macroporous silicon solar cell (*not to scale*). The p-type epitaxy is colored in green. An n^+ -type diffusion (red) and a SiN_x layer (blue) is at the front side and a SiO_x layer (yellow) is at the pore walls. Figure from Ref. [Ern13a].

The oxide layer at the rear side is selectively removed by using a 40 wt% HF-saturated lint-free cloth which is followed by another RCA-cleaning. Two cycles of plasma-assisted atomic layer deposition (PA-ALD) generate a 0.24 nm-thick AlO_x tunneling layer on the front surface. One ALD cycle is equivalent to 0.12 nm aluminum oxide [vH07]. This layer prohibits a diffusion of the front contact aluminum through the front side diffusion.

Inclined evaporation through a shadow mask of the Al grid fingers on the front side at an angle of 55° to the surface normal avoids penetration of Al into the pores. The spacing between the fingers is 2 mm and the width of the Al fingers is 110 μm .

Then a SiN_x double layer is deposited for front surface passivation and anti-reflection coating. The double layer consists of a 10 nm layer with a refractive index of $n = 2.4$ and a 100 nm layer with a refractive index of $n = 2.05$ as measured on planar reference samples. The interface is improved by annealing the samples in air on a hot plate at 350°C for 2 min.

The rear-side grid is evaporated at interdigitated positions relative to the front-side grid (see Fig. 5.24). The metalization scheme is equivalent to the heterojunction solar cells as sketched in Figure 5.10. Subsequent to metalization, the Si handling frame is removed and the cell area is defined to 3.92 cm^2 .

Then, the rear side of the thin macroporous silicon solar cells is glued to a 100 μm thick metal foil by means of a conductive silver glue (CE 3103 from Emerson Cuming) in order to provide mechanical stability. This liquid glue has a lower resistivity than the conductive foil from the heterojunction solar cells. The closed rear side of the MacEpi solar cells allows to use a liquid glue instead of a conductive foil.

Finally, the samples are cured in air on a hot plate at 150°C for 5 min to improve the electrical conductivity and adhesion of the glue. Figure 5.25 shows a photo of the MacEpi cell glued to a metal foil.

Planar, non-porous reference samples are processed along with the MacEpi samples. The reference samples are from an identical substrate wafer and receive the same p-type epitaxy at the rear side. One of the planar references is not glued to a metal foil.

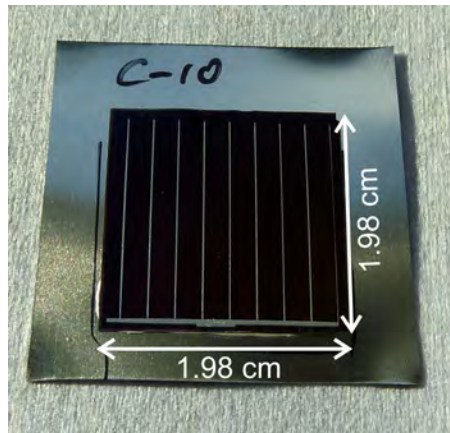


Figure 5.25: Photo of the MacEpi cell glued to a metal foil. Figure from Ref. [Ern13a].

5.4.6 Cell results

Electrical characteristics

The illuminated J - V curves are measured at 25 °C under one sun illumination by halogen lamps in a home built cell tester. The lamp to cell distance is adjusted to reproduce the short-circuit current density of a cell that was calibrated at Fraunhofer ISE CalLab under 0.1 W cm^{-2} of AM1.5g-illumination. After measuring the external quantum efficiency under one sun bias light, a spectral mismatch correction is applied in order to correct the short-circuit current density for AM1.5g-illumination [Kin91]. Furthermore, the dark J - V curves and $J_{\text{SC}}-V_{\text{OC}}$ curves are measured with the same cell testing equipment.

The MacEpi solar cells are illuminated through a $15 \text{ mm} \times 15 \text{ mm}$ -sized mask to exclude edge regions, since an increased series resistance is observed by photoluminescence imaging [Gla10] when using the experimental setup described in Ref. [Hin11]. The planar reference cells are illuminated through a mask with the size of 4.25 cm^2 .

Figure 5.26a shows the J - V curve of the best out of three MacEpi cells. It has an open-circuit voltage of $V_{\text{OC}} = 544 \text{ mV}$ and a short-circuit current density of $J_{\text{SC}} = 37.1 \text{ mA cm}^{-2}$. With the fill factor $FF = 65.1\%$, the cell achieves an energy-conversion efficiency of $\eta = 13.1\%$. The open-circuit voltage of this cell is $V_{\text{OC}} = 560 \text{ mV}$ without the mask.

Table 5.4 lists the measured parameters for the MacEpi cells and planar references.

The lumped shunt resistance $R_{\text{shunt}} = 6.7 \times 10^3 \Omega \text{ cm}^2$ is determined from the dark J - V curve at -0.5 V by Ohm's law.

The lumped series resistance

$$R_{\text{S,FF}} = \frac{V_{\text{OC}}}{J_{\text{SC}}} \left(1 - \frac{FF}{pFF} \right) = 2.3 \Omega \text{ cm}^2 \quad (5.7)$$

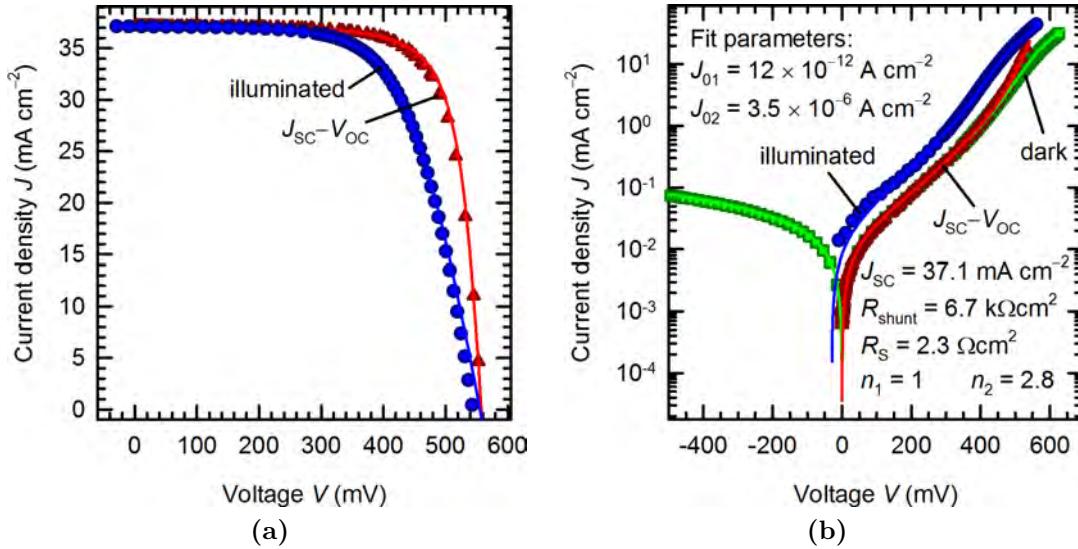


Figure 5.26: (a) In-house measured illuminated J - V curve (blue circles) and J_{SC} - V_{OC} curve (red triangles) of the MacEpi cell. The solid blue and red lines are fits from a two-diode model for the parameters shown in Fig. 5.26b. (b) Illuminated J - V curve (blue circles), dark J - V curve (green boxes), and J_{SC} - V_{OC} curve (red triangles) of the MacEpi cell. The solid blue, green, and red lines are fits from a two-diode model for the parameters given in the figure. Figures from Ref. [Ern13a].

follows from the measured values of V_{OC} , J_{SC} and FF and the measured pseudo fill factor pFF that is extracted from the J_{SC} - V_{OC} measurement after shifting by J_{SC} [Gre98].

Series resistance imaging

Figure 5.27 shows an electroluminescence (EL) and a series resistance image of a planar reference sample glued to a metal carrier. The series resistance image was determined by applying a method based on photoluminescence imaging for a spatially resolved coupled determination of the dark saturation current and series resistance (C-DCR) [Gla10] using the experimental setup described in Ref. [Hin11]. The silver glue is visible in the EL-image but almost disappears in the series resistance image, thus indicating the low impact of the silver glue to the series resistance. The series resistance is increased at the cells edges.

Figure 5.28a shows a series resistance image of the best MacEpi-cell obtained by applying the C-DCR method. The series resistance is almost constant in the center of the cell and increases to the sample edges. A rear side finger is broken on the right-hand side of the cell. The dotted red lines illustrate the position of the fingers at the rear side. The fingers at the rear side are not interconnected by a busbar and do not cover the full sample height in order not to overlap with the metalized regions at the front side. Figure 5.29 shows a normalized histogram plot of the series resistance of the total cell area in dark gray and of

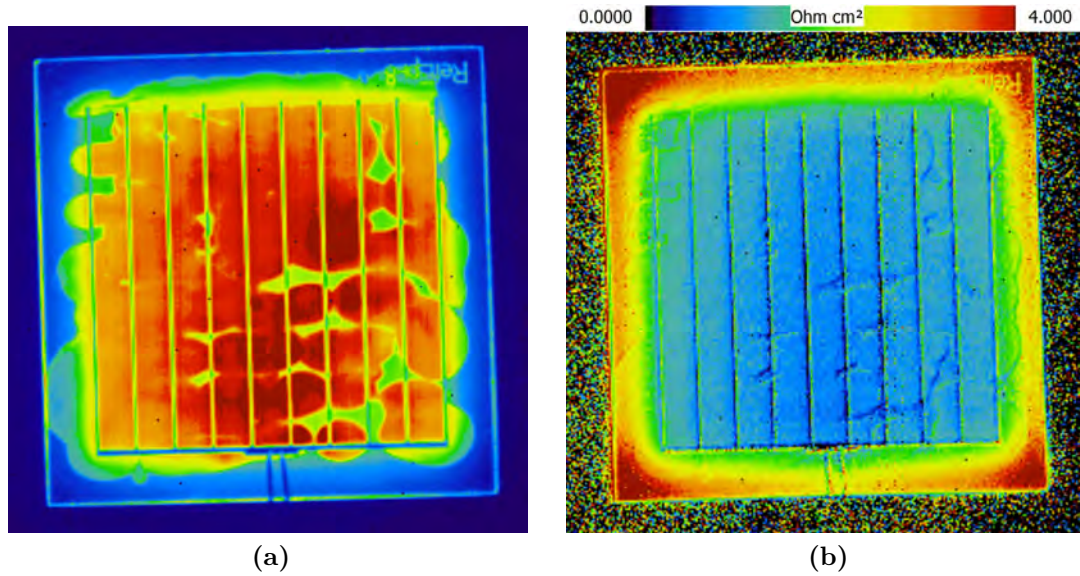


Figure 5.27: (a) Electroluminescence image of a planar reference sample glued to a metal foil at 620 mV. Color scale is in arbitrary units. (b) Series resistance image of the planar reference sample from Fig. 5.27a determined using the C-DCR method.

Table 5.4: Electrical solar cell results of the epitaxial solar cells.

Sample	A (cm ²)	J_{SC} (mA cm ⁻²)	V_{OC} (mV)	FF (%)	pFF (%)	η (%)
Best	3.92 ^A	33.8	560	56.6	74.2	10.7
Mean ^B	3.92 ^A	34.1 ± 0.3	575 ± 18	55.3 ± 1.3	72.0 ± 2.5	10.9 ± 0.3
Best	2.25 ^C	37.1	544	65.1	77.0	13.1
Mean ^B	2.25 ^C	36.7 ± 0.4	560 ± 17	62.2 ± 2.9	74.6 ± 3.1	12.8 ± 0.4
Planar ref. ^D	4.25 ^C	30.5	632	74.6	77.5	14.4
Planar ref. ^E	4.25 ^C	30.0	634	75.5	77.2	14.4

^A Illuminated area is cell area.

^B Average cell parameters of three MacEpi cells.

^C Illuminated area is aperture area.

^D Planar reference cell glued to a metal foil.

^E Non-glued planar reference.

the masked cell area in light gray. The average series resistance obtained by the C-DCR method is $R_{S,PL} = (3.7 \pm 2.8) \Omega \text{ cm}^2$ for the full cell area and $R_{S,PL} = (2.8 \pm 1.7) \Omega \text{ cm}^2$ for the $15 \text{ mm} \times 15 \text{ mm}$ -sized illuminated area.

Figure 5.28b shows a line-scan of the series resistance parallel to the busbar averaged over a 5 mm high rectangle as sketched in Fig. 5.28a. The series resistance shows a strong increase to the wafer edges and a slight increase in between two front-side fingers.

Quantum efficiency

Figure 5.30 shows the hemispherical reflectance R and the internal quantum efficiency IQE of the MacEpi cell. The reflectance is $\leq 3\%$ for wavelengths ranging from 400 nm to 900 nm .

5.4.7 Discussion

Epitaxial layer growth

The thickness of the epitaxial layer on a planar reference sample $d_{\text{ref}} = (4.7 \pm 0.2) \mu\text{m}$ is larger than the epitaxial layer thickness $d_{\text{rear}} = (3.0 \pm 0.2) \mu\text{m}$ on the rear side of the macroporous sample.

The amount of material corresponding to the difference in thickness $\Delta d = d_{\text{ref}} - d_{\text{rear}} = 1.7 \mu\text{m}$ is good for covering the walls with an epitaxial layer thickness of $\Delta d/2f = 0.16 \mu\text{m}$

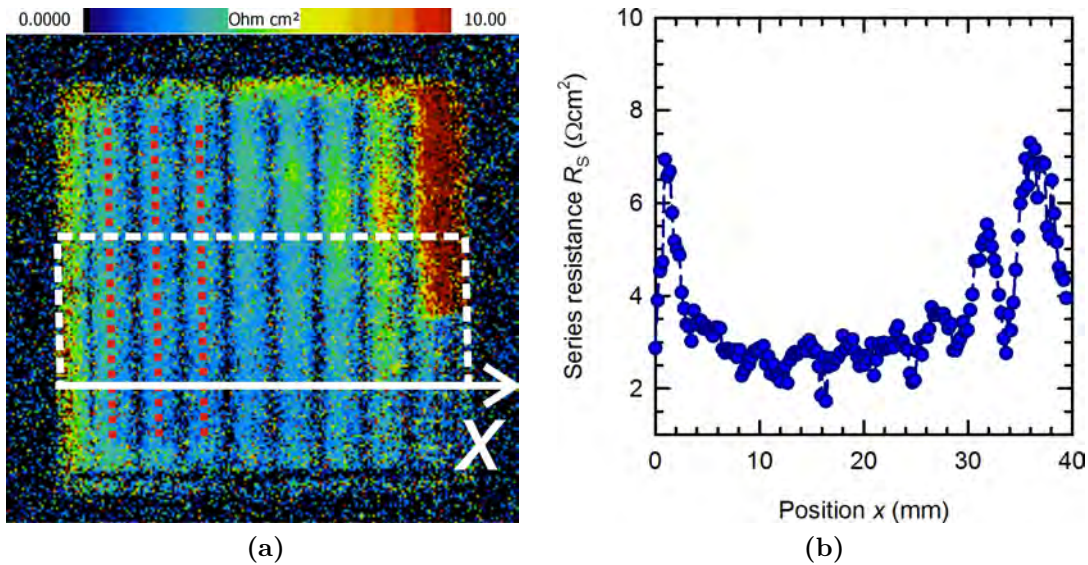


Figure 5.28: (a) Series resistance image obtained by the C-DCR method of the best MacEpi-cell. (b) Averaged line-scan of the series resistance of the best MacPSi-cell. The position x is parallel to the busbar.

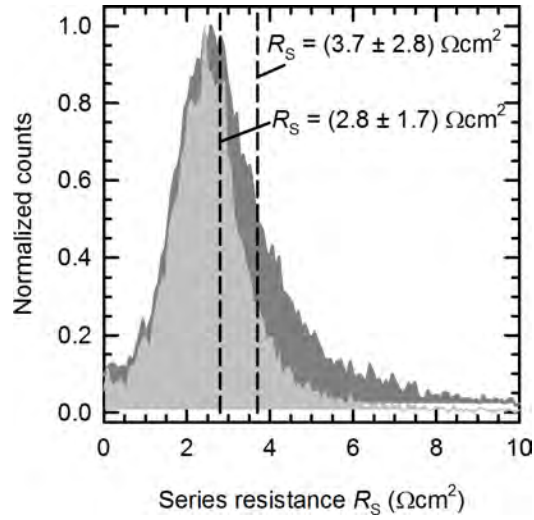


Figure 5.29: Histogram plot of the series resistance image of the total cell area.

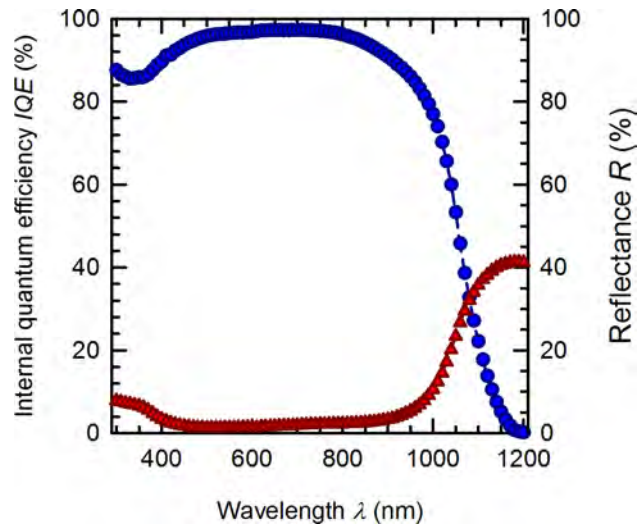


Figure 5.30: In-house measured internal quantum efficiency IQE (blue circles) and hemispherical reflectance R (red triangles) of the MacEpi cell. Figure from Ref. [Ern13a].

of Si. However, the measured average thickness of the epitaxial layer is $d_{av} = (0.4 \pm 0.1) \mu\text{m}$. Furthermore, the epitaxial layer on the pore walls is thicker at the bottom region. A turbulent gas flow could cause this discrepancy in the epitaxial layer thickness [Bri11] at the rear side. Brinkmann et al. also observe a “hour glass”-shaped epitaxial growth in via holes with diameters of few hundred μm . An alternative explanation is that most of the Si adatoms arrive at the outer surface and then diffuse into the pores where less adatoms arrive.

Carrier lifetime

The measured effective carrier lifetime $\tau_{\text{eff}} = (12.8 \pm 1.3) \mu\text{s}$ of a fully passivated MacEpi layer corresponds to an open-circuit voltage potential of

$$V_{\text{OC}} = \frac{kT}{q} \ln \left(\frac{J_{\text{SC}}}{J_0} - 1 \right) = (619 \pm 5) \text{ mV} \quad (5.8)$$

with $kT/q = 25.68 \text{ mV}$ at 298 K, $J_0 = (12.6 \pm 2.4) \times 10^{-13} \text{ A cm}^{-2}$, and $J_{\text{SC}} = 37.1 \text{ mA cm}^{-2}$.

However, the measured open-circuit voltage is only 544 mV. From the slope of the dark J - V and the J_{SC} - V_{OC} curve in the voltage range of 100 mV to 600 mV a local ideality factor n in the range from 2 to 3.5 is derived. The ideality factor at the maximum power point is $n = 2.5$. The high ideality factor indicates that the recombination current is essentially due to recombination that is located at the edges of the space charge region (SCR) [Edm96, Bre06]. The porous surface enhances the SCR edge length to $l = 104 \mu\text{m}$ for the $A = 3.92 \text{ cm}^2$ -sized cell. This corresponds to an enlargement factor of 1300.

The dark and illuminated J - V curves and the J_{SC} - V_{OC} curve are consistently fitted with a two-diode model [Sah57] with the voltage independent ideality factors $n_1 = 1$ and $n_2 = 2.8$. Figure 5.26b shows a semi-logarithmic plot of the dark and illuminated J - V curve and the J_{SC} - V_{OC} characteristics. The solid lines are the fitted curves for the fit parameters listed in the figure.

The previously determined values of $R_{\text{shunt}} = 6.7 \times 10^3 \Omega \text{ cm}^2$, $R_{\text{S}} = 2.3 \Omega \text{ cm}^2$, and $J_{\text{SC}} = 37.1 \text{ mA cm}^{-2}$ are used for the fits. The only free parameters of the fit are $J_{01} = 12 \times 10^{-12} \text{ A cm}^{-2}$ and $J_{02} = 3.5 \times 10^{-6} \text{ A cm}^{-2}$.

The SCR recombination current density per edge length is $J_{02,\text{edge}} = J_{02}A/l = 1.3 \times 10^{-9} \text{ A cm}^{-1}$. This $J_{02,\text{edge}}$ value corresponds to a surface recombination velocity of $8 \times 10^5 \text{ cm s}^{-1}$ as determined by Kühn et al. [Küh00]. Thus, the results are consistent with Kühn et al. only if the sample had no surface passivation at the edge of the SCR. This is possibly the case at the intersection of the SiO_x and SiN_x layers at the pore openings.

Series resistance

A candidate for the high series resistance of $2.3 \Omega \text{ cm}^2$ is the conductive glue. However, the comparison of the glued reference cell with the non-glued reference cell shows that the conductive glue accounts only for $0.3 \Omega \text{ cm}^2$.

Another possible source of the series resistance is the reduced area fraction of the P-diffused front surface region compared to a non-porous surface. The pore openings at the front side consume a large fraction of the front surface. The oxide layer covers the pore walls almost to the top. This oxide layer is visible as brighter region at the pore walls in Fig. 5.18a. Hence, the total diffused area at the front side is reduced for the MacEpi samples.

Figure 5.31 shows a SEM micrograph of the front side of the MacEpi cell. The P-diffused region is marked in red and has an effective line width of $d_{\text{line}} = 2 \mu\text{m}$ to $3 \mu\text{m}$ and a length of $l_{\text{line}} = 6.6 \mu\text{m}$. Since the Al fingers are parallel to the vertical image border as determined from SEM micrographs the current has to flow from left to the right through the P-diffused region as depicted in Fig. 5.31. Therefore, the effective sheet resistance $R_{\text{sheet,eff}}$ is calculated in the quadratic unit cell with a resistance network sketched in the figure.

The length of the conducting regions R_2 is $l_{\text{line}} = 6.6 \mu\text{m}$ and $l_{\text{line}}/2$ for the R_1 regions. Only half of the conductive areas lie within the unit cell area. This reduces the effective line width to $d_{\text{line}}/2 = 1 \mu\text{m}$ to $1.5 \mu\text{m}$. The resistances R_1 and R_2 are then calculated by $R_1 = R_{\text{sheet}} \times l_{\text{line}}/d_{\text{line}}$ and $R_2 = 2R_1$ with the nominal sheet resistance $R_{\text{sheet}} = 60 \Omega$ of the phosphorus diffusion. The resulting effective sheet resistance is then calculated to $R_{\text{sheet,eff}} = 230 \Omega$ to 460Ω which is a factor 3.9 to 7.7 larger than the nominal sheet resistance. Thus, the front surface region accounts for

$$R_{S,\text{front}} = \frac{1}{3} b^2 R_{\text{sheet,eff}} = 0.77 \Omega \text{ cm}^2 \text{ to } 1.54 \Omega \text{ cm}^2 \quad (5.9)$$

with $2b = 2 \text{ mm}$ the spacing between the front side fingers.

Further contributions to the series resistance are estimated by the equations given in Ref. [Mei84]. Therefore, a typical specific contact resistance of $1 \text{ m}\Omega \text{ cm}^2$ for the evaporated Al fingers [Mad12] and the specific bulk resistivity $2.65 \times 10^{-6} \Omega \text{ cm}$ of Al is used. Table 5.5

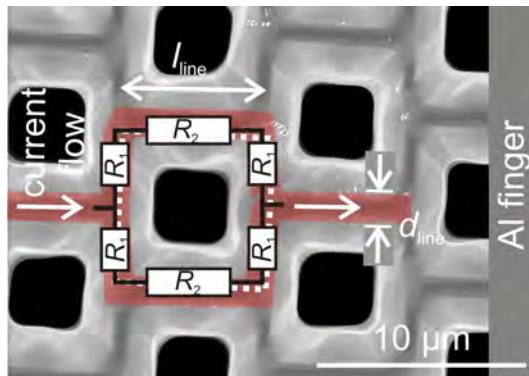


Figure 5.31: Top-view SEM micrograph of the surface of a detached macroporous Si layer after the epitaxy. The red region marks the P-diffused region. Figure from Ref. [Ern13a].

Table 5.5: Estimated series resistance contributions

Source of loss	Reference cell	MacEpi cell
Diffused front side ($\Omega \text{ cm}^2$)	0.20	0.77 to 1.54
Epitaxial emitter rear side ($\Omega \text{ cm}^2$)	0.12	0.18
Grid fingers (front and rear side) ($\Omega \text{ cm}^2$)	0.12	0.12
Bus bar ($\Omega \text{ cm}^2$)	0.04	0.04
Contact interface (front and rear side) ($\Omega \text{ cm}^2$)	0.04	0.11 to 0.16
Base ($\Omega \text{ cm}^2$)	0.05	0.01
Conductive glue (from experiment) ($\Omega \text{ cm}^2$)	0.3	0.3
Total ($\Omega \text{ cm}^2$)	0.9	1.5 to 2.4
Total (measurement) ($\Omega \text{ cm}^2$)	0.8	2.3

lists all the contributions to the series resistance of the planar reference sample and the MacEpi cell.

The total resistance of $0.9 \Omega \text{ cm}^2$ calculated for the reference cell agrees with the measured value of $0.8 \Omega \text{ cm}^2$. For the MacEpi cell the measured value is $2.3 \Omega \text{ cm}^2$ and agrees with the calculated value of $1.5 \Omega \text{ cm}^2$ to $2.4 \Omega \text{ cm}^2$. The estimation shows that the geometry at the front side diffusion causes about 50% of the series resistance.

5.5 MacPSi solar cells with ion implanted emitter

The third macroporous Si solar cell concept developed in this work uses ion implantation to selectively dope the outer surfaces of a macroporous Si layer. Thus, no masking of the surface is required for doping. Part of this work is published in Ref. [Ern13c]. In the further description these type of solar cells are termed “MacImplant solar cells”.

5.5.1 Sample preparation

Macroporous Si samples are prepared by the etching procedure described in Chapter 1.

Subsequent to the etching of the pores, the macroporous Si absorber layer is detached from the substrate. Then, the area of the macroporous layer is reduced to $60 \text{ mm} \times 60 \text{ mm}$ and subsequently laser-bonded to a silicon frame with four $20 \text{ mm} \times 20 \text{ mm}$ -sized openings (compare Section 5.1) to ease handling of the thin film. The four openings are quadratically arranged with a center-to-center distance of 25 mm. The side that was facing the substrate prior to detachment becomes the front side of the solar cell.

First, the samples are cleaned with an RCA-cleaning procedure. The implantation process is sketched in Figure 5.32. The implantation is performed under an angle of 25° of the ion beam with respect to the surface normal to avoid penetration of the ions through the open pores. First, boron ions from a boron trifluoride (BF_3) source are implanted into

the front side of the macroporous Si layer. The acceleration energy is 20 keV and the dose is $1.5 \times 10^{15} \text{ cm}^{-2}$.

Then, the macroporous layer turned upside down and rotated by 180° for the phosphorus implantation. The phosphorus ions from a phosphine (PH_3) source are accelerated with an energy of 20 keV at a dose of $2.0 \times 10^{15} \text{ cm}^{-2}$.

Finally, the samples are annealed in an oxygen atmosphere at temperatures $T \geq 1000^\circ\text{C}$ for dopant activation and diffusion. This creates a 20 nm thick oxide layer. Afterwards the supporting wafer with four samples is separated by a laser into $25 \text{ mm} \times 25 \text{ mm}$ -sized macroporous Si layers with an accessible area of $20 \text{ mm} \times 20 \text{ mm}$.

5.5.2 Structural analysis

Figure 5.33a shows a cross section SEM micrograph of a $(34 \pm 2) \mu\text{m}$ -thick macroporous Si cell with implanted emitter (MacImplant). Electrochemical etching of the separation layer creates a surface texture at the front side. The pore diameter is $2r_p = (4.3 \pm 0.2) \mu\text{m}$. Thus, the porosity is $p = (26.2 \pm 2.4) \mu\text{m}$.

The dashed box in Fig. 5.33a marks the region where the position of the pn-junction of the macroporous Si cell is determined using electron beam induced current (EBIC) technique. Figure 5.33b shows an SEM micrograph of the front side overlaid by the EBIC-signal (red). A pn-junction at both sides of the pores is observed. In cross sections taken in a plane perpendicular to the SEM micrograph shown here the same result is observed. The measured depth of the B-implantation at the pore walls ranges from $12 \mu\text{m}$ to $16 \mu\text{m}$.

5.5.3 Doping profile

The doping concentration of the boron and phosphorus implanted regions is measured by ECV profiling on planar non-porous reference samples. Figure 5.34 shows the concentration

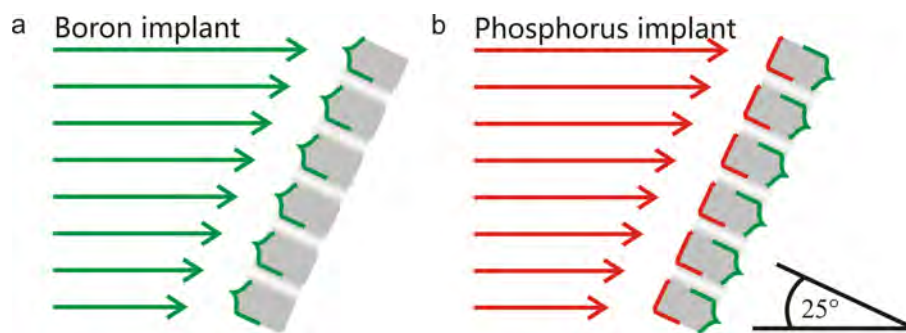


Figure 5.32: Illustration of the implantation of (a) the boron emitter at the front side, and (b) the phosphorus region at the rear side under an angle of 25° to the surface normal. Figures from Ref. [Ern13c].

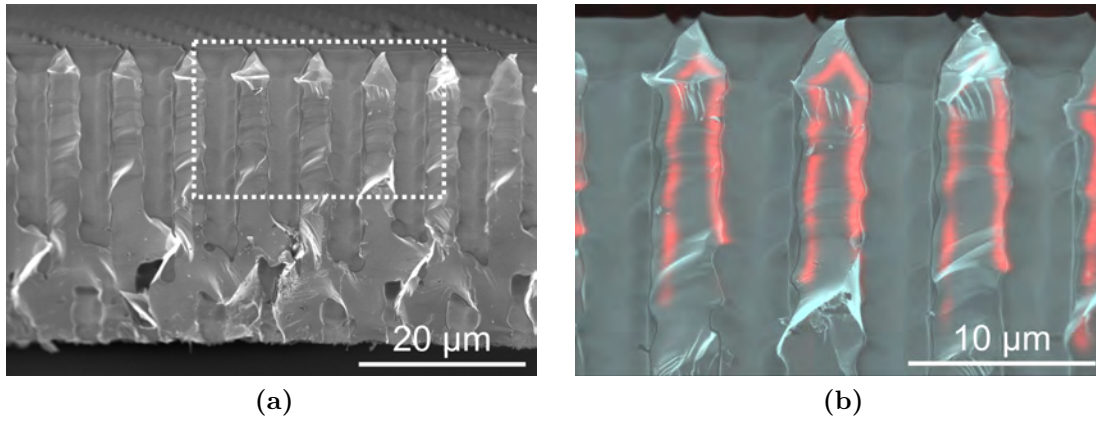


Figure 5.33: (a) Cross sectional SEM micrograph of a (34 ± 2) μm -thick macroporous Si solar cell. (b) Detailed EBIC (red) and SEM micrograph of the pn-junction at the front side. Figures from Ref. [Ern13c].

profile for the phosphorus region (red circles) and the boron emitter (green triangles). The peak concentration is $5 \times 10^{19} \text{ cm}^{-3}$ for the phosphorus doped region and $2 \times 10^{19} \text{ cm}^{-3}$ for the boron doped region. The depth is $1.0 \mu\text{m}$ for the phosphorus doped region and $0.9 \mu\text{m}$ for the boron doped region.

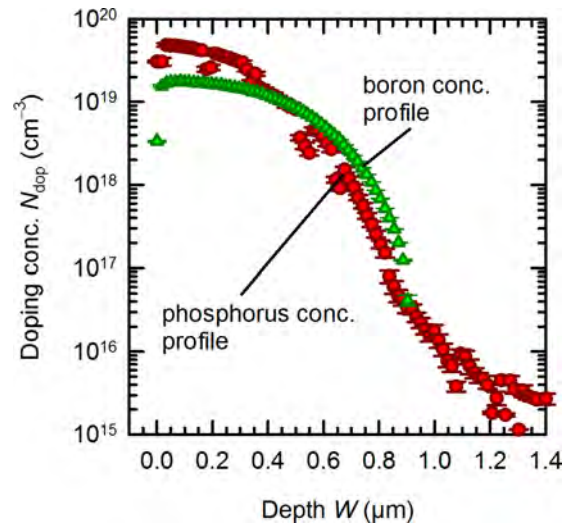


Figure 5.34: Doping concentration profile of the phosphorous (red circles) and boron (green triangles) implanted region measured on a planar reference sample after annealing. Figure from Ref. [Ern13c].

The sheet resistance is measured by a 4-point probe measurement and is $(45 \pm 2) \Omega$ for the phosphorus doped region and $(36 \pm 2) \Omega$ for the boron emitter.

5.5.4 Solar cell preparation

Figure 5.35 sketches the solar cell. The boron emitter is at the front side and at the upper section of the pore walls. The phosphorus doped region is at the rear side and at the bottom region of the pores.

Directly after laser-cutting into $25 \text{ mm} \times 25 \text{ mm}$ -sized samples the macroporous Si layers are RCA-cleaned. The oxide layer from the previous annealing step is removed from a 5 wt% HF-solution. A 70 nm thick SiN_x film with a refractive index of 1.9 is deposited onto the front and rear side of the sample.

The samples are RCA-cleaned and a 80 nm thick oxide layer is grown in a wet thermal oxidization at 900°C . After a dip in a 1 wt% HF-solution for 1 min the SiN_x film is removed in 85 wt% ortho-phosphoric acid at 140°C for 45 min. The removal process is finished with a dip in an 1 wt% HF-solution for 10 s.

An RCA-cleaning with the HF-dips shortened to each 10 s is followed by two cycles of PA-ALD of AlO_x to generate a thin tunneling layer on the front side [vH07]. This layer prohibits a diffusion of the front contact aluminum through the front diffusion.

The Al front side fingers are evaporated through a shadow mask with an angle of 55° to the surface normal to avoid penetration of Al into the pores. The spacing between the fingers is 2 mm and the width of the Al fingers is $110 \mu\text{m}$.

Then, a SiN_x double layer is deposited for front surface passivation and anti-reflection coating. The double layer consists of a 10 nm layer with a refractive index of $n = 2.4$ and a 100 nm layer with a refractive index of $n = 2.05$ as measured on planar reference samples.

Subsequently, the rear-side grid is evaporated at interdigitated positions relative to the front-side grid (see Fig. 5.35) with an angle of 55° to the surface normal. Then, the

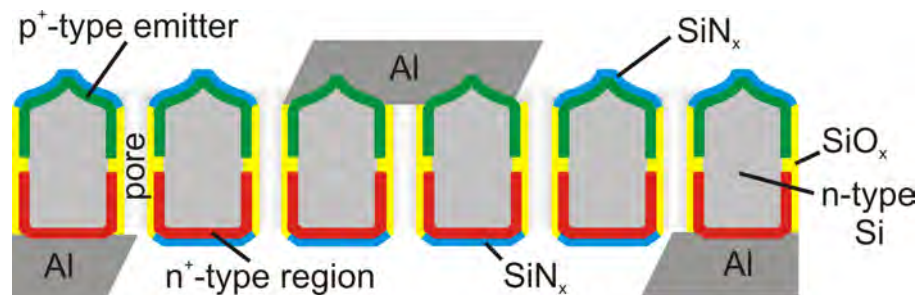


Figure 5.35: Schematics of the macroporous solar cell (*not to scale*). The p^+ -type implanted emitter (green) is at the front side. An n^+ -type implanted region (red) is at the rear side. A SiN_x layer (blue) is on the front and on the rear side. A SiO_x layer (yellow) is on the pore walls. Figure from Ref. [Ern13c].

Si handling frame is removed and the cell area is defined to 3.92 cm^2 . The interface is improved by annealing the samples in air on a hot plate at $350 \text{ }^\circ\text{C}$ for 2 min.

Mechanical support of the thin MacImplant cells is provided by laser-bonding of the thin films to an Al coated glass carrier to provide a good electrical contact and mechanical stability for device characterization. The so called AMELI-process is described in Ref. [SH12]. Aligning of the $38 \text{ }\mu\text{m}$ -sized laser-welding spots to the centre of the $110 \text{ }\mu\text{m}$ -wide Al fingers is enabled by the openings in the border area of the Al coating on the glass. Finally, the samples are annealed in air on a hot plate at $425 \text{ }^\circ\text{C}$ for 3 min. Figure 5.36a shows the front side of a MacImplant solar cell bonded to a glass carrier. The Al coating on the glass has a width of 13 mm. Figure 5.36b shows the rear side of the interconnected cell. The red dots illustrate the positions of the laser-welding spots.

Planar, non-porous reference samples are processed along with the MacImplant samples. The reference samples are from an identical substrate wafer and receive the same p-type implantation at the front side and the same n-type implantation at the rear side.

5.5.5 Cell results

The illuminated J - V curves are measured at a temperature of $25 \text{ }^\circ\text{C}$ under illumination by halogen lamps in a home built cell tester. The lamp to cell distance is adjusted to reproduce the short-circuit current density of a cell that was calibrated at Fraunhofer ISE CalLab under 0.1 W cm^{-2} of AM1.5g-illumination. The external quantum efficiency is measured under one sun bias light and a spectral mismatch correction is applied [Kin91].

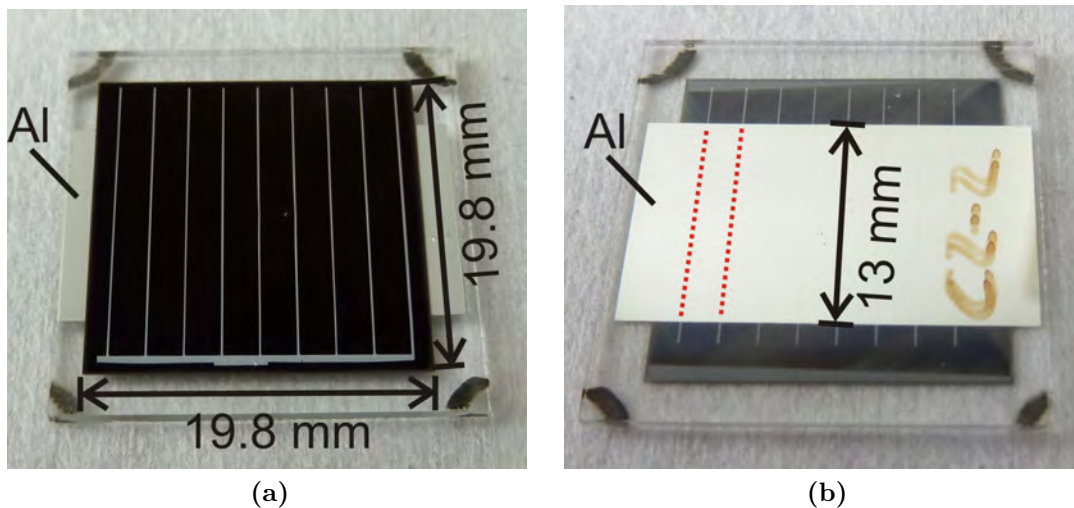


Figure 5.36: MacImplant cell bonded to an Al coated glass carrier. (a) Front side of the solar cell. (b) Rear side of the cell. The red dots illustrate the positions of the laser-welding spots. Figures from Ref. [Ern13c].

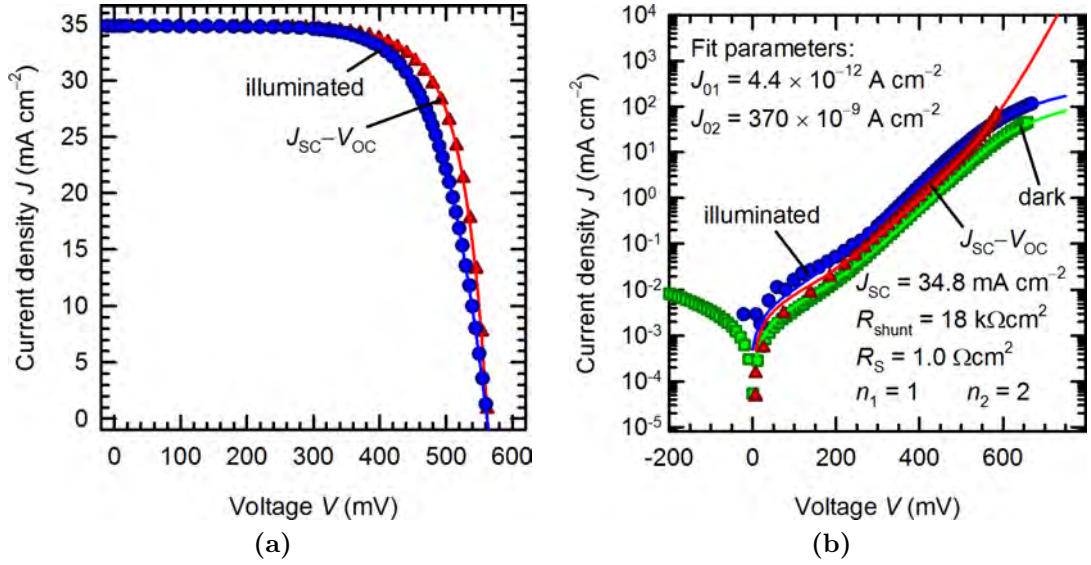


Figure 5.37: (a) In-house measured illuminated J - V curve (blue circles) and J_{SC} - V_{OC} curve (red triangles) of the MacImplant cell. The solid blue and red lines are fits from a two-diode model for the parameters shown in Fig. 5.37b. (b) Illuminated J - V curve (blue circles), dark J - V curve (green boxes), and J_{SC} - V_{OC} curve (red triangles) of the MacImplant cell. The solid blue, green, and red lines are fits from a two-diode model for the parameters given in the figure. Figures from Ref. [Ern13c].

The cells are illuminated through a 15 mm \times 15 mm-sized mask to exclude edge regions. The planar reference cells are illuminated through a mask with the size of 4.25 cm².

Figure 5.37a shows the J - V curve of the best out of three MacImplant cells. The best cell achieves an open-circuit voltage of 562 mV and a short-circuit current density of 34.8 mA cm⁻². With a fill factor $FF = 69.1\%$ the cell achieves an energy-conversion efficiency of $\eta = 13.5\%$.

Table 5.6 lists the measured parameters for the MacImplant cells and planar reference cells. The lumped parallel resistance $R_{shunt} = 18 \times 10^3 \Omega \text{ cm}^2$ of the best MacImplant cell is determined from the dark J - V curve at -0.5 V by Ohm's law. The lumped series resistance $R_s = 1.0 \Omega \text{ cm}^2$ is determined using the fill factor method [Gre98].

The dark and illuminated J - V curves and the J_{SC} - V_{OC} characteristics are simultaneously fitted with a two-diode model [Sah57] with the voltage independent ideality factors 1 and 2. Figure 5.37b shows a semilogarithmic plot of the dark and illuminated J - V curves (green boxes and blue circles) and the J_{SC} - V_{OC} curve (red triangles).

For the fits (solid lines in the graph), the previously determined values of $R_{shunt} = 18 \times 10^3 \Omega \text{ cm}^2$, $R_s = 1.0 \Omega \text{ cm}^2$, and $J_{SC} = 34.8 \text{ mA cm}^{-2}$ are used. The only fitted parameters are $J_{01} = 4.4 \times 10^{-12} \text{ A cm}^{-2}$ and $J_{02} = 370 \times 10^{-9} \text{ A cm}^{-2}$.

Table 5.6: Electrical solar cell results of the implanted solar cells.

Sample	A (cm ²)	J_{SC} (mA cm ⁻²)	V_{OC} (mV)	FF (%)	pFF (%)	η (%)
Best	3.92 ^A	33.0	581	63.0	75.3	12.1
Mean ^B	3.92 ^A	32.3 ± 0.7	566 ± 28	62.7 ± 2.2	75.2 ± 0.4	11.5 ± 0.6
Best	2.25 ^C	34.8	562	69.1	73.7	13.5
Mean ^B	2.25 ^C	34.4 ± 0.5	550 ± 25	68.8 ± 1.8	73.9 ± 0.5	13.0 ± 0.5
Planar ref.	4.25 ^C	31.3	623	77.4	80.0	15.1
Mean ^D	4.25 ^C	31.2 ± 0.1	624 ± 1	77.5 ± 0.1	79.9 ± 0.1	15.0 ± 0.1

^A Illuminated area is cell area.

^B Average cell parameters of three MacImplant cells.

^C Illuminated area is aperture area.

^D Average cell parameters of three planar reference cells.

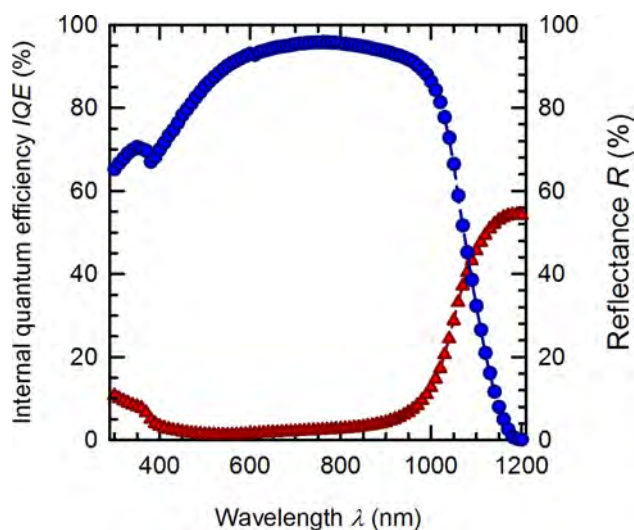


Figure 5.38: In-house measured internal quantum efficiency IQE (blue circles) and hemispherical reflectance R (red triangles) of the MacImplant cell. Figure from Ref. [Ern13c].

Figure 5.38 shows the in-house measured internal quantum efficiency IQE and reflectance R of the best MacImplant cell. The cell has a low reflectance of $\leq 5\%$ for wavelengths ranging from 380 nm to 920 nm. However, the internal quantum efficiency is $< 90\%$ for wavelengths < 570 nm. The strong losses are most likely caused by free-carrier absorption in the highly boron doped region at the front side.

5.5.6 Discussion

The low open-circuit voltages of the MacImplant cells and of the planar reference cells is supposed to come from poorly passivated boron emitter by silicon nitride films [Ker02, Che06]. In Ref. [Che06], the SiN_x passivation limited the implied open-circuit voltages for boron emitters with sheet resistances $< 50 \Omega$ to values around 620 mV. Therefore, the SiN_x front side passivation of this work only acts as anti-reflection coating. Future improvements of the MacImplant solar cells will therefore have to optimize the front side passivation.

In Fig. 5.33b a boron implanted region on both sides of the pores is observed. Reflection of boron ions at the pore walls may cause this effect, since the ions are impinging under an angle of 65° with respect to the surface normal of the pore walls.

The fraction of backscattered ions as a function of the angle of incidence of the ion beam on a planar surface is calculated using Iradina 1.0.4 [Bor11]. Iradina is a software for simulating ion beam irradiation of three-dimensional target geometries. Figure 5.39 shows the fraction of the backscattered ions for the boron ions (green triangles) and phosphorus ions (red circles) as a function of the angle of incidence. The fraction of the backscattered ions is lower for the phosphorus ions due to their higher atomic mass. The simulations show that 20.4% of the boron ions and 14.5% of the phosphorus ions are reflected at a planar silicon surface under an angle of incidence of 65° and an acceleration energy of 20 keV.

Iradina allows also the simulation of ion beam irradiation on three-dimensional targets [Bor11]. In order to understand the reflection in the pore walls, a three-dimensional

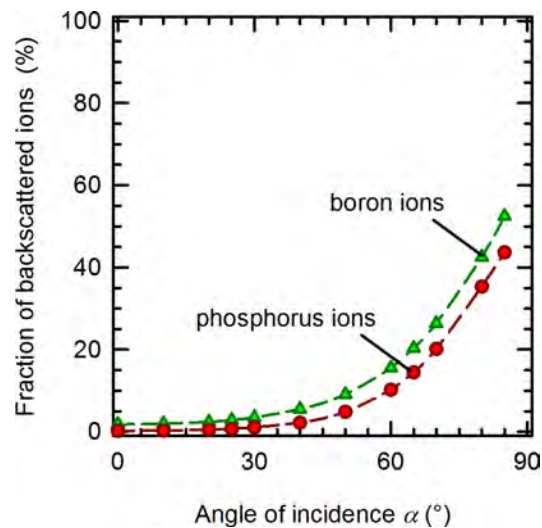


Figure 5.39: Fraction of backscattered ions as a function of the angle of incidence α of the ion beam for boron (green triangles) and phosphorus (red circles). The dashed lines are to guide the eye. Figure from Ref. [Ern13c].

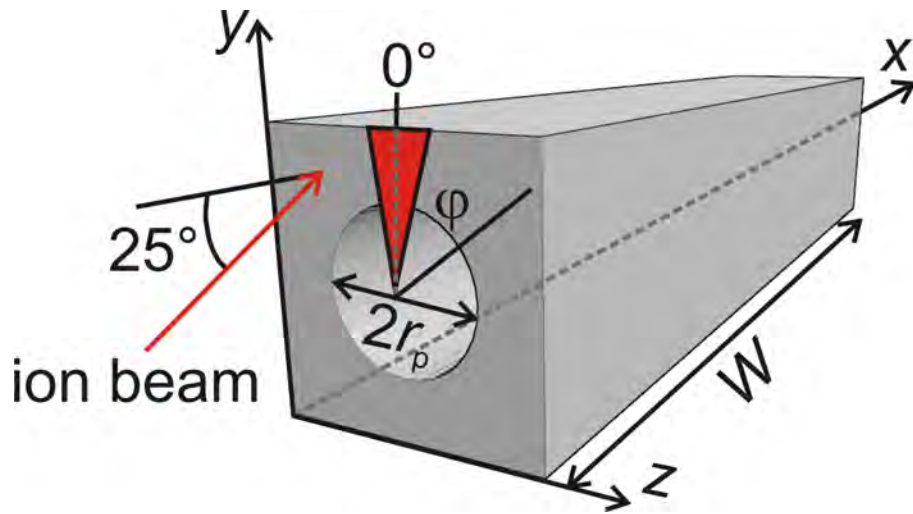


Figure 5.40: Illustration of the three-dimensional pore target in Iradina. The ion beam has an inclination angle of 25° to the surface normal. Figure from Ref. [Ern13c].

Si target with a macropore in the center is defined. Figure 5.40 shows this geometry. The pore diameter is $2r_p = 4.3 \mu\text{m}$ and the thickness of the unit cell is $W = 30 \mu\text{m}$. The ion beam enters the yz -plane with an inclination angle of 25° to the surface normal. The position of the ion beam is randomly distributed over this plane.

In order to illustrate the distribution of the implanted ions in the pore wall, the Cartesian coordinate system is transformed into the cylindrical coordinate system with radius r and polar angle φ . Then, the implanted ions are integrated over circular sectors with an angle $\Delta\varphi = 10^\circ$ as a function of the pore depth x . The red region in Fig. 5.40 illustrates such a circular sector.

Figure 5.41 shows the implanted ions as a function of the polar angle φ and the pore depth x . The red area in the upper center is the region where the ion beam directly hits the pore wall. This region reaches approximately $9 \mu\text{m}$ deep into the pores. The orange and green areas at the shady side are the regions where the ion beam hits the pore wall mainly from the first reflection and reaches approximately $18 \mu\text{m}$ deep into the pores. Multiple reflections for few ions cause a weak implantation even deeper in the pores (blue region).

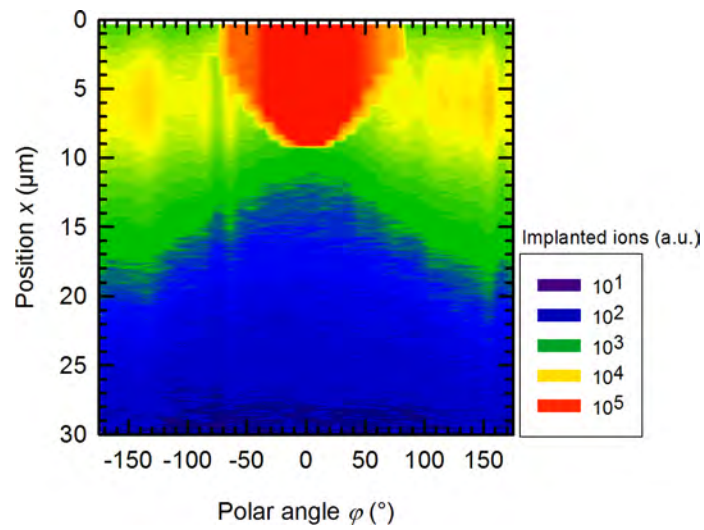


Figure 5.41: Implanted ions as a function of polar angle φ and pore depth x . Figure from Ref. [Ern13c].

6 | Summary

In this work, macroporous Si was investigated as new thin-film absorber material for crystalline Si solar cells. Therefore, an electrochemical etching process was developed.

Fabrication and separation of 133 cm^2 -sized and $(29 \pm 2) \mu\text{m}$ -thick macroporous Si layers from $(305 \pm 20) \mu\text{m}$ -thick n-type crystalline Si substrate wafers was demonstrated in this work for the first time. The typical porosity of the macroporous Si absorber layers fabricated in this work is $p = 30\%$. The separation layer of the macroporous Si layers produced with the large area etching setup is a cavity with a porosity of $p = 100\%$.

This work also demonstrates highly controllable pore growth on a small area etching setup with an etched area of 1 cm^2 . By varying the etching current density when etching the highly porous separation layer, the width of weak bridges that remain as connection between the macroporous layer and the substrate can be precisely controlled. The width of the weak bridges varies in the range from 0 nm to 800 nm for the layers produced with the small area etching setup.

A three-dimensional numerical model was developed to describe measured effective carrier lifetimes of surface passivated macroporous Si layers with non-passivated regions at the positions of the weak bridges. The numerical model accounts for these non-passivated regions. The numerical model is experimentally verified with surface passivated macroporous Si samples with varied percentage of the non-passivated areas in the range from $\Psi = 0\%$ to 1.6% . The effective carrier lifetime of a fully passivated sample ($\Psi = 0\%$) is $\tau_{\text{eff}} = (10.1 \pm 0.5) \mu\text{s}$.

The optical reflectance of a $(34 \pm 2) \mu\text{m}$ -thick macroporous Si layer with hexagonally arranged pores and a $(35 \pm 2) \mu\text{m}$ -thick layer with randomly arranged pores was measured with six diffuse back reflectors and a dark room behind the samples. An analytical model describes the measured total reflectance curves of each sample simultaneously for the seven measurements with only one fit parameter. The optical model yields the optical absorption of the macroporous Si samples. The macroporous Si layer with randomly distributed pores allows for a short-circuit current density of $J_{\text{SC}}^* = (40.82 \pm 0.36) \text{ mA cm}^{-2}$. This is close to the photogeneration current density of $J_{\text{SC}}^* = (41.43 \pm 0.37) \text{ mA cm}^{-2}$ that is calculated for a Lambertian light trapping scheme with an identical effective thickness. This sample achieves a fraction of 0.985 ± 0.012 of the Lambertian limit. The sample with hexagonally arranged pores achieves a fraction of 0.935 ± 0.003 of the Lambertian limit which is mainly due to the higher front surface reflectance compared to the sample with randomly arranged pores.

Surface passivation with Al_2O_3 of the optically characterized samples yielded an actual effective carrier lifetime of $\tau_{\text{eff}} = (28.6 \pm 2.9) \mu\text{s}$ for the sample with hexagonally arranged

pores and $\tau_{\text{eff}} = (25.7 \pm 2.6) \mu\text{s}$ for the sample with randomly arranged pores. Implied J - V curves of these samples were measured using a photoluminescence-based method. In this work, contactless transient microwave-detected photoconductance decay method is used to calibrate the photoluminescence signal for the first time. This new method experimentally determines the efficiency potential of macroporous Si. In case of the hexagonally arranged pores, the efficiency potential is $\eta = (20.2 \pm 0.4) \%$. The sample with randomly arranged pores yields an efficiency potential of $\eta = (21.5 \pm 0.4) \%$.

However, solar cell processing of such thin layers is challenging. Therefore, a handling process to mechanically support the fragile layers during processing in the laboratory was developed in this work. The process bonds the macroporous Si layers to a thick Si frame by means of laser-welding. Since no extraneous material is used in this process, the macroporous Si layers can be treated with any typical solar cell process, such as wet chemical RCA-cleaning, high-temperature furnace processes, and plasma-enhanced deposition processes.

A processing sequence for selectively passivating the inner pore walls was developed in this work. This process combines non-conformal and surface conformal deposition techniques. The low process pressure during plasma-enhanced chemical vapor deposition of SiN_x leads to a non-conformal deposition of a protecting layer on the outer surface of the macroporous Si layer. Thermal oxidization at atmospheric pressure on the contrary leads to a surface conformal deposition. Selective wet chemical etching in phosphoric acid then removes the protecting SiN_x layer and leaves a macroporous Si layer with surface passivated pore walls and accessible front and rear side.

In this work, three concepts for processing macroporous Si solar cells were developed and characterized. The first concept is based on a heterojunction with amorphous silicon. The best 3.92 cm^2 -sized macroporous heterojunction solar cell achieves an open-circuit voltage of 494 mV, a short-circuit current density of 21.3 mA cm^{-2} , and with a fill factor of 68.7% an energy-conversion efficiency of 7.2%.

The second approach uses epitaxial growth of p^+ -type silicon onto the n-type macroporous silicon for junction formation. The epitaxial layer has two functions. First, the layer acts as a p-type emitter and second, the epitaxial layer seals the rear side of the macroporous silicon absorber and thus eases device fabrication. The best solar cell of this type achieves an open-circuit voltage of 544 mV, a remarkably high short-circuit current density of 37.1 mA cm^{-2} , and with a fill factor of 65.1% an energy-conversion efficiency of 13.1%.

The third cell concept is based on the implantation of boron and phosphorus ions to create side-selective highly doped regions. The best solar cell of this type achieves an open-circuit voltage of 562 mV, a short-circuit current density of 34.8 mA cm^{-2} , and with a fill factor of 69.1% an energy-conversion efficiency of 13.5%.

Bibliography

- [Alt05] P. Altermatt; F. Geelhaar; T. Trupke; X. Dai; A. Neisser und E. Daub: Injection dependence of spontaneous radiative recombination in c-Si: experiment, theoretical analysis, and simulation, in: *5th International Conference on Numerical Simulation of Optoelectronic Devices*, S. 47–48
- [Aro80] N. D. Arora; S. G. Chamberlain und D. J. Roulston: Diffusion length determination in p-n junction diodes and solar cells. *Applied Physics Letters* (1980), Bd. 37(3): S. 325–327
- [Ave72] M. Aven; J. Z. Devine; R. B. Bolon und G. W. Ludwig: Scanning electron microscopy and cathodoluminescence of ZnSex Te1 – xp-n junctions. *Journal of Applied Physics* (1972), Bd. 43(10): S. 4136–4142
- [Bas93] P. Basore: Extended spectral analysis of internal quantum efficiency, in: *Proceedings of the 23rd IEEE Photovoltaic Specialists Conference*, IEEE, New York, S. 147–152
- [Blu74] W. Bludau; A. Onton und W. Heinke: Temperature dependence of the band gap of silicon. *Journal of Applied Physics* (1974), Bd. 45(4): S. 1846
- [Bor11] C. Borschel und C. Ronning: Ion beam irradiation of nanostructures – A 3D Monte Carlo simulation code. *Nuclear Instruments and Methods in Physics Research Section B: Beam Interactions with Materials and Atoms* (2011), Bd. 269(19): S. 2133–2138
- [Bre95] R. Brendel: Note on the interpretation of injection-level-dependent surface recombination velocities. *Applied Physics A Materials Science & Processing* (1995), Bd. 60(5): S. 523–524
- [Bre97] R. Brendel: A novel process for ultrathin monocrystalline silicon solar cells on glass, in: *14th European Photovoltaic Solar Energy Conference*, H.S. Stephens & Associates, Bedford (1997), S. 1354–1357
- [Bre99] R. Brendel und D. Scholten: Modeling light trapping and electronic transport of waffle-shaped crystalline thin-film Si solar cells. *Applied Physics A: Materials Science & Processing* (1999), Bd. 69(2): S. 201–213
- [Bre06] O. Breitenstein; P. Altermatt; K. Ramspeck; M. Green; J. Zhao und A. Schenk: Interpretation of the Commonly Observed I-V Characteristics of C-SI Cells Having Ideality Factor Larger Than Two, in: *2006 IEEE 4th World Conference on Photovoltaic Energy Conference*, IEEE, S. 879–884

- [Bri11] N. Brinkmann; D. Pócza; E. J. Mitchell und S. Reber: 3D epitaxial growth through holes for the fabrication of thin-film solar cells. *Journal of Crystal Growth* (2011), Bd. 335(1): S. 37–41
- [Cam87] P. Campbell und M. A. Green: Light trapping properties of pyramidally textured surfaces. *Journal of Applied Physics* (1987), Bd. 62(1): S. 243
- [Cam90] P. Campbell: Light trapping in textured solar cells. *Solar Energy Materials* (1990), Bd. 21(2-3): S. 165–172
- [Cam93] P. Campbell: Enhancement of light absorption from randomizing and geometric textures. *Journal of the Optical Society of America B* (1993), Bd. 10(12): S. 2410
- [Che06] F. W. Chen; T.-T. A. Li und J. E. Cotter: Passivation of boron emitters on n-type silicon by plasma-enhanced chemical vapor deposited silicon nitride. *Applied Physics Letters* (2006), Bd. 88(26): S. 263514
- [COM12] COMSOL Multiphysics (2012), URL <http://www.comsol.de>, [Online; accessed 3-October-2012]
- [Cue04] A. Cuevas und D. Macdonald: Measuring and interpreting the lifetime of silicon wafers. *Solar Energy* (2004), Bd. 76(1-3): S. 255–262
- [Dro07] F. Dross; J. Robbelein; B. Vandeveld; E. van Kerschaver; I. Gordon; G. Beaucarne und J. Poortmans: Stress-induced large-area lift-off of crystalline Si films. *Applied Physics A* (2007), Bd. 89(1): S. 149–152
- [Edm96] S. A. Edmiston; G. Heiser; A. B. Sproul und M. A. Green: Improved modeling of grain boundary recombination in bulk and p-n junction regions of polycrystalline silicon solar cells. *Journal of Applied Physics* (1996), Bd. 80(12): S. 6783
- [Ern10] M. Ernst und R. Brendel: Large area macroporous silicon layers for monocrystalline thin-film solar cells, in: *35th IEEE Photovoltaic Specialists Conference (PVSC)*, IEEE, S. 003122–003124
- [Ern11] M. Ernst und R. Brendel: Modeling effective carrier lifetimes of passivated macroporous silicon layers. *Solar Energy Materials and Solar Cells* (2011), Bd. 95(4): S. 1197–1202
- [Ern12a] M. Ernst; R. Brendel; R. Ferré und N.-P. Harder: Thin macroporous silicon heterojunction solar cells. *physica status solidi (RRL) - Rapid Research Letters* (2012), Bd. 6(5): S. 187–189
- [Ern12b] M. Ernst; R. Brendel; R. Ferré; N.-P. Harder und S. Kajari-Schröder: Macroporous silicon as an absorber for thin heterojunction solar cells, in: *2012 38th IEEE Photovoltaic Specialists Conference*, IEEE, S. 001040–001045

- [Ern12c] M. Ernst; U. Zywietsch und R. Brendel: Point contact openings in surface passivated macroporous silicon layers. *Solar Energy Materials and Solar Cells* (2012), Bd. 105: S. 113–118
- [Ern13a] M. Ernst und R. Brendel: Macroporous Silicon Solar Cells With an Epitaxial Emitter. *IEEE Journal of Photovoltaics* (2013), Bd. 3(2): S. 723–729
- [Ern13b] M. Ernst und R. Brendel: Lambertian light trapping in thin monocrystalline macroporous Si layers. *physica status solidi (RRL) - Rapid Research Letters* (submitted, 2013)
- [Ern13c] M. Ernst; H. Schulte-Huxel; R. Niepelt; S. Kajari-Schröder und R. Brendel: Thin Crystalline Macroporous Silicon Solar Cells with Ion Implanted Emitter. *Energy Procedia* (2013), Bd. 38: S. 910–918
- [Gla10] M. Glatthaar; J. Haunschild; M. Kasemann; J. Giesecke; W. Warta und S. Rein: Spatially resolved determination of dark saturation current and series resistance of silicon solar cells. *physica status solidi (RRL) - Rapid Research Letters* (2010), Bd. 4(1-2): S. 13–15
- [Goe81] A. Goetzberger: Optical Confinement in Thin Si-Solar Cells by Diffuse Back Reflectors, in: *15th IEEE Photovoltaic Specialists Conference (PVSC)*, IEEE, Kissimmee and FL and USA, S. 867–870
- [Gre98] M. A. Green: *Solar cells: Operating Principles, Technology and System Applications*. Sydney and Australia: Univ. New South Wales (1998)
- [Gre08] M. A. Green: Self-consistent optical parameters of intrinsic silicon at 300 K including temperature coefficients. *Sol. Energy Mater. Sol. Cells* (2008), Bd. 92: S. 1305–1310
- [Gue95] C. A. Gueymard: SMARTS, A Simple Model of the Atmospheric Radiative Transfer of Sunshine: Algorithms and Performance Assessment: Professional Paper FSEC-PF-270-95, in: *Florida Solar Energy Center*, 1679 Clearlake Rd. and Cocoa and FL 32922
- [Gue01] C. A. Gueymard: Parameterized transmittance model for direct beam and circumsolar spectral irradiance. *Solar Energy* (2001), Bd. 71(5): S. 325–346
- [Hen09] F. Henley; S. Kang; Z. Liu; L. Tian; J. Wang und Y.-L. Chow: Beam-induced wafering technology for kerf-free thin PV manufacturing, in: *2009 34th IEEE Photovoltaic Specialists Conference (PVSC)*, IEEE, S. 001718–001723
- [Her13] S. Herlufsen: *Characterization of crystalline silicon based on measurements of the photoluminescence emission*, Dissertation, Leibniz Universität Hannover, Hannover (2013)
- [Hez89] R. Hezel und K. Jaeger: Low-Temperature Surface Passivation of Silicon for Solar Cells. *Journal of The Electrochemical Society* (1989), Bd. 136(2): S. 518

- [Hin11] D. Hinken; C. Schinke; S. Herlufsen; A. Schmidt; K. Bothe und R. Brendel: Experimental setup for camera-based measurements of electrically and optically stimulated luminescence of silicon solar cells and wafers. *Review of Scientific Instruments* (2011), Bd. 82(3): S. 033706
- [Hoe06] B. Hoex; S. B. S. Heil; E. Langereis; M. C. M. van de Sanden und W. M. M. Kessels: Ultralow surface recombination of c-Si substrates passivated by plasma-assisted atomic layer deposited Al₂O₃. *Applied Physics Letters* (2006), Bd. 89(4): S. 042112
- [Hoe07] B. Hoex; J. Schmidt; R. Bock; P. P. Altermatt; M. C. M. van de Sanden und W. M. M. Kessels: Excellent passivation of highly doped p-type Si surfaces by the negative-charge-dielectric Al₂O₃. *Applied Physics Letters* (2007), Bd. 91(11): S. 112107
- [Hoe12] B. Hoex; van de Sanden, M. C. M.; J. Schmidt; R. Brendel und W. M. M. Kessels: Surface passivation of phosphorus-diffused n⁺-type emitters by plasma-assisted atomic-layer deposited Al₂O₃. *physica status solidi (RRL) - Rapid Research Letters* (2012), Bd. 6(1): S. 4–6
- [Hol12] Z. C. Holman; A. Descoeudres; L. Barraud; F. Z. Fernandez; J. P. Seif; S. d. Wolf und C. Ballif: Current Losses at the Front of Silicon Heterojunction Solar Cells. *IEEE Journal of Photovoltaics* (2012), Bd. 2(1): S. 7–15
- [Hur02] P. Hurley; B. O’Sullivan; F. Cubaynes und P. Stolk: Examination of the Si(111)-SiO₂, Si(110)-SiO₂, and Si(100)-SiO₂ Interfacial Properties Following Rapid Thermal Annealing. *J. Electrochem. Soc* (2002), Bd. 149: S. G194–G197
- [Kan85] D. E. Kane und R. M. Swanson: Measurement of the emitter saturation current by a contactless photoconductivity decay method, in: *18th IEEE Photovoltaic Specialists Conference (PVSC)*, IEEE, S. 578–583
- [Ker70] W. Kern und D. Puotinen: Cleaning solutions based on hydrogen peroxide for use in silicon semiconductor. *RCA Review* (1970), Bd. 31: S. 187–206
- [Ker02] M. J. Kerr: *Surface, Emitter and Bulk Recombination in Silicon and Development of Silicon Nitride Passivated Solar Cells*, Dissertation, Australian National University, Canberra (2002), URL <https://digitalcollections.anu.edu.au/bitstream/1885/47459/5/01front.pdf>
- [Kes12] M. Kessler; T. Ohrdes; P. P. Altermatt und R. Brendel: The effect of sample edge recombination on the averaged injection-dependent carrier lifetime in silicon. *Journal of Applied Physics* (2012), Bd. 111(5): S. 054508
- [Kin91] D. King und B. Hansen: A sensitivity analysis of the spectral mismatch correction procedure using wavelength-dependent error sources (solar cell testing), in: *The Conference Record of the Twenty-Second IEEE Photovoltaic Specialists Conference - 1991*, IEEE, S. 459–465

- [Küh00] R. Kühn; P. Fath und E. Bucher: Effects of pn-junctions bordering on surfaces investigated by means of 2D-modeling, in: *Photovoltaic Specialists Conference, 2000. Conference Record of the Twenty-Eighth IEEE*, S. 116–119, URL <http://ieeexplore.ieee.org/stamp/stamp.jsp?arnumber=915768>
- [Kun86] M. Kunst und G. Beck: The study of charge carrier kinetics in semiconductors by microwave conductivity measurements. *J. Appl. Phys* (1986), Bd. 60: S. 3558–3566
- [Leh90] V. Lehmann und H. Föll: Formation Mechanism and Properties of Electrochemically Etched Trenches in n-Type Silicon. *J. Electrochem. Soc* (1990), Bd. 137(2): S. 653–659
- [Leh91] V. Lehmann und U. Gösele: Porous silicon formation: A quantum wire effect. *Appl. Phys. Lett* (1991), Bd. 58: S. 856–858
- [Leh92] V. Lehmann; W. Hönlein; R. Stengl; J. Willer und H. Wendt: Verfahren zur Herstellung einer Solarzelle aus einer Substratscheibe (1992)
- [Leh93] V. Lehmann: The Physics of Macropore Formation in Low Doped n-Type Silicon. *J. Electrochem. Soc* (1993), Bd. 140: S. 2836–2843
- [Leh97] V. Lehmann und U. Grüning: The limits of macropore array fabrication. *Thin Solid Films* (1997), Bd. 297: S. 13–17
- [Leh98] V. Lehmann: Macroporous silicon: Physics and applications, in: R. Helbig (Herausgeber) *Advances in Solid State Physics 37*, Bd. 37 von *Advances in Solid State Physics*, Springer Berlin Heidelberg, Berlin and Heidelberg (1998), S. 15–23
- [Luk87] K. L. Luke und L.-J. Cheng: Analysis of the interaction of a laser pulse with a silicon wafer: Determination of bulk lifetime and surface recombination velocity. *J. Appl. Phys* (1987), Bd. 61: S. 2282
- [Luq89] A. Luque: *Solar Cells and Optics for Photovoltaic Concentration*. Adam Hilger, Bristol (1989)
- [Mac58] G. Macfarlane; T. McLean; J. Quarrington und V. Roberts: Fine Structure in the Absorption-Edge Spectrum of Si. *Physical Review* (1958), Bd. 111(5): S. 1245–1254
- [Mäc03] H. Mäckel und A. Cuevas: Determination of the surface recombination velocity of unpassivated silicon from spectral photoconductance measurements, in: K. Kurokawa (Herausgeber) *Proceedings of the 3rd World Conference on Photovoltaic Energy Conversion*, Bd. 1, Osaka (2003), S. 71–74
- [Mad12] C. Mader; J. Müller; S. Eideloth und R. Brendel: Local rear contacts to silicon solar cells by in-line high-rate evaporation of aluminum. *Solar Energy Materials and Solar Cells* (2012), Bd. 107: S. 272–282

- [Mei84] D. Meier und D. Schroder: Contact resistance: Its measurement and relative importance to power loss in a solar cell. *IEEE Transactions on Electron Devices* (1984), Bd. 31(5): S. 647–653, URL <http://ieeexplore.ieee.org/stamp/stamp.jsp?arnumber=1483869>
- [Mis93] K. Misiakos und D. Tsamakis: Accurate measurements of the silicon intrinsic carrier density from 78 to 340 K. *Journal of Applied Physics* (1993), Bd. 74(5): S. 3293
- [Mos12] M. M. Moslehi; P. Kapur; J. Kramer; V. Rana; S. Seutter; A. Deshpande; T. Stalcup; S. Kommera; J. Ashjaee; A. Calcaterra; D. Grupp; D. Dutton und R. Brown: Worldrecord 20.6% efficiency 156mm x 156mm full-square solar cells using low-cost kerfless ultrathin epitaxial silicon and porous silicon lift-off technology for industryleading high-performance smart PV modules, in: *PV Asia Pacific (APVIA/PVAP) Expo*, Singapore (2012)
- [Pow12] D. M. Powell; M. T. Winkler; H. J. Choi; C. B. Simmons; D. B. Needleman und T. Buonassisi: Crystalline silicon photovoltaics: a cost analysis framework for determining technology pathways to reach baseload electricity costs. *Energy & Environmental Science* (2012), Bd. 5(3): S. 5874
- [Pro94] E. K. Propst und P. A. Kohl: The Electrochemical Oxidation of Silicon and Formation of Porous Silicon in Acetonitrile. *J. Electrochem. Soc* (1994), Bd. 141: S. 1006–1013
- [Rai76] S. I. Raider; R. Flitsch; J. A. Aboaf und W. A. Pliskin: Surface Oxidation of Silicon Nitride Films. *Journal of The Electrochemical Society* (1976), Bd. 123(4): S. 560
- [Sah57] C.-t. Sah; R. Noyce und W. Shockley: Carrier Generation and Recombination in P-N Junctions and P-N Junction Characteristics. *Proceedings of the IRE* (1957), Bd. 45(9): S. 1228–1243
- [Sch95] M. Schöfthaler und R. Brendel: Sensitivity and transient response of microwave reflection measurements. *J. Appl. Phys* (1995), Bd. 77(7): S. 3162–3173
- [Sch96] F. Schuurmans; A. Schönecker; J. Eikelboom und W. Sinke: Crystal-orientation dependence of surface recombination velocity for silicon nitride passivated silicon wafers, in: *Conference Record of the Twenty Fifth IEEE Photovoltaic Specialists Conference - 1996*, IEEE, S. 485–488
- [Sch97] F. M. Schuurmans; A. Schönecker; A. R. Burgers und W. C. Sinke: Simplified evaluation method for light-biased effective lifetime measurements. *Applied Physics Letters* (1997), Bd. 71(13): S. 1795
- [Sch98] A. Schenk: Finite-temperature full random-phase approximation model of band gap narrowing for silicon device simulation. *Journal of Applied Physics* (1998), Bd. 84(7): S. 3684

- [SH12] H. Schulte-Huxel; R. Bock; S. Blankemeyer; A. Merkle und R. Brendel: Aluminum-Based Mechanical and Electrical Laser Interconnection Process for Module Integration of Silicon Solar Cells. *IEEE Journal of Photovoltaics* (2012), Bd. 2(1): S. 16–21
- [Sin85] K. S. W. Sing; D. H. Everett; R. A. Haul; L. Mosou; R. A. Pierotti; J. Rouquerol und T. Siemieniewska: Reporting physisorption data for gas/solid systems with special reference to the determination of surface area and porosity. *Pure Appl. Chem* (1985), Bd. 57(4): S. 603–619
- [Sin96] R. Sinton; A. Cuevas und M. F. Stuckings: Quasi-steady-state photoconductance, a new method for solar cell material and device characterization, in: *25th IEEE Photovoltaic Specialists Conference*, S. 457–460
- [Tan92] M. Tanaka; M. Taguchi; T. Matsuyama; T. Sawada; S. Tsuda; S. Nakano; H. Hanafusa und Y. Kuwano: Development of New a-Si/c-Si Heterojunction Solar Cells: ACJ-HIT (Artificially Constructed Junction-Heterojunction with Intrinsic Thin-Layer). *Japanese Journal of Applied Physics* (1992), Bd. 31(Part 1, No. 11): S. 3518–3522
- [Tay96] H. Tayanaka und T. Matsushita: Separation of thin epitaxial Si films on porous Si for solar cells, in: *Proc. 6th Sony Research Forum*, S. 556
- [The70] M. J. J. Theunissen; J. A. Appels und W. H. C. G. Verkuylen: Application of Preferential Electrochemical Etching of Silicon to Semiconductor Device Technology. *Journal of The Electrochemical Society* (1970), Bd. 117(7): S. 959–965
- [The72] M. J. J. Theunissen: Etch Channel Formation during Anodic Dissolution of N-Type Silicon in Aqueous Hydrofluoric Acid. *J. Electrochem. Soc.: Solid-State Science and Technology* (1972), Bd. 119(3): S. 351–360
- [Tie84] T. Tiedje; E. Yablonovitch; G. D. Cody und B. G. Brooks: Limiting efficiency of silicon solar cells. *IEEE Transactions on Electron Devices* (1984), Bd. 31(5): S. 711–716
- [Tru03] T. Trupke; M. A. Green; P. Würfel; P. P. Altermatt; A. Wang; J. Zhao und R. Corkish: Temperature dependence of the radiative recombination coefficient of intrinsic crystalline silicon. *Journal of Applied Physics* (2003), Bd. 94(8): S. 4930
- [Tru05] T. Trupke; R. A. Bardos; M. D. Abbott und J. E. Cotter: Sun-photoluminescence: Contactless determination of current-voltage characteristics of silicon wafers. *Applied Physics Letters* (2005), Bd. 87(9): S. 093503
- [Tur58] D. R. Turner: Electropolishing Silicon in Hydrofluoric Acid Solutions. *Journal of The Electrochemical Society* (1958), Bd. 105(7): S. 402–408
- [Uhl56] A. Uhlir: Electrolytic Shaping of Germanium and Silicon. *Bell System Technical Journal* (1956), Bd. 35(2): S. 333–347

- [Vei13] B. Veith; T. Ohrdes; F. Werner; R. Brendel; P. P. Altermatt; N.-P. Harder und J. Schmidt: Injection dependence of the effective lifetime of n-type Si passivated by Al₂O₃: An edge effect? *Solar Energy Materials and Solar Cells* (2013)
- [vH07] J. L. van Hemmen; S. B. S. Heil; J. H. Klootwijk; F. Roozeboom; C. J. Hodson; M. C. M. van de Sanden und W. M. M. Kessels: Plasma and Thermal ALD of Al₂O₃ in a Commercial 200 mm ALD Reactor. *J. Electrochem. Soc* (2007), Bd. 154(7): S. G165–G169
- [Wat71] Y. Watanabe und T. Sakai: Application of a thick anode film to semiconductor devices. *Reviews of the Electrical Communications Laboratories* (1971), Bd. 19(7-8): S. 899
- [Wer13] F. Werner; Y. Larionova; D. Zielke und J. Schmidt: Aluminum Oxide Based Inversion Layer Solar Cells on n-Type c-Si, in: *28th European Photovoltaic Solar Energy Conference*, Bd. 2CO.3.2
- [Wil96] K. R. Williams und R. S. Muller: Etch Rates for Micromachining Processing. *Journal of Microelectromechanical Systems* (1996), Bd. 5(4): S. 256–269
- [Wil03] K. R. Williams; K. Gupta und M. Wasilik: Etch Rates for Micromachining Processing - Part II. *Journal of Microelectromechanical Systems* (2003), Bd. 12(6): S. 761–778
- [Wol63] M. Wolf und H. Rauschenbach: Series resistance effects on solar cell measurements. *Advanced Energy Conversion* (1963), Bd. 3(2): S. 455–479
- [Yab82] E. Yablonovitch und G. Cody: Intensity enhancement in textured optical sheets for solar cells. *IEEE Transactions on Electron Devices* (1982), Bd. 29(2): S. 300–305
- [Zha11] D. Zhang; A. Tavakoliyaraki; Y. Wu; R. van Swaaij und M. Zeman: Influence of ITO deposition and post annealing on HIT solar cell structures. *Energy Procedia* (2011), Bd. 8: S. 207–213

List of symbols

Symbol	Description	Unit
α_{Si}	Absorption coefficient of Si	cm^{-1}
A	Absorption	
c_{HF}	HF-concentration	wt%
D_{p}	Holes diffusion coefficient	cm s^{-2}
η	Efficiency	%
E_{a}	Activation energy	eV
E_{QE}	External quantum efficiency	
FF	Fill factor	%
G	Generation rate	$\text{cm}^{-3} \text{s}^{-1}$
I_{QE}	Internal quantum efficiency	
J	Current density	mA cm^{-2}
J_{PS}	Critical current density	mA cm^{-2}
J_{SC}	Short-circuit current density	mA cm^{-2}
J_{SC}^*	Photogeneration current density	mA cm^{-2}
k	Boltzmann constant	$1.38065 \times 10^{-23} \text{ J K}^{-1}$
k_{Si}	Extinction coefficient of Si	
N_{D}	Dopant concentration	cm^{-3}
n_{i}	Intrinsic carrier concentration	cm^{-3}
n_{Si}	Refractive index of Si	
N_{Si}	Atomic density of Si	$5.02 \times 10^{22} \text{ cm}^{-3}$
n_{v}	Dissolution valence	
Φ	Photon flux	$\text{cm}^{-2} \text{ s}^{-1}$
p	Porosity	%
Δp	Excess carrier concentration	cm^{-3}
q	Elementary charge	$1.6022 \times 10^{-19} \text{ A s}$

Symbol	Description	Unit
r	Rate of pore growth	μm^{-1}
R	Reflection	
R	Recombination rate	$\text{cm}^{-3} \text{s}^{-1}$
R_{sheet}	Sheet resistance	Ω
$2r_0 = d_0$	Pore distance	μm
r_p	Pore radius	μm
S	Surface recombination velocity	cm s^{-1}
τ	Carrier lifetime	us
T	Temperature	K
T	Transmission	
V	Voltage	V
V_{OC}	Open-circuit voltage	V
W	Thickness	μm
W_{eff}	Effective thickness	μm

List of publications

Refereed journal papers

1. R. Brendel and M. Ernst, “Macroporous Si as an absorber for thin-film solar cells,” *Phys. Status Solidi RRL* **4** (1-2), pp. 40–42 (2010).
2. M. Ernst and R. Brendel, “Modeling effective carrier lifetimes of passivated macroporous silicon layers,” *Solar Energy Materials and Solar Cells* **95** (4), pp. 1197–1202 (2011).
3. M. Ernst, U. Zywietz, and R. Brendel, “Point contact openings in surface passivated macroporous silicon layers,” *Solar Energy Materials and Solar Cells* **105**, pp. 113–118 (2012).
4. M. Ernst, R. Brendel, R. Ferré, and N.-P. Harder, “Thin macroporous silicon heterojunction solar cells,” *Phys. Status Solidi RRL* **6** (5), pp. 187–189 (2012).
5. M. Ernst and R. Brendel, “Macroporous silicon solar cells with epitaxial emitter,” *IEEE Journal of Photovoltaics* **3** (2), pp. 723–729 (2013).
6. M. Ernst and R. Brendel, “Lambertian light trapping in thin monocrystalline macroporous Si layers,” submitted to *Phys. Status Solidi RRL* (2013).

International conferences

1. M. Ernst and R. Brendel, “Large area macroporous silicon layers for monocrystalline thin-film solar cells,” in *Proceedings of 35th IEEE Photovoltaic Specialists Conference*, 2010, pp. 3122–3124.
2. M. Ernst, R. Brendel, R. Ferré, N.-P. Harder, and S. Kajari-Schröder, “Macroporous silicon as an absorber for thin heterojunction solar cells,” in *Proceedings of 38th IEEE Photovoltaic Specialists Conference*, 2012, pp. 1040–1045.
3. M. Ernst, H. Schulte-Huxel, S. Kajari-Schröder, and R. Brendel, “Thin crystalline macroporous silicon solar cells with ion implanted emitter,” presented at SiliconPV 2013 in Hamelin and submitted to *Energy Procedia* 2013.

4. S. Schäfer, M. Ernst, S. Kajari-Schröder, and R. Brendel, "Multilayer etching for kerf-free solar cells from macroporous silicon," presented at SiliconPV 2013 in Hamelin and submitted to Energy Procedia 2013.
5. M. Ernst and R. Brendel, "Advanced structures for photovoltaics from macroporous silicon," presented at E-MRS 2013 Spring Meeting, Strasbourg.

International and national workshops

1. M. Ernst, "Macroporous silicon as a new absorber for thin-film solar cells," Silicon-FOREST Workshop 2011, Falkau, Germany, (2011).
2. M. Ernst, U. Zywietz, R. Brendel, "Local point contact openings in passivated macroporous silicon layers," 5th International Workshop on Crystalline Silicon Solar Cells - CSSC-5, Boston, USA, (2011).
3. M. Ernst, "Makroporöse Siliziumsolarzellen," Silicon-FOREST Workshop 2013, Falkau, Germany, (2013).

Popular scientific journals

1. P. P. Altermatt, M. Ernst, E. Garralaga, L. Kühnemund, C. Tegenkamp, R. Brendel, "Nanostrukturen für Solarzellen - Kleine Strukturen mit großer Wirkung," *Unimagazin, Leibniz Universität Hannover*, 01/02 2011, pp. 60–62.
2. M. Ernst, "Makroporöses Silizium für ultradünne monokristalline Solarzellen," *Ingenieur Spiegel*, Public Verlagsgesellschaft und Anzeigenagentur mbH, 04/2011, pp. 4–6.
3. P. P. Altermatt, M. Ernst, E. Garralaga, L. Kühnemund, C. Tegenkamp, R. Brendel, "Nanostrukturen für Solarzellen," *AlumniCampus, Leibniz Universität Hannover*, Ausgabe 6, Juni 2011, pp. 36–38.
4. M. Ernst, "Dünne Solarzellen aus makroporösem Silizium," *Ingenieur Spiegel*, Public Verlagsgesellschaft und Anzeigenagentur mbH, 04/2012, pp. 50–51.

Patent Applications

1. R. Brendel, M. Ernst, and H. Plagwitz, "Verfahren zum Bilden von dünnen Halbleiterschichtsubstraten sowie Verfahren zum Herstellen eines Halbleiterbaulements, insbesondere einer Solarzelle, mit einem solchen Halbleiterschichtsubstrat," German Patent application DE102009024613, Filing date: 12.06.2009

-
2. R. Brendel and M. Ernst, “Verfahren zum Bilden von dünnen Halbleiterschichtsubstraten sowie Verfahren zum Herstellen eines Halbleiterbauelements, insbesondere einer Solarzelle, mit einem solchen Halbleiterschichtsubstrat,” German Patent application DE102009053262, Filing date: 13.11.2009

Persönliche Daten

Name	Marco Ernst
Anschrift	Ostertorwall 20, 31785 Hameln
Geburtsdatum	11. April 1983
Nationalität	Deutsch

Schulbildung

1989 - 1993	Grundschule Schwaförden
1993 - 1995	Orientierungsstufe Schwaförden
1995 - 2002	Gymnasium Sulingen
	Abschluss der allgemeinen Hochschulreife im Juni 2002

Ersatzdienst

August 2002 - Mai 2003	Sozialstation Sulinger Land
-------------------------------	-----------------------------

Universitätsausbildung

Oktober 2003 - März 2006	Technische Universität Braunschweig Studium der Physik
Mai 2006 - November 2008	Gottfried Wilhelm Leibniz Universität Hannover Studium der Physik Diplomprüfung im November 2008
Oktober 2007 - Oktober 2008	Institut für Solarenergieforschung in Hameln/Emmerthal Diplomarbeit

Anstellung

Seit Januar 2009	Institut für Solarenergieforschung in Hameln/Emmerthal Wissenschaftlicher Mitarbeiter im Bereich Silicium-Dünnschichtzellen
-------------------------	---